University of Ljubljana
Faculty of Mathematics and Physics

Andrej Studen

Compton Camera with Position-Sensitive Silicon Detectors

Doctoral Thesis

Supervisor: Prof. Dr. Marko Mikuž

Ljubljana, 2005

Univerza v Ljubljani
Fakulteta za matematiko in fiziko

Andrej Studen

Comptonska kamera s krajevno ločljivimi silicijevimi detektorji

Doktorska disertacija

Mentor: prof. dr. Marko Mikuž

Ljubljana, 2005

Ta doktorat ne bi nastal brez izdatne pomoči ljudi okrog mene. Na prvem mestu je mentor in šef Marko Mikuž, ki je znal kritično presoditi moje ideje in me uspešno voditi do uspešnega zaključka. Posebna zahvala gre Dejanu Žontarju za motivacijo pisanju, skrbno branje in opozorila na neskladja in slogovne napake v doktorskem delu. Pri projektu Comptonska kamera sta pomembno sodelovala še Vladimir Cindro in Erik Margan. Za prijetno delovno vzdušje bi se rad zahvalil tudi vsem ostalim sodelavcem z Odseka za eksperimentalno fiziko osnovnih delcev Instituta Jožef Stefan.

I should also like to thank people from all over the world who participated in this Compton camera study. First there are the project master minds Neal Clinthorne and Les Rogers from University of Michigan. During my stays in Michigan there were Lisha, Sang-June and Sam who helped to push things along. When working in CERN I had strong support from local Compton camera group, including the leader of the European part Peter "Failure is Impossible" Weilhammer, electronic wizard Enrico Chesi, people at bonding lab, Nail Malakhov with regular soup and tea breaks, and Dirk Meier, currently at IDEAS, who introduced me to the problematic and invited me to many jogs below the Jura. In Valencia, special thanks goes to Gabriela Llosa Llacer for sharing restless Sundays figuring Why Things Don't Work Like They Are Supposed To and Carlos Lacasta for writing DAQ software. I will not forget Harris Kagan from Ohio State University, who was an inexhaustible source of ideas.

Nazadnje bi se zahvalil še prijateljem in družini, še posebej Kati za moralno podporo in Anji, da me je naučila, da energija ni vedno sorazmerna masi.

Abstract

Currently, SPECT uses a mechanically collimated (Anger) camera to detect distribution of γ sources. The detection technique, however, suffers from resolution-efficiency trade-off inherent to mechanical collimation. Compton camera principle is a suggested alternative which avoids the trade-off. In Compton camera, Compton scattering of emitted photons is detected in a special scattering detector which replaces the mechanical collimator. The direction of the incoming photon is determined from kinematics of Compton scattering.

The thesis describes the development and evaluation of a Compton camera prototype. The prototype consisted of two sub-detectors: the scattering detector or the scatterer and an absorber which detects the scattered photons. The scatterer consisted of multiple scatterer modules amplifying the prototype's efficiency. Each module was equipped with a custom-designed position-sensitive silicon pad sensor coupled to an off-shelf associated electronics. Modules were calibrated and tested. The measurements confirmed energy and spatial resolution of the modules suitable for Compton camera.

The imaging heads of the existing SPRINT II imaging ring were the absorber modules of the prototype, matching the requirements of Compton camera. The modules were calibrated and tested, and measured results confirmed their eligibility.

The prototype was assembled on a custom designed frame. The scatterer was set in the center and three absorber modules formed a semi-ring around the scatterer. The layout of the prototype was optimized for imaged objects placed on axis on the semi-ring, providing best imaging performance with detection of events with the scattering angles around $\pi/2$. Data for photons emitted from an on-axis ^{99m}Tc point source were measured and from those, the position of the source was reconstructed using a simple back-projection technique.

The determined performance of this simple prototype is similar to the performance of a typical Anger camera. A more refined and improved applications of the principle should excel the performance of present cameras and hence be a competitive tool for future SPECT imaging. A suggested application is a prostate probe, which would enable SPECT imaging of the prostate, an unreachable task for present detection techniques.

Keywords: *SPECT, Compton camera, silicon pad detectors, scintillation camera*

PACS:

29.30.Kv X- and gamma-ray spectroscopy,
29.40.Gx Tracking and position-sensitive detectors,
87.58.Ce Single photon emission computed tomography (SPECT).

Izvleček

Dandanašnji slikanje izvorov žarkov γ pri SPECT opravi kamera s svinčenimi zaslonkami (Angerjeva kamera). Z metodo je neločljivo povezana izmenjava med izkoristkom in ločljivostjo. Težavo premosti Comptonska kamera; namesto zaslonk ima kamera poseben sipalni detektor, v katerem se izsevani fotoni comptonsko sipajo. Smer vpadenga fotona nato doloįmo na podlagi kinematike sipanja.

Dokotorska disertacija opisuje razvoj in preizkus delovanja prototipa Comptonske kamere. Prototip je bil sestavljen iz dveh pod-detektorjev: sipalnega detektorja oz. sipalca in absorberja, ki zaznava sipane fotone. Sipalec sestavljajo moduli sipalca; večje število modulov znantno poveča izkoristek prototipa. Za modul smo razvili posebne krajevno-ločljive silicijeve detektorje z blazinicami in jih sklopili s primerno bralno elektroniko. Umerjeni moduli so pokazali časovno in energijsko ločljivost primerno uporabi v Comptonski kameri.

Detektorske glave obroča SPRINT II, namenjenega slikanju sevalcev γ, smo uporabili kot module za absorber, saj njihove lastnosti ustrezajo potrebam Comptonske kamere. Module smo umerili, rezultati preizkusov pa so potrdili njihovo primernost.

Za prototip je bilo izdelano primerno ogrodje: v centru je bil sipalec, obkrožen s tremi moduli absorberja, ki so tvorili nepopoln obroč. Slikanje je bilo optimizirano za izvore postavljene v os obroča absorberjev, kar je omogočalo zaznavanje dogodkov s sipalnimi koti okrog $\pi/2$, ki dajejo najnatančnejšo sliko izvorov. Prototip smo preizkusli za točkast izvor ^{99m}Tc postavljen v os obroča in lego izvora rekonstruirali s preprosto projekcijo izmerkov nazaj v prostor izvorov.

Meritve so pokazale, da so lastnosti preprostega prototipa primerljive z lastnostmi sofisticiranih Angerjevih kamer. Prototip omogoča številne izboljšave, kar nakazuje obetavnost bodočih aplikacij Comptonske kamere. Ena izmed idej je proba za prostato, ki bi omogočala slikanje prostate s SPECT, česar trenutna SPECT tehnologija še ne zmore.

Ključne besede: *SPECT, Comptonska kamera, silicijevi detektorji z blazinicami, scintilacijska kamera.*

PACS: 29.30.Kv, 29.40.Gx, 87.58.Ce.

Contents

Chapter 1

INTRODUCTION

In the field of medical imaging, single photon emission computed tomography (SPECT) is one of the methods enabling in-vivo functional imaging of the tissue. This makes it an important tool in disease recognition and treatment monitoring. In SPECT the patient is injected with a radio-tracer that is a disease-specific bio-molecule with chemically bonded radio-active nucleus. A camera sensitive in the energy range of the emitted gamma-rays detects the spatial distribution of the tracer molecule concentration over time.

Conventional SPECT imagers (Anger cameras) use mechanical collimators to detect the spatial distribution of the radio-tracers. Mechanical collimation couples the spatial resolution and efficiency of the device in an inverse fashion thus limiting the achievable resolution with acceptable patient-absorbed doses of radiation. To overcome this resolution-efficiency trade-off, "electronic" collimation, based on Compton scattering kinematics was proposed [TNE74].

In case of electronic collimation the mechanical collimator is replaced with a scatterer, a sensor where photons are Compton scattered. A second sensor (the absorber) photo-absorbs the Compton scattered photons and both sensors operate in coincidence. The kinematics of Compton scattering is used to determine the scattering angle based on the measured kinetic energy of the Compton electron. All possible directions of incoming photon form a cone, centered on the first interaction point. This leads to an additional ambiguity as opposed to mechanical collimation where a line can be traced from the detector to the source. The much higher efficiency of electronic collimation however overcomes this penalty.

The performance of a Compton camera is governed by the following parameters:

- Energy resolution. Either the energy of the recoil electron or the energy of the scattered photon have to be known. The detector-material choice should reflect that.

- Spatial resolution. Both detectors should at least match the resolution of a comparable Anger camera.

- Efficiency. The underlying conical ambiguity of Compton imaging requires the Compton camera to have a higher efficiency than its mechanically collimated counterpart for comparable image quality, which is further discussed in Chapter 7, Section 7.1.3.

- Timing of each sensor. Compton scattering events have to be properly matched to the interaction of the scattered photon in the absorber. Large discrepancies between timing of the individual sensors can lead to event mis-matching and small discrepancies increase the amount of random background.

- Image reconstruction. Since data collected on both sensors are only algebraically related to the true tracer density distribution, complex reconstruction techniques are required. The complexity of this stage can cause the final image to reflect both the quality of the technique and the quality of the collected data.

- Doppler broadening. Random motion of the bound electron prior to scattering is an inherent limit to the spatial resolution of the reconstructed image. The effect drops with increasing energy of the initial photons thus electronic collimation favors a choice of sources with higher energy of initial photons. This is in strong contrast to the Anger camera where photons with higher energy penetrate the collimator and increase background.

1.1 Historical overview

It was in the 1950-s that Hal Anger constructed his gamma camera [Ang58]. It was based on the recently discovered NaI(Tl) scintillator, and the collimation was performed using lead mechanical collimators. The simplicity of use, relative low cost and simple one-to-one imaging made it the imager of choice for SPECT. Nevertheless, imaging with Anger camera has been far from perfect. On average, only one per 10000 photons hitting the detector area contributes to the image, others are scattered in the collimator. There is the persistent trade-off between image resolution and efficiency of the imager. As lead septa get penetrated, imaging degrades with growing photon energy which limits the choice of imaging agents. All Compton scattered photons in the active detection area cause position ambiguity and have to be filtered away. Therefore a new detection principles are sought.

The principle of Compton imaging was introduced in the field of gamma-astronomy in 1973 [SHS73]. The photon energies are higher than in medical imaging, usually exceeding 1 MeV. Since mechanical collimation becomes impractical at high energies, Compton imaging becomes the method of choice. The Compton Gamma-Ray Observatory (CGRO) was a satelite observatory, orbiting earth between April 5, 1991 and June 4, 2000, and hosted COMPTEL telescope [GFF$^+$93] which detected location of celestial photon sources using Compton imaging principle. Several new projects involving Compton telescopes are being investigated [KAS$^+$04, BOA$^+$04].

Compton imaging in nuclear medicine followed, with the introduction in Nature by Todd and Nigthingale in 1974 [TNE74]. It took a while to implement the idea, and the first prototype was constructed by Singh et al. [Sin83]. Semiconductor scatterer of high purity germanium (HPGe) was used to measure the recoil electron energy, exhibiting the required energy resolution. The absorber was a conventional Anger camera, with its collimator removed . The prototype was used for qualitative studies of the method. Since the absorber was placed collinearly with the source and the scatterer, many direct hits were observed, causing pile-up in the absorber.

A ring setup of the absorber was introduced by 1993 to avoid direct hits in the absorber by Martin[MKW$^+$93] and co-workers. With the same type of scatterer (HPGe) as for the previous prototypes (Singh) they performed first imaging tests. The phantoms were simple - a source with or without uniform background. Their spatial resolution was within the order of magnitude of the available Anger cameras at comparable total efficiency. But taking into account the conical ambiguity their imaging performance was much worse than that of an Anger camera.

A further increase in spatial resolution was achieved with replacement of the HPGe scatterer with a silicon pad sensor[LCH$^+$99]. There are several facts favoring silicon: operation at room temperature with negligible loss of energy resolution, excellent spatial resolution, availability, high Compton to photo-absorption ratio, lower Doppler broadening, etc. Similar phantoms as with the first ring prototype were studied, and reconstructed images showed a factor of 2 improvement over the HPGe setup. However the performance of the silicon scatterer was still far from the desired. A thin silicon layer was used which significantly decreased the efficiency, energy resolution was much lower than expected and timing was not optimized, thus their prototype was still far away from matching Anger camera performance.

1.2 Objectives of thesis

Encouraged by recent development of silicon sensor technology, the thesis concentrates on a development of a Compton camera with position sensitive silicon sensors for medical imaging. As pointed out in [Bla99] there are a number of theoretical advantages of using a Compton camera over an Anger camera:

- Higher system sensitivity at required spatial resolution, either improving image at a given radiation dose uptake by the patient, or decreasing the dose at a given image quality.
- Better performance at higher gamma-ray energies. Anger camera performance decreases rapidly with increasing gamma-ray energy due to collimator penetration. High energy photons are less likely to scatter in the patient, providing a better data sample. Development of higher energy imaging agents has been hindered by the choice of the imager, and for those Compton imaging could offer a suitable detection technique.

Maintaining the ring geometry [MKW+93, LCH+99], efforts were concentrated on further development of the silicon sensor array to be used as the scatterer. Silicon pad sensors [WND+96] are an attractive choice for a scatterer of a Compton camera used in medical imaging, since they offer:

- lower Doppler broadening compared to germanium or other high atomic number semiconductors (CZT,CdTe),
- excellent spatial resolution,
- adequate energy resolution even at room-temperature,
- high Compton scattering to photo-absorption ratio,
- mature processing techniques,
- robustness.

The goal of the thesis is to construct a Compton camera prototype with a custom developed scatterer module based on silicon pad sensors and associated read-out electronics. The absorber is composed of a set of existing modules taken from a single photon ring imager (SPRINT II, [RCS+88]). The prototype is to be tested and its performance evaluated.

Chapter 2

Basic principles of Compton Camera operation

2.1 Compton camera principle

The underlying principle of the Compton camera is a kinematic reconstruction of Compton scattering. Compton scattering was first described by H.G. Compton in 1923 [Com23] and the mechanism of the interaction is illustrated in figure 2.1: A photon scatters off a bound electron, thereby transferring part of its energy and momentum. In Compton scattering, the energy transfer exceeds by far the electron's binding energy, causing the electron to be released from the atom. The direction of the photon is changed and its energy reduced for the amount transferred to the electron. Only the photon and the electron are involved in the interaction and the process can be described as a simple two-body problem, yielding a relation of the photon's scattering angle to the energy transfer.

To reconstruct a Compton scattering event, the Compton camera is made of two sensors. In the first sensor, the scatterer, Compton scattering takes place and in the second, the absorber, the scattered photon is absorbed. In the scatterer, three quantities are measured: the time of the interaction, the point of interaction and the kinetic energy of the released electron. For a successful reconstruction the scattered photon has to escape from the scatterer and be absorbed in the absorber. The three quantities measured by the absorber are the time of interaction, the impact point and the energy of the scattered photon.

The three measurements from each of the sensors are combined to reconstruct the initial photon direction. Timing information from both sensors is required for coincidence measurement, the two interaction positions determine the scattered photon direction and the kinetic energy of the electron is used to determine the scattering angle. Energy of the scattered photon can be measured with a low energy resolution and is only used for an off-line background rejection. Namely in the case of proper matching, the sum of the kinetic energy

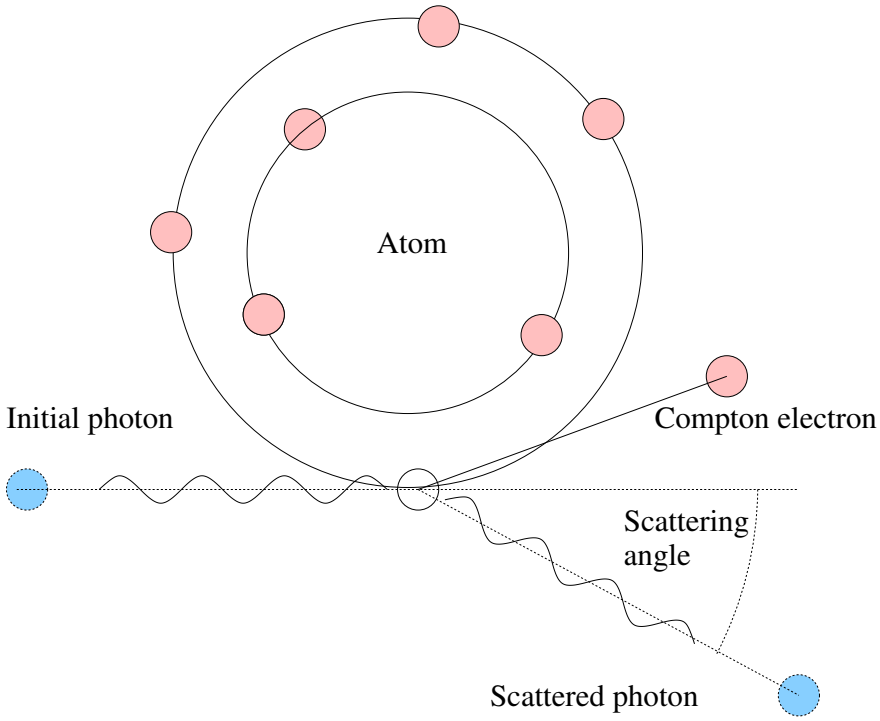

Figure 2.1: Schematic representation of a Compton scattering.

of the electron and the energy of the scattered photon is equal to the energy of the initial photon.

With the scattering angle determined, all possible directions of the incoming photon form a surface of a cone: the axis of the cone is given by the scattered photon direction, the opening angle equals the scattering angle and the apex is fixed to the interaction point in the scatterer. Figure 2.2 illustrates the conical ambiguity of each of the reconstructed events and how intersection of several events yields the position of the photon source[1].

Normally energy resolution of the absorber is much lower than resolution of the scatterer and energy measured in the absorber is only used for rejection of background events. Namely in the case of proper matching, the sum of the kinetic energy of the electron and the energy of the scattered photon is equal to the energy of the initial photon. However if energy resolution of the absorber is comparable to energy resolution of the scatterer, a factor $\sqrt{2}$ gain in energy resolution is obtained if energies measured in both sub-detectors are considered.[2]

The equation relating the scattering angle to the energy transfer is determined from the energy-momentum conservation laws. The expression, relevant for the Compton camera

[1]This procedure is sometimes referred to as *electronic collimation* since collimation is done with a sensor and associated electronics rather than with a mechanical collimator.

[2]N. H. Clinthorne. US patent #6,323,492; 2001.

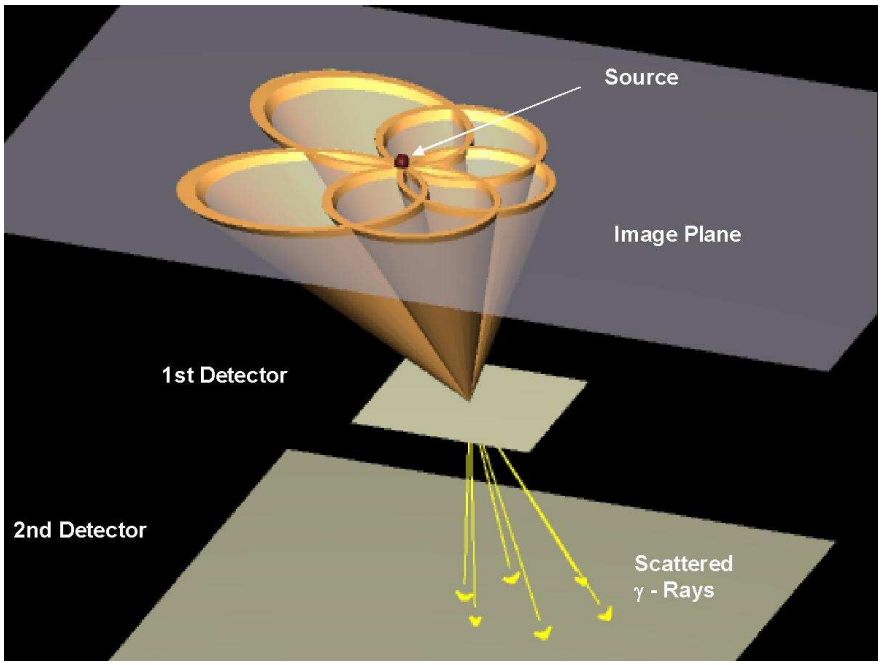

Figure 2.2: Schematic drawing of a source reconstruction with a Compton camera. Each event corresponds to a cone of possible initial photon directions. Intersections of several cones yield the position of the photon source.

relates the scattering angle θ to the kinetic energy of the electron E_e:

$$\sin^2 \frac{\theta}{2} = \frac{m_e c^2 E_e}{2E_\gamma(E_\gamma - E_e)}, \tag{2.1}$$

where the electron is assumed to be at rest before the interaction. The energy of the initial photon, E_γ, is determined by the properties of the radio-tracer used. The two constants are m_e, rest mass of the electron and c, the velocity of light in vacuum. By setting $\sin\theta/2$ to one, one can determine $E_e^{\max}$, the maximum of E_e:

$$E_e^{\max} = \frac{1}{1 + \frac{m_e c^2}{2E_\gamma}} E_\gamma. \tag{2.2}$$

This value is commonly referred to as the Compton edge.

2.2 Performance parameters of Compton camera

Compton camera performance is evaluated in terms of its efficiency and the spatial resolution of the reconstructed spatial distribution of radio-tracers. At a given image quality the

efficiency of a Compton camera is expected to exceed that of an Anger camera by several orders of magnitude. With higher efficiency the procedure can be optimized either for lower radiation doses absorbed by the patient or shorter imaging times, giving a sequence of images depicting the physiology of the selected tissue. The spatial resolution of the reconstructed source distribution determines the smallest features still visible on the image. SPECT can be also used for searches of cancer lesions, and the smaller the discovered abnormalities, the better the chance for a successful treatment.

The efficiency of the Compton camera is the portion of photons emitted by the radio-tracer which is used in the reconstruction of the radio-tracer spatial distribution. For an event to be reconstructed, the following sequence of events has to occur:

- a photon is emitted in the solid angle covered by the scatterer
- the photon undergoes Compton scattering in the scatterer
- the scattered photon escapes from the scatterer, its direction within the solid angle spanned by the absorber
- the scattered photon is detected in the absorber

The efficiency depends substantially on the radio-nuclide bonded in the radio-tracer, so a short summary of the radio-nuclides used in contemporary SPECT imagers will follow later in this Chapter. On top of that, the efficiency depends on the detector geometry, and an evaluation for a specific prototype will be given with the prototype description in Chapter 5. Because of the underlying conical ambiguity the efficiency of a Compton camera should not be directly compared to the efficiency of an Anger camera and a more detailed analysis of a comparison procedure will be given in Chapter 7

The limited resolution of the Compton collimation is exhibited as broadening of the cone formed by possible directions of incoming photon. The measure of the broadening is an angular probability distribution function (pdf) with the scattering angle as an argument, which is a cross-section of probability through the thickened cone[3]. In the following discussion, the angular resolution is determined as the full-width-at-half-maximum (FWHM) of this angular pdf. Spatial resolution (in terms of FWHM of the spatial distribution) is proportional to the determined separation $d_{\mathrm{src-scat}}$ between the source and the scatterer and evaluated angular resolution.

There are three contributions to the angular resolution: the inherent resolution given by Doppler broadening, the contribution of limited energy resolution of the scatterer and geometric contribution related to determination of the scattered photon track. The former two contributions depend significantly on the selected radio-nuclide so they will be discussed following the introduction of the radio-tracers suitable for SPECT imaging with Compton

[3]In an ideal case of perfect resolution, the pdf is a $\delta()$ function.

camera, given in the next section. The geometric contribution however depends substantially on the detector layout and will be evaluated for actual prototype in Chapter 5.

2.3 Radio-tracers for SPECT imaging with a Compton camera

The Compton camera principle significantly differs from the principle of the Anger camera, so the two approaches may favor different photon energies, and consequentially, different radio-tracers. The radio-active isotope bonded in the radio-tracer is called a radionuclide. Table 2.1 gives a list of radionuclides , candidates for a Compton camera SPECT.

Radio-tracer is a chemical compound of a radionuclide with a disease-specific bio-molecule. About 90% of all radio-tracers are based on ^{99m}Tc. The most important reasons for that are the low energy of the emitted photons, which is well-suited to mechanical collimators of the Anger cameras, the monochromatic spectrum with virtually no β-radiation, and suitable life-time. The draw-back of using ^{99m}Tc is the high probability of additional scatter in the patient, which deteriorates the image and increases the patient-absorbed radio-active dose. The angular resolution of Compton camera, both the scatterer energy resolution and the Doppler broadening contribution, favor higher photon energies, so tracers based on ^{99m}Tc are not the optimal choice for Compton camera imaging.

Table 2.1: List of radio-active sources (radionuclides) which could be used in radio-tracers imaged by a Compton camera.

nuclide	principal γ-ray energies [keV]	half-life	comments
^{99m}Tc	140.5	6.01 hours	
^{123}I	159.0	13.27 hours	also 1 MeV β-s
^{111m}In	245.5, 171.3	2.8 days	
^{131}I	364.5	8.02 days	also 606 keV β-s
^{113m1}In	391.7	1.6 hours	
^{11}C, ^{13}N, ^{15}O, ^{18}F	511	20.4, 9.9, 2, 1 min	positron

Compton camera performs better for radionuclides with higher photon energies, such as ^{111m}In, ^{131}I, ^{113m1}In or positron sources ^{11}C, ^{13}N, ^{15}O, ^{18}F. ^{111m}In is popular because of its relatively long half life of 2.8 days, but with its principal γ-ray energies of 171 and 245 keV, imaging with Anger-camera type SPECT imagers only allows for low image resolution. In positron sources two back-to-back photons with energy of 511 keV are created following the annihilation of the positron. The collimation based on detection of the photon pair is called positron emission tomography (PET) and Compton camera principle can be used to enhance the spatial resolution of the reconstructed image [S. 01]. SPECT imaging of a single photon

of the pair is also interesting since it doesn't require the second photon to be detected. The positron sources are isotopes of elements frequent in human tissue and there are virtually no limitations on the bio-molecule selection, and the high energy of the photons decreases the probability of photon scatter in the tissue. Due to the collimator penetrability, an Anger camera is not practical at such photon energies and a Compton camera may well prove its advantage.

2.4 Effect of scatterer energy resolution on angular resolution

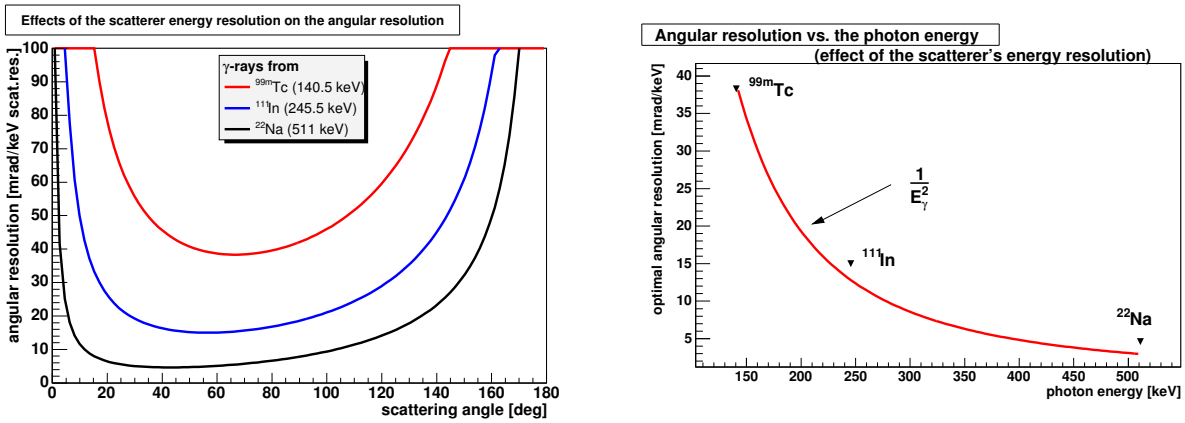

Figure 2.3: Left: Angular resolution due to finite energy resolution of the scatterer. The vertical axis is given in miliradians per keV scatterer resolution. The resolution lines for three possible radio-tracers are shown. Right: The optimal angular resolution taken from curves on the left versus the energy of the initial photon. The $1/E_\gamma^2$ fit is added. The vertical axis bears the same units as in the left part of the figure.

This section describes the influence of the scatterer energy resolution on the error of the source position estimation. The actual energy resolution of our scatterer will be described in Chapter 3, but the effects on the angular resolution are quite general. From (2.1) the scattering angle depends on E_e, the measured electron energy. The error of the scattering angle σ_θ is related to the energy resolution in the scatterer σ_E via:

$$\sigma_\theta^E = \frac{\sigma_{E_e}}{\sin\theta}\frac{m_e c^2}{E_\gamma^2}\Big(1+\frac{E_\gamma}{m_e c^2}(1-\cos\theta)\Big)^2. \tag{2.3}$$

The left side of Figure 2.3 shows angular resolution of Compton camera as function of scattering angle for three gamma-ray energies, clearly illustrating the $1/\sin\theta$ dependence. This implies low resolution of a device both at small and large scattering angles, and best resolution around scattering angle of 90° . The resolution improves with growing initial photon

energy. The right side of Figure 2.3 illustrates this improvement, showing the best resolution obtainable for a given initial photon energy. The improvement scales approximately with $1/E_\gamma^2$, as depicted on the image.

2.5 Doppler broadening

Doppler broadening represents an inherent limit on the Compton camera angular resolution. In this thesis we will present the mechanism of the broadening and its effect on the event reconstruction. Equation (2.1) assumes the bound electron to be at rest before the interaction, while in fact it is moving randomly within the atom or the crystal. Due to symmetry of Compton scattering the only important quantity is p_z, the component of $\vec{\mathbf{p}}$, the electron momentum, parallel to $\vec{\mathbf{q}}$, the scattering momentum, which is defined as the difference between $\vec{\mathbf{k}'}$, the scattered photon momentum and $\vec{\mathbf{k}}$, the initial photon momentum:

$$\vec{\mathbf{q}} = \vec{\mathbf{k}'} - \vec{\mathbf{k}}. \tag{2.4}$$

Recalculating the Compton relation (2.1) yields the following equations:

$$\sin^2\frac{\theta}{2} = \frac{mc^2 E_e}{2E_\gamma(E_\gamma - E_e)} - \Delta_{\vec{\mathbf{p}}}, \tag{2.5}$$

$$\Delta_{\vec{\mathbf{p}}} = \frac{p_z c\; qc}{2E_\gamma(E_\gamma - E_e)}, \tag{2.6}$$

$$qc = \sqrt{E_\gamma^2 - 2(E_\gamma - E_e)\cos\theta + (E_\gamma - E_e)^2} \tag{2.7}$$

The term $\Delta_{\vec{\mathbf{p}}}$ is the correction to (2.1) and qc is the magnitude of the scattering momentum.

The above relations imply that a given pair (E_e, θ) determines a value p_z:

$$p_z(E_e, \theta) = \frac{1}{qc}\left(E_e mc^2 - (E_\gamma - E_e)E_\gamma(1 - \cos\theta)\right) \tag{2.8}$$

The probability that for a given energy transfer E_e the scattering angle equals θ is given with $J(p_z)$, the probability that $p_z(E_e, \theta)$ will be encountered in the interaction. Values $J(p_z)$ are also called Compton profiles and they presented a great interest to atomic physicists since they offer a glimpse into the movement of the electron in an atom. Each atomic shell exhibits a different Compton profile and for an accurate evaluation of the effect, correct weighting has to be applied based on the probability that an electron from a certain shell is encountered. The tabulated values of $J(p_z)$ in [WP72] already account for that.

Our aim is to determine the scattering cross-section $\frac{d^2\sigma}{dE_e d\theta}$, which is proportional to the probability that the photon will transfer E_e while scattering for θ. Since the encountered

momentum component is independent from the energy transfer, we can write:

$$\frac{d^2\sigma}{dE_e dp_z} = \frac{d\sigma}{dE_e} J(p_z). \tag{2.9}$$

where $\frac{d\sigma}{dE_e}$ is the conventional, unbroadened Klein-Nishina differential cross-section. Changing the variables to E_e and θ gives $d^2\sigma/dE_e d\theta = d^2\sigma/dE_e dp_z \; |dp_z/d\theta|$. Inserting the derivative of (2.8) gives the double differential Klein-Nishina cross-section (DDKNXS):

$$\frac{d^2\sigma}{dE_e d\theta} = \pi r_0^2 \frac{mc^2(E_\gamma - E_e)}{E_\gamma (qc)^2} \left(1 + \cos^2\theta + \frac{E_e^2}{E_\gamma(E_\gamma - E_e)}\right)\left(p_z c + qc\right) J(p_z) \tag{2.10}$$

This analytical expression offers the possibility to compare Doppler broadening for various photon energies, detector materials, solid angle ranges, etc. The following examples concentrate on the effects interesting for a Compton camera.

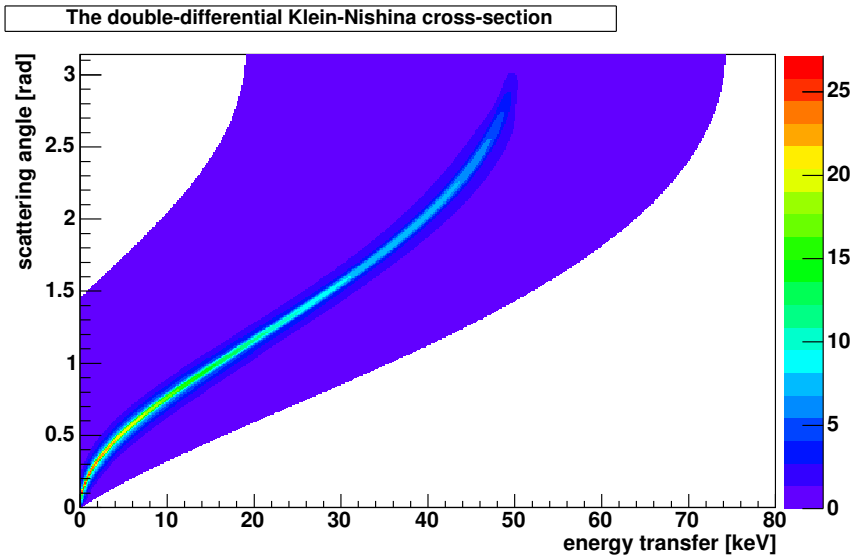

Figure 2.4: Double differential Klein-Nishina cross-section in silicon, given by (2.10). The cross-section is color-coded, with bright trace corresponding to the most probable events. Color scale is in units of $r_0^2/rad/keV$. For ^{99m}Tc, E_γ=140.5 keV.

Figure 2.4 shows the DDKNXS for ^{99m}Tc in silicon. The bright trace shows the Compton relation (2.1) which determines the principal scattering angles for a given energy transfer. The profiles of the DDKNXS show the distribution of the scattering angles around the central angle for a given energy transfer. This is a situation which resembles the actual measurement where the energy transfer is measured and scattering angle determined. If no electron movement were present, a single scattering angle would be possible,and angular pdf would be $\delta()$ function. The broadening of this distribution is called the Doppler broadening,

and the spread contributes to the error of the determined scattering angle. s

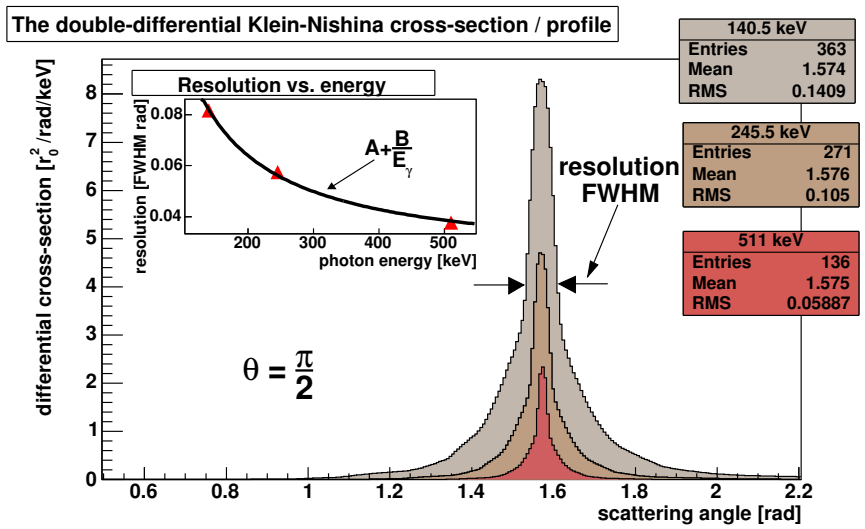

Figure 2.5: Profile of double differential Klein-Nishina cross-section for fixed energy transfer in scattering in silicon. Selected energy transfer corresponds to scattering angle of $\pi/2$. Error on scattering angle is given in terms of FWHM of distribution. Comparison for E_γ= 140.5, 245.5 and 511 keV is given. Inset shows resolution improving approximately as $1/E_\gamma$.

Figure 2.5 shows profiles of DDKNXS for the central scattering angle of $\pi/2$ for three different energies E_γ of the initial photon. The inset shows angular resolution obtained from the profiles to decrease approximately as $1/E_\gamma$, but with an asymptotic limit for large E_γ.

Figure 2.6 shows the dependence of the angular resolution in silicon on the central scattering angle determined from (2.1). Two facts are observed: first that the imaging is best at low scattering angles and that the resolution improves with the initial photon energy.

Doppler broadening also affects the spectrum of the excited electrons. Figure 2.7 shows the comparison of the model with no Doppler broadening and a more realistic one with broadening. The sharp edges of the former are smoothed out. The Compton edge ceases to be the maximum energy of the excited electrons since a part of the electron momentum is contributed by the electron movement.

The discussion on Doppler broadening will be concluded with a comparison of scattering materials. Doppler broadening is sensitive to the binding energy of the shells electrons are moving in. There is no simple Z, the atomic number, dependence. In high-Z atoms, the inner electrons are strongly bound to the core and high momenta can be encountered, but they only represent a small portion of the electrons available for Compton scattering. The comparison of different materials can be done on a one-to-one basis. Figure 2.8 shows a comparison of two most popular semiconductor materials, silicon and germanium. Germanium (32)

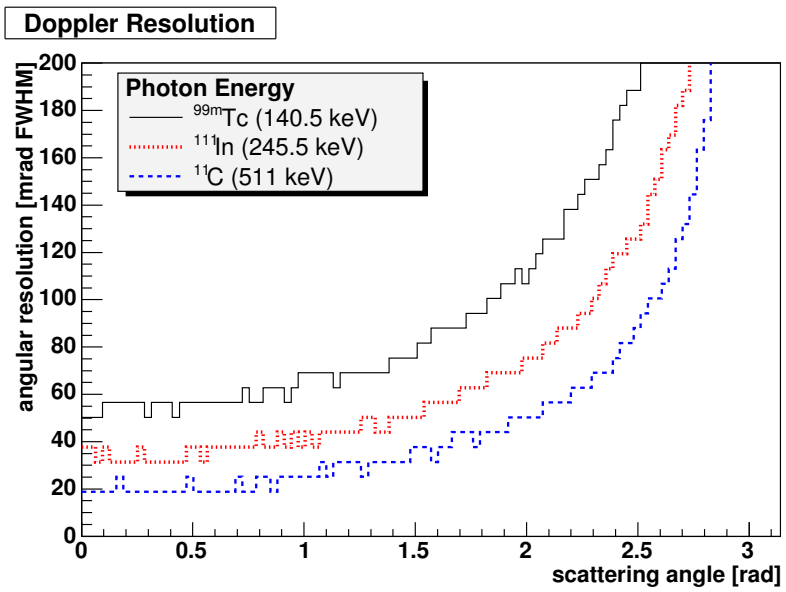

Figure 2.6: Error on scattering angles in silicon for fixed energy transfer. Horizontal axis shows the central scattering angle for given energy transfer. The resolution represents FWHM of the projection of DDKNXS. Comparison for E_γ=140.5, 245.5 and 511 keV.

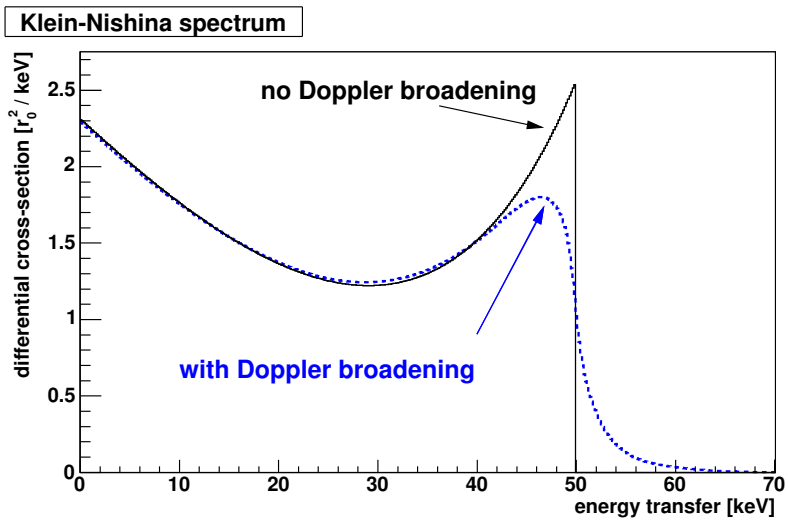

Figure 2.7: The spectrum of scattered electron kinetic energy. Comparison of Klein-Nishina cross-section with and without Doppler broadening For ^{99m}Tc on silicon, E_γ=140.5 keV.

contains more than twice as many electrons as silicon (14), which explains the larger total cross-section. Comparing the resolutions silicon performs much better, yielding half the

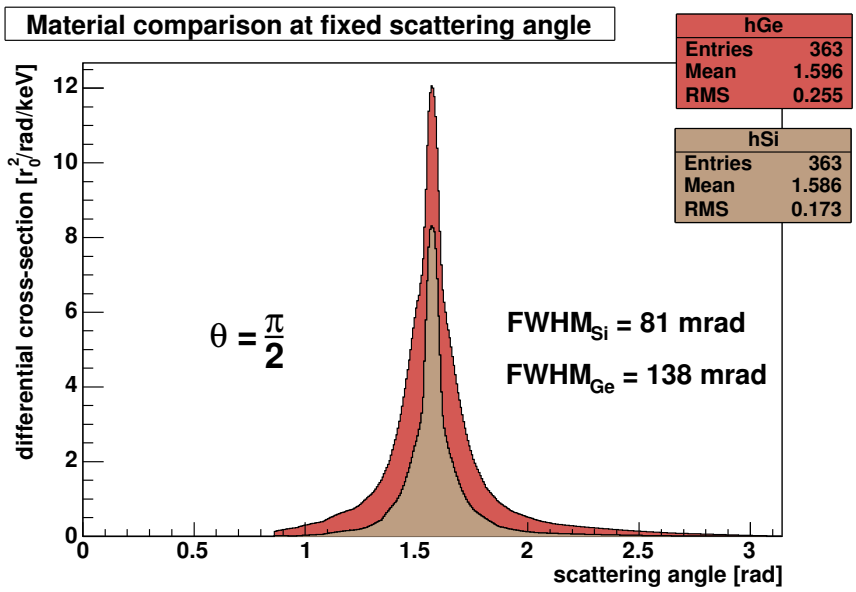

Figure 2.8: Profiles of DDKNXS for fixed scattering energy; comparison of silicon and germanium as scattering materials. Energy transfer corresponds to central scattering angle of $\pi/2$, E_γ=140.5 keV.

width of germanium at the scattering angle of $\pi/2$. Observing Figure 2.6 we see that the resolution is almost constant in a wide range of the scattering angles below this value, so the estimate of Figure 2.8 is a good measure of the corresponding resolutions.

2.6 Compton scattering probability

This section is devoted to the illustration of the dependence of the Compton interaction probability on the scattering angle, the energy transfer, the initial photon energy and the scattering material. This dependencies are derived by a quantum treatment of the Compton scattering, which was first presented by Klein and Nishina [KN28]. The probability of an interaction can be evaluated in different terms. Here it is given as a cross-section σ, in units of area. The attenuation coefficient μ which is the probability per unit depth traversed by the photon beam, is expressed as:

$$\mu = \frac{\rho N_A}{A}\ \sigma, \tag{2.11}$$

with ρ the material density, N_A the Avogadro number and A the atomic mass of the selected material. The attenuation length is the inverse of μ. The cross-sections are calculated for silicon, unless mentioned otherwise.

Figure 2.9 shows the Compton scattering differential cross-section with respect to the solid

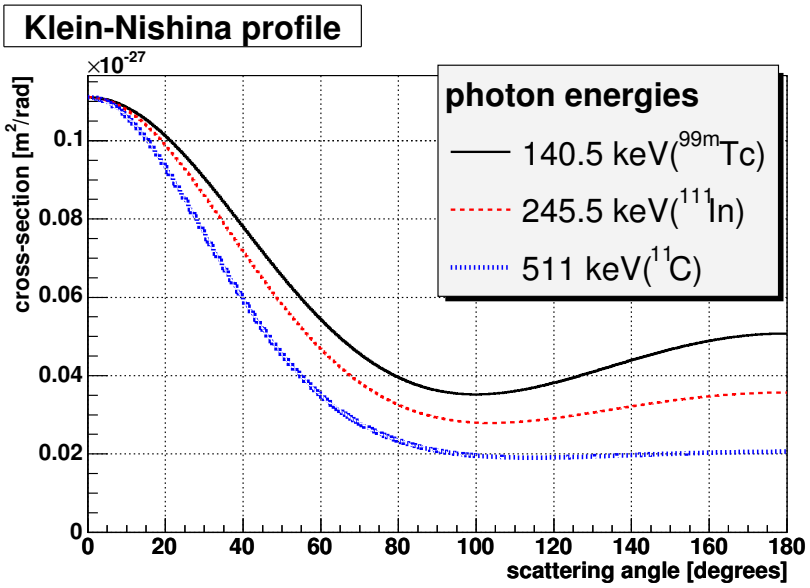

Figure 2.9: Compton scattering differential cross-section with respect to solid angle as a function of scattering angle for different initial photon energies.

angle as a function of the scattering angle θ, given by Klein and Nishina:

$$\frac{d\sigma}{d\Omega} = Zr_o^2\left(\frac{1}{1+\alpha(1-\cos\theta)}\right)^2\left(\frac{1+\cos^2\theta}{2}\right)\left(1+\frac{\alpha^2(1-\cos\theta)^2}{(1+\cos^2\theta)[1+\alpha(1-\cos\theta)]}\right), \quad (2.12)$$

with $\alpha = E_\gamma/m_ec^2$, the initial photon energy in units of the rest electron energy. The cross-sections for photons emitted by radionuclides listed in Table 2.1 are given. The forward scattering ($\theta < \pi/2$) is more probable, and the asymmetry increases with the initial photon energy.

Figure 2.10 shows the Compton scattering differential cross-section with respect to the energy transfer E_e of the interaction:

$$\frac{d\sigma}{dE_e} = Z\pi r_0^2\frac{mc^2}{E_\gamma^2}\left[1+\left(1-\frac{E_emc^2}{E_\gamma(E_\gamma-E_e)}\right)^2+\frac{E_e^2}{E_\gamma(E_\gamma-E_e)}\right]. \quad (2.13)$$

The dependency is shown for the same radionuclides as in Figure 2.9. The range of the transfer has a sharp limit at the Compton energy.

The total Compton scattering cross-section is the integral of 2.12 over the solid angle:

$$\sigma = 2Z\pi r_0^2\left[\frac{1+\alpha}{\alpha^2}\left\{2\frac{1+\alpha}{1+2\alpha}-\frac{1}{\alpha}\ln(1+2\alpha)\right\}+\frac{1}{2\alpha}\ln(1+2\alpha)-\frac{1+3\alpha}{(1+2\alpha)^2}\right]. \quad (2.14)$$

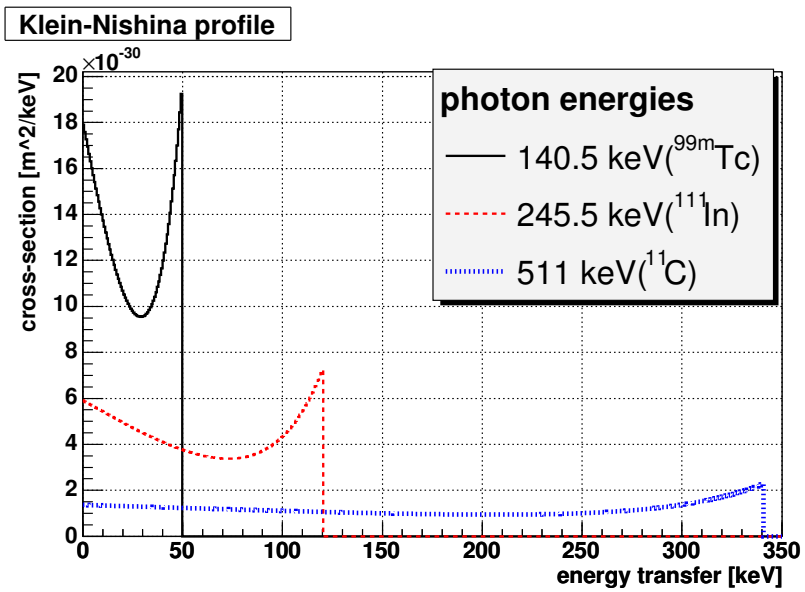

Figure 2.10: Compton scattering differential cross-section with respect to energy transfer, for different initial photon energies.

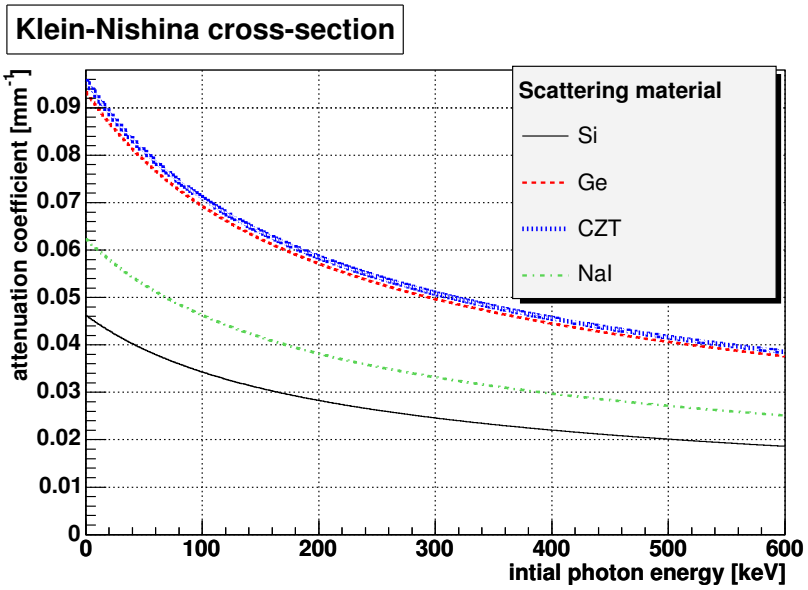

Figure 2.11: Attenuation coefficient of Compton scattering. Comparison for different scattering material.

The attenuation coefficient due to the Compton scattering is derived from (2.14) using relation (2.11) and shown in Figure 2.11 as a function of the initial photon energy for silicon,

germanium, CZT and NaI. The probability of Compton scattering decreases with growing photon energy, a factor of 2 incurred between 60 and 600 keV.

2.7 Photo-absorption

For photons with energy over approximately 10 keV and below 1.2 MeV the only relevant interactions are the Compton scattering and the photo-absorption. The Compton scattering was thoroughly described among the principles of the Compton camera, and this section is devoted to the description of the photo-absorption.

The importance of photo-absorption is related to the individual sensors of a Compton camera: in the scatterer, the photo-absorption is not desired for and in the absorber it is the main interaction. This is reflected in the material choice and will be discussed later in this section.

The photo-absorption is an interaction of photons, where the initial photon is completely absorbed by the atom, and a photo-electron with kinetic energy approximately equal to the initial photon energy is created. A part of the photon energy is used to extract the electron from the binding shell, and the subsequent rearrangement of the atom's electrons produces secondary radiation (X-rays or Auger electrons) with total energy equal to the missing energy. Photo- and Compton electrons are treated equally, where subsequent ionization is concerned, and if the secondary radiation is absorbed by the medium, the total measured ionization (providing the photo-electron stops in the detector) is proportional to the initial photon energy.

The angular distribution of the photo-electron direction is isotropic, since the nucleus absorbers the initial photon momentum. There is no single analytic expression giving dependency of μ over all ranges of Z and E_γ, but a rough approximation [Kno99] is:

$$\mu \propto \rho \frac{N_A}{A} \frac{Z^n}{E_\gamma^{3.5}}, \tag{2.15}$$

with exponent n varying between 4 and 5 depending on the initial photon energy. Exact dependence, shown in Figure 2.12 which compares μ in different scattering materials over the range of photon energies used in SPECT, is based on tabulated values [Sco73]. We see that NaI, the sensitive material of the absorber, has three orders of magnitude larger μ than silicon due to larger effective Z. The efficiency of the absorber with 1 cm thick NaI crystal is close to unity for photon energies up to 200 keV, but above that value the efficiency starts to drop significantly.

The interactions in an ideal scatterer would be limited to Compton scattering, and the ratio of Compton to total interaction probability would equal 1 in the whole energy range. Figure 2.13 shows the realistic ratios for various detection materials, with silicon being the closest to ideal. The thickness of silicon scatterer can be increased with almost no signal loss due to

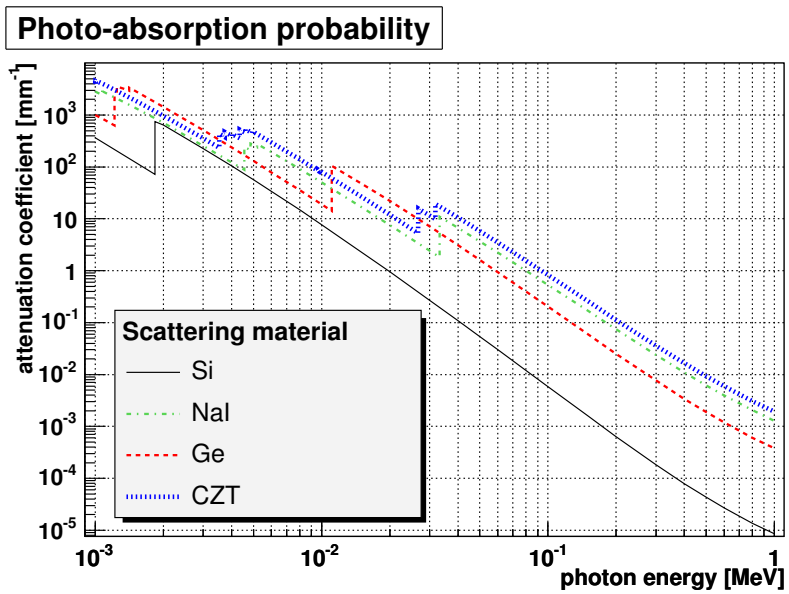

Figure 2.12: Photo-absorption attenuation coefficient as function of initial photon energy for various detector media. Data from [Sco73]. Both X and Y scale are logarithmic!

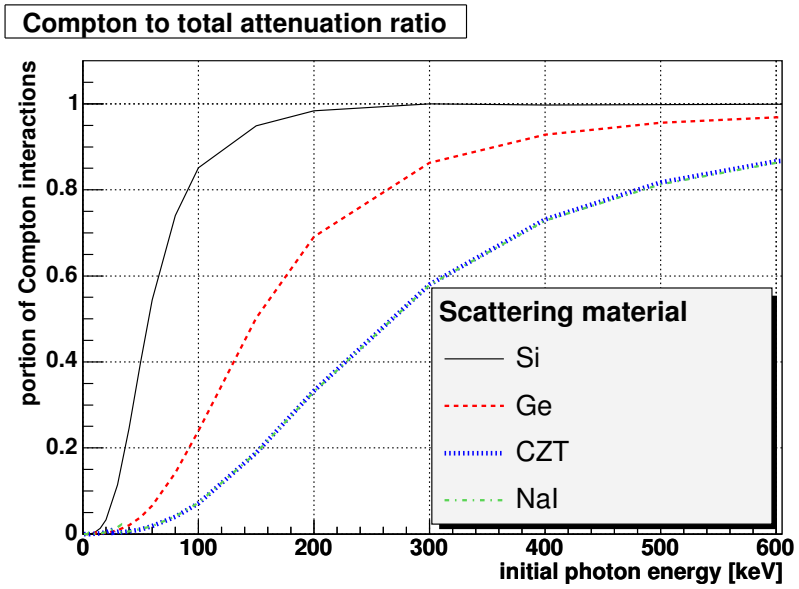

Figure 2.13: Compton to total attenuation ratio in various media, data from [Sco73, HVB$^+$75].

the photo-absorption, giving a great enhancement of the scatterer's efficiency, which is not the case for the rest of the listed detection material.

Chapter 3

Scatterer

As already described, the scatterer is the first sensor of a Compton camera in which the scattering of the initial photon takes place. The scatterer with the associated electronics has to provide several pieces of information: the location of the interaction, the measurement of the energy transfer and a trigger signal for timing correlation with the absorber. These requirements present complex technical challenges, causing previous Compton camera prototypes to fall somewhat short of their design goals. Because of that, we devoted special attention to development of the scatterer.

Recent years have seen substantial progress in the field of silicon sensors. Practically every major high energy physics experiment constructed in the last decade includes a set of position sensitive silicon detectors at its core. The potential for medical imaging applications, where X-ray and γ-rays are imaged, was also quickly recognized and silicon is by many claimed to be the best semiconductor detection material available. The following reasons favor it as the Compton camera scatterer material:

- suitable energy resolution at the room temperature,
- high resistivity substrates, giving manageable depletion voltages for 1 mm thick sensors,
- robustness,
- Doppler broadening is lower than in any other semiconductor material,
- high ratio of Compton to photo absorption interaction cross-section,
- manageable cost,
- excellent spatial resolution on the impact position.

The only draw-back of silicon as a γ-ray sensor is its low attenuation coefficient. The thickness of a sensor is limited by the production process and manageable depletion voltages, but stacking of sensors can increase efficiency, hence reducing the problem.

This chapter describes the development and performance of a Compton camera scatterer. First the properties of silicon pad sensors are given and the signal formation and operation conditions described. We continue with the description of electronic processing of the signal, with special attention given to the first stage of readout electronics embedded in an application specific integrated circuit (ASIC). Performance of the assembly in terms of energy resolution and timing properties is described and evaluated in terms of requirements of the Compton camera scatterer.

3.1 Basics of silicon pad sensor operation

Silicon is a semiconductor material and the common property of all semiconductors is a gap in the electron energy band structure around the Fermi level. This makes them insulators at low temperature and conductors with moderate resistivity at room temperature. The energy gap in silicon is 1.12 keV, and the resistivity of a pure (intrinsic) silicon sample at room temperature would be 300 kΩcm.

Years ago it was demonstrated that a semiconductor can be used as a particle detector, exhibiting high efficiency and energy and spatial resolutions. The invention became widely used and semiconductors are presently one of the most popular detector materials.

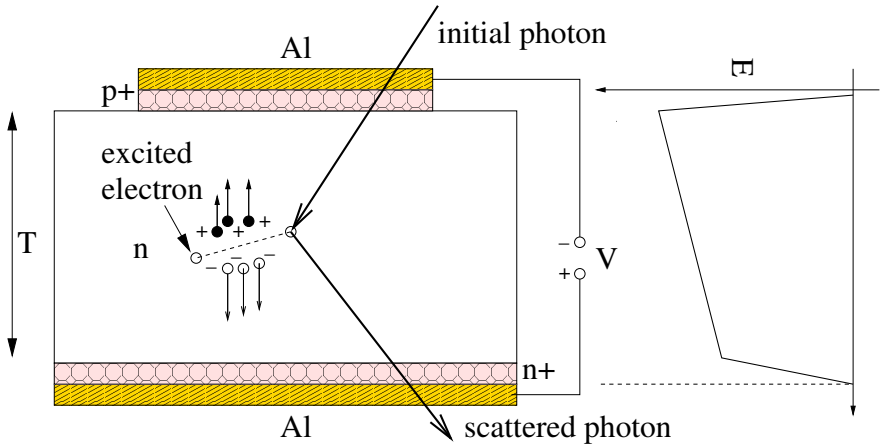

Figure 3.1: A sketch of a Compton interaction in a silicon p^+nn^+ diode.

A p^+nn^+ diode operating as a sensor is sketched in Figure 3.1. A pn junction is formed between the p^+ (top) and n layer of the diode. A reverse bias, applied over the metal contacts forms a depletion region around the junction. The dopant concentration of the p^+ layer is 10^6-times larger than the dopant concentration of the high resistivity n layer, therefore the depth of the depletion region in the p^+ layer is 10^3-times smaller than in the n-layer and can be thus ignored in the subsequent analysis. Both p^+ and n^+ layers with

similar dopant concentration assure ohmic contact of the semiconductor with the metal electrodes. Applying a voltage V across the junction in the reverse direction, the thickness of the depleted region, d is:

$$d = \sqrt{\frac{2V\varepsilon\varepsilon_0}{e_0 N_d}}, \tag{3.1}$$

with ε the dielectric constant of silicon, ε_0 the permittivity of free space, e_0 electron charge magnitude and N_d dopant (donor) concentration. The depletion region grows until full depletion is reached at V_{FD} and the depletion region extends throughout the sensor bulk:

$$V_{FD} = \frac{e_0 N_d w^2}{2\varepsilon\varepsilon_0}, \tag{3.2}$$

with w being the sensor thickness. The V_{FD} of the diode should be as low as possible to prevent possible damage caused to structures on the sensor surface by too high operating voltages and reduce the effect of large edge currents. Since V_{FD} grows as w^2 and thick sensors are required, N_d has to be small. The resistivity ϱ of an n-doped sample is given with:

$$\varrho = \frac{1}{N_d \mu_e e_0}, \tag{3.3}$$

with μ_e the electron mobility. Since N_d is low, the resistivity is high. Another important parameter is C, the capacitance of the sensor, which is decreasing with increasing width of the depletion region d and V as:

$$C = \frac{\varepsilon\varepsilon_0 S}{d} = S\sqrt{\frac{\varepsilon\varepsilon_0 e_0 N_d}{2V}}, \tag{3.4}$$

with S the sensor area, until the C_{FD}, the full depletion value is reached:

$$C_{FD} = \frac{\varepsilon\varepsilon_0 S}{w}. \tag{3.5}$$

Figure 3.1 also shows the mechanism of signal formation in the diode by Compton scattering. The electron, involved in Compton scattering (the Compton electron) creates electron-hole pairs along its path. Each created pair is split by the electric field: the holes drift towards the top (negative) electrode and the electrons to the bottom counterpart. Three properties of signal formation are important for a scatterer in a Compton camera: the shape of the signal produced by each of the created electron-hole pairs, the total number of created pairs, and the distance over which these pairs are created. The following paragraphs describe in turn each of these properties.

The number of electron-hole pairs produced by the Compton electron is proportional to its kinetic energy or the energy transfer of the interaction. The number of created electron-hole pairs is subject to fluctuations, since the energy is distributed among the created electron-hole pairs and phonon excitations. N_{e-h}, the average number of created pairs is given by:

$$N_{e-h} = \frac{E_e}{\eta}, \tag{3.6}$$

with η_{Si}=3.6 keV, the average energy required to create an electron-hole pair in silicon. Q, the total charge collected on the readout electrode is then:

$$Q = N_{e-h} e_0 = \frac{e_0 E_e}{\eta}. \tag{3.7}$$

For Compton edges of the radionuclides listed in Table 2.1, there are 13800, 33400 and 94600 electron-hole pairs created for ^{99m}Tc, ^{111}In and ^{11}C, respectively.

Fano[Fan47] calculated the fluctuation of N_{e-h}:

$$\sigma_F = \sqrt{F N_{e-h}}, \tag{3.8}$$

with F_{Si}=0.1, the Fano factor named after him. The fluctuation σ_F is much smaller than corresponding carrier number fluctuation of an ionization chamber and semiconductors have excellent intrinsic energy resolution. The error σ_F is given as a number of electrons, which leads to the convention that all errors on energy measurement in semiconductors are expressed in this units. The intrinsic error on N_{e-h} is given as 37, 57 and 97 e at Compton edges of ^{99m}Tc, ^{111}In and ^{11}C, respectively.

The Compton electron is causing ionization in the semiconductor until its energy falls below η, then it is swept to the electrode by the electric field. The total distance between the interaction point and the most distant secondary ionization point is called the electron range, and it plays an important role in the reconstruction of the interaction position. Since secondary ionization is a random process, the electron path is not a straight line, but a windy path with many abrupt turns and it is impossible to locate either the interaction point or the end of the track. The total signal is thus treated as a cloud of electron-hole pairs, with the position of the scattering as its center of weight. The inherent spatial resolution of a semiconductor when locating a photon interaction point is therefore the range of the Compton electron[1].

[1]The only exception to the rule occurs for electrons with ranges exceeding the volume of the sensor cell. If the length of the path is long enough and the energy of the electron high enough, the interaction end of the signal is calculated using Bethe-Bloch formula for differential energy loss as a function of electron energy. For medical imaging the initial photon energy is much too small, so the stated rule is valid.

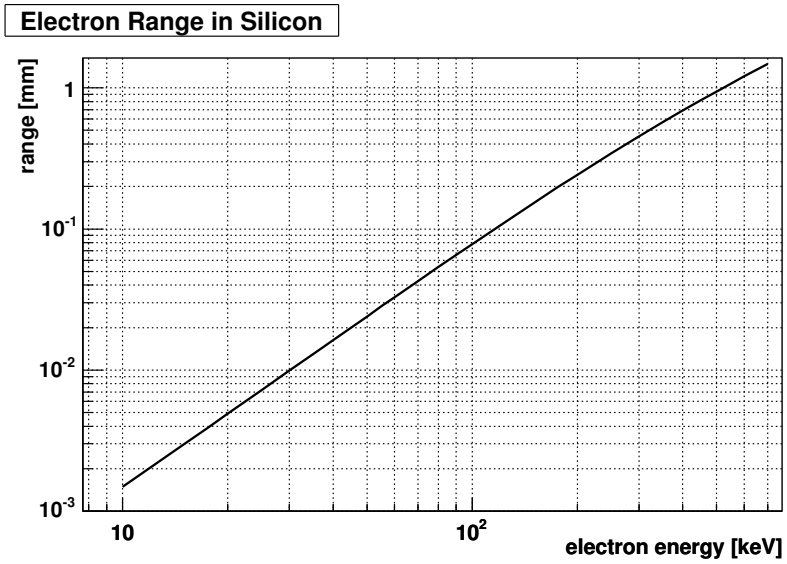

Figure 3.2: Range of electrons in silicon as a function of their kinetic energy. Data are taken from [UM84].

Figure 3.2 shows the range of electron in silicon as a function of its kinetic energy. The Compton electron range is 24, 110 and 550 μm for electrons with the Compton edge energy of ^{99m}Tc, ^{111}In and ^{11}C radionuclide, respectively.

Table 3.1 lists the important detection parameters of silicon as scatterer for radionuclides listed in Table 2.1. The maximum kinetic energy (the Compton edge) of Compton electrons was used to characterize the individual radionuclides.

Table 3.1: Silicon detection properties of the Compton electrons with maximum energy (the Compton edge) of the listed radionuclides.

Radionuclide	Photon energy [keV]	Compton edge [keV]	Number of created e-h pairs N_{e-h}	Error on N_{e-h}, σ_F	Electron range [mm]
^{99m}Tc	140.5	49.8	13847	37	0.024
^{111}In	245.5	120.3	33417	57	0.11
^{11}C	511	340.7	94630	97	0.55

In semiconductor detectors the signal presented to the electronics is the current induced on the electrodes by the moving carriers. The number of carriers is small enough that they can be treated separately and independently. According to the Ramo theorem[Ram39] a moving charge in an electric field induces a current pulse on the readout electrode with the current pulse shape $i(t)$ given by

$$i(t) = q\vec{\mathbf{v}}(t)\vec{\mathbf{E}_\mathbf{w}}, \tag{3.9}$$

where q is the charge of the carrier, $\vec{\mathbf{v}}$ its velocity and $\vec{\mathbf{E}_\mathbf{w}}$ the weighting potential. The

velocity of the carrier is related to $\vec{\mathbf{E}}$ the electric field:

$$\vec{\mathbf{v_i}} = \mu_i \vec{\mathbf{E}}, \tag{3.10}$$

with μ_i the carrier mobility and index i marking the carrier type (e-lectrons,h-oles). The electric field as a function of x, measured from the p^+n junction is given by:

$$E(x) = -\frac{V}{w} - \frac{e_0 N_d}{\varepsilon\varepsilon_0}\left(\frac{w}{2} - x\right), \tag{3.11}$$

where $V > V_{FD}$ is the applied reverse bias. The field is pointing towards, the coordinate system away from the p^+n junction, which makes the electric field (3.11) negative, as shown in Figure 3.1. It is convenient for a pad sensor fabrication to make the p^+ electrode the readout electrode so the current pulse shapes of each carrier type on that electrode will be calculated. The weighting field in a diode is constant and parallel to the electric field:

$$E_w = -1/w. \tag{3.12}$$

In a pad sensor the weighting field partially stretches towards the adjacent electrodes and equation (3.12) can be only treated as an approximation and used for an illustration of the produced pulse shapes.

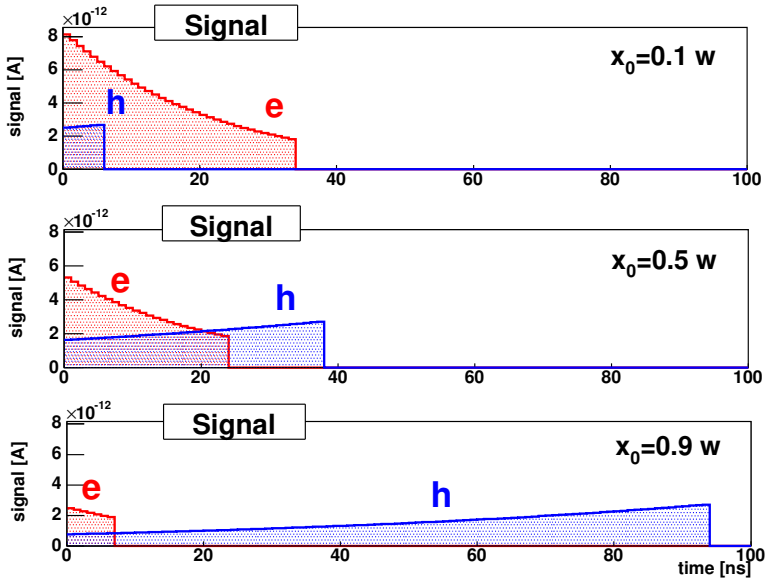

Figure 3.3: Raw signal produced in the silicon p^+nn^+ diode. Signal per electron-hole pair is given, with contribution of holes and electrons shown separately. The position of the interaction was chosen at 10, 50 and 90 % of the sensor thickness, with the origin set at the p^+n junction.

The equation of carrier motion (3.10) is solved to yield $v_i(t)$, which is combined with (3.12) and the Ramo pulse shape to yield the respective pulse shapes:

$$i_e = A\frac{e_0}{\tau_e}\mathrm{e}^{-\frac{t}{\tau_e}}, \tag{3.13}$$

$$i_h = A\frac{e_0}{\tau_h}\mathrm{e}^{\frac{t}{\tau_h}}, \tag{3.14}$$

with $\tau_i = \varepsilon\varepsilon_0/\mu_i e_0 N_d$, and A, dimensionless constant. A depends on x_0, the depth of interaction and V, the applied bias:

$$A = \frac{1}{2}\left(\frac{V}{V_{FD}} + 1\right) - \frac{x_0}{w}. \tag{3.15}$$

The resulting current shapes are shown in Figure 3.3. The bulk resistivity was chosen at ϱ =20kΩcm and applied voltage was set to 1.5 V_{FD}. The diode thickness enters the equation only through (3.2), yielding V_{FD}= 160 V for a sensor thickness of 1 mm. The contribution of both carrier types is shown separately and we see that the longest signal collection times occur for events occurring close to the n^+ layer of the silicon sensor, where a combination of a lower electric field and low mobility of holes is encountered. The collection times are shortened significantly with increased reverse bias.

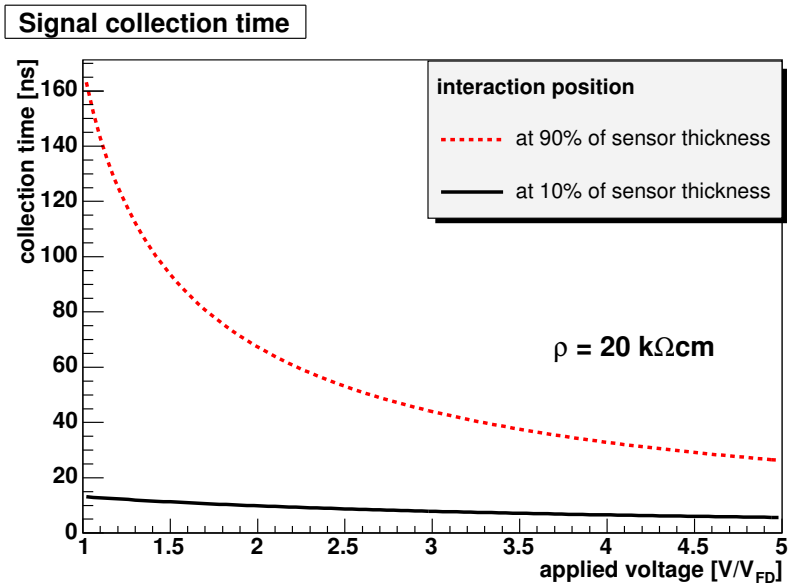

Figure 3.4: Collection time for signal in a silicon diode with ϱ=20 kΩcm as a function of the applied reverse bias. Comparison for events occurring at 10 and 90 % of the diode depth.

The time necessary to collect all charge generated in Figure 3.3 is t_c, the collection time, with the relation to x_0 shown in the figure. For events at the far edge of the diode, the

hole contribution is dominant and t_c^h, the collection time of the created holes is the relevant parameter. The situation is reversed at the near edge, with t_c^e, the collection time of the electrons. Both are derived from the integral $\int_{x_0}^{\text{EDGE}} dx/v$ and the velocity given by (3.10). The corresponding collection times are:

$$t_c^h = \tau_h \ln\left(\frac{1+\frac{V}{V_{FD}}}{1+\frac{V}{V_{FD}}-2\frac{x_0}{w}}\right), \tag{3.16}$$

$$t_c^e = \tau_e \ln\left(\frac{3+\frac{V}{V_{FD}}}{1+\frac{V}{V_{FD}}+2\frac{x_0}{w}}\right). \tag{3.17}$$

The combined collection time as a function of the depletion voltage is shown in Figure 3.4. Comparison for events occurring at near edge (10% of the diode depth) and the far edge (90% of the depth) is given. Over-biasing greatly improves the performance, with the collection time shortening for a factor of 2.5 when the voltage is varied from V_{FD} to $2V_{FD}$, for events occurring at the far edge.

3.2 Front-end electronics

The task of the front-end electronics is:

- to provide an analog signal proportional to the energy of the Compton electron
- to generate a timing trigger.

This is reflected in the circuit organization. The signal part generates the analog signal and the trigger part generates the trigger. The properties of each of the parts will be thoroughly discussed in the following subsections.

Further stages of electronics are more important in terms of data organization and communication. The second stage generates the operation parameters of the first stage, and collects and organizes the data. The next stage does the analog to digital conversion, packs the data into an event and communicates the data to the storage and control device, the PC. The computer is the last stage of the processing, managing task such as controlling the data flow, storing the data and performing off-line data analysis. Their importance on the data collection is not as crucial as the performance of the front-end, and they will be presented briefly later on.

To obtain position sensitivity, a segmentation of the sensor is required and this is reflected in parallelization of the front-end electronics into independent channels. The following discussion is limited to a single processing channel, but the actual circuit has to supply as many channels as there are pads in the diode array.

3.2.1 Signal part

The signal part of the front-end electronics has to provide an analog signal proportional to the energy of the Compton electron. The measured energy is then used for the scattering angle determination, via the Compton camera principle. Thus the measurement error will be reflected in the reconstructed source resolution. To maximize the resolution, a low-noise processing circuit is required.

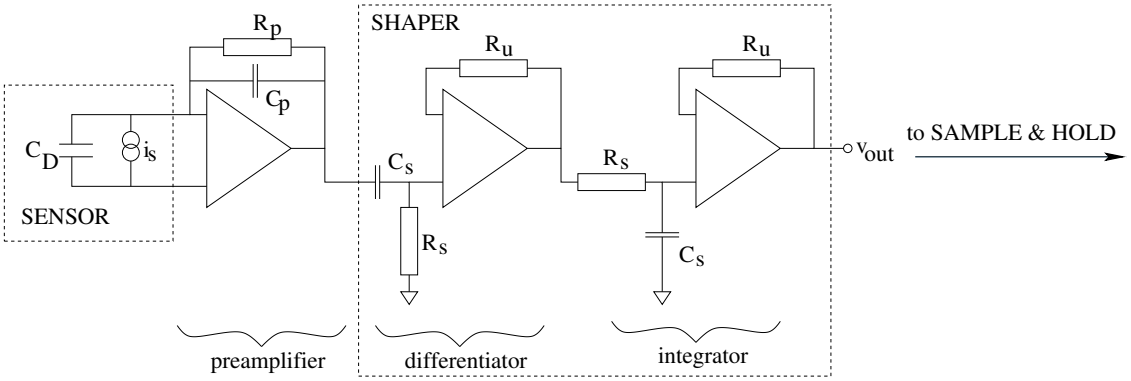

Figure 3.5: A schematic representation of the signal part of each channel of the front-end electronics circuit together with the sensor.

Figure 3.5 shows a schematic of the signal part circuit. The input is the diode signal current $i_s(t)$ and the output the voltage $v_{\text{out}}(t)$. The processing chain is composed of a charge-sensitive pre-amplifier and a CR-RC shaper.

The raw signal (Figure 3.3) is first integrated on a charge-sensitive pre-amplifier with a capacitive feed-back C_p. The input capacitance seen by the signal is A_pC_p, with A_p the amplification factor of the pre-amplifier, which exceeds the sensor capacitance C_d, and the charge is integrated over C_p. If no resistor is present in the feed-back, the output of the pre-amplifier is a constant voltage Q/C_p, proportional to the energy of the excited electron, cf. (3.7). A feed-back resistor R_p, is added to restore the base-line in $\tau_p = R_pC_p$, the pre-amplifier relaxation time. For an impulse, $Q\delta(t_0)$, the voltage at the output of the pre-amplifier is given by:

$$v_p(t) = \frac{Q}{C_p}\, \mathrm{e}^{-\frac{t-t_0}{\tau_p}}, \tag{3.18}$$

for $t > t_0$.

The next stage of the processing is the shaping of the pulse. There are two reasons for shaping the pre-amplifier output: to make the peak wider and to cut the band-width and thereby reduce the noise. In the pre-amplifier output (3.18), the energy is given by the pulse amplitude. The sharp peak strongly correlates the sampling amplitude time with the obtained value. To minimize this correlation, the shaper broadens the peak. The circuit of

3.5 shows a shaper made of a single differentiation stage (C-R) and a single integration stage (R-C) with equal characteristic time $\tau_s^E = R_s C_s$. The response of the circuit to an impulse ($\delta(t)$) is shown in Figure 3.6. The output of the pre-amplifier (equation (3.18)) is shown for comparison. The blow-up on the inset shows the rounded-off peak appearing at fixed time τ_s^E after the physical event. The negative peak of the shaper is called the undershoot and it is an artifact due to the zero-restoration part of the pre-amplifier. Indeed, the shaped pulse and the output of the pre-amplifier restore a zero voltage with the same relaxation time τ_p. Ignoring this, the shaped response to an impulse input is given with:

$$v_{\text{out}}(t) = \frac{Q}{C_p} \frac{(t - t_0)}{\tau_s} \mathrm{e}^{-\frac{t-t_0}{\tau_s^E}}. \tag{3.19}$$

The amplitude of the generated signal is proportional to the Compton electron energy and is given by:

$$v_{signal} = \frac{Q}{C_p \mathrm{e}}, \tag{3.20}$$

where e is the base of ln. The amplitude is extracted from the pulse by a SAMPLE & HOLD circuit which will be described later in this chapter.

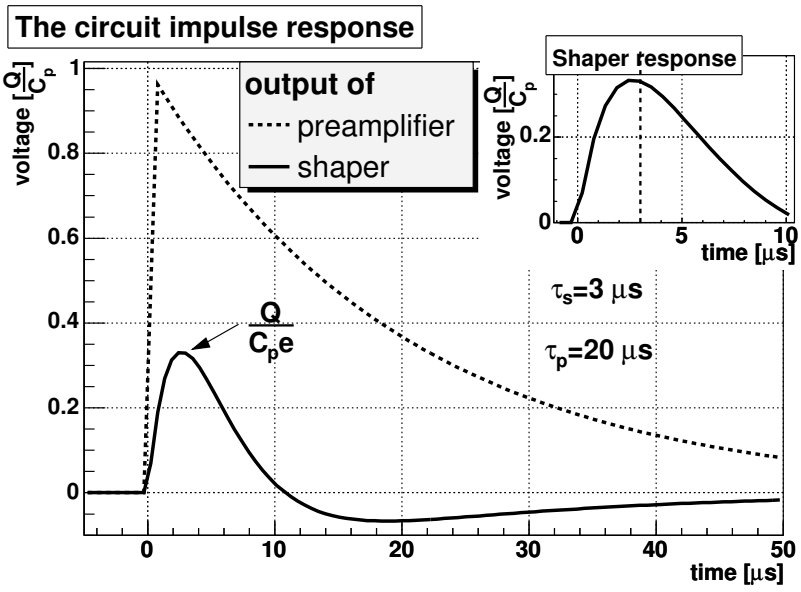

Figure 3.6: Impulse response of a pre-amplifier with characteristic time $\tau_p = 20\mu s$ and a shaper with $\tau_s^E = 3\mu s$. The impulse integral equals Q, the pre-amplifier feed-back capacitance C_p. The characteristic times resemble those of the actual prototype.

The signal is super-imposed on the fluctuating base-line. The error on the sampled amplitude is therefore equal to base-line variation, which is also called the noise of the signal. The signal is a voltage pulse, and the noise V_n is most naturally expressed in volts, but since we

are interested in the collected charge Q and related energy E_e, it will be expressed as an equivalent noise charge (ENC) σ_n or energy resolution Δ_E. The relation to V_n is extracted using relations (3.20) and (3.7):

$$\sigma_n = V_n C_p \mathrm{e}, \tag{3.21}$$

$$\Delta_E \ = (2.35 \times \eta)\sigma_n \ = \ 8.5 \times V_n C_p \mathrm{e}. \tag{3.22}$$

The energy resolution Δ_E is expressed as FWHM and the ENC as the variance of the distribution of the base-line fluctuations, and the factor $2\sqrt{2\ln(2)} = 2.35$ converts the variance to FWHM, and the combined value of 8.5 includes the silicon specific η_{Si}=3.6. The following discussion will derive the variance of the fluctuation based on spectral power densities of noise sources appearing in processing chain.

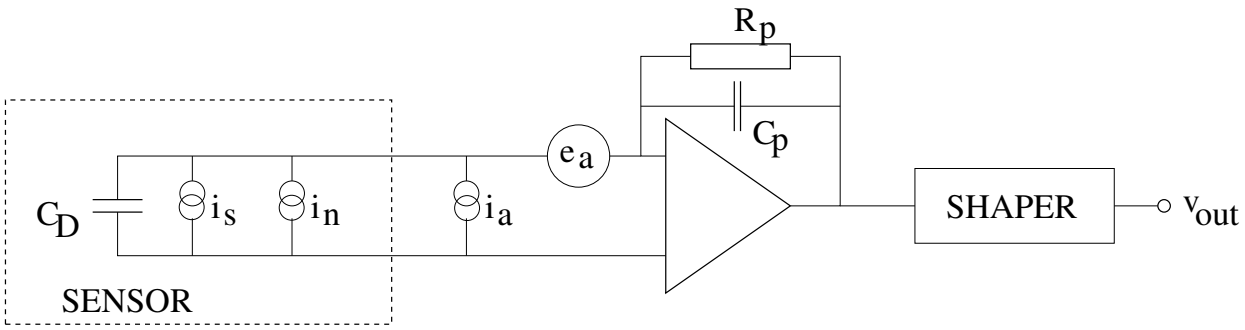

Figure 3.7: A schematic representation of the front-end electronics circuit and the sensor, including the noise sources.

Figure 3.7 shows the circuit schematic, including noise sources, which can be treated either as voltage or current sources. The current sources come in parallel with the signal source and are also called parallel, while the voltage sources are in series with the signal. The treatment is reflected in units of their power spectral densities: V^2/Hz or A^2/Hz for voltage or current sources, with spectral densities of both types frequency independent, or white in nature.

There are two major sources of noise: the sensor and the pre-amplifier. The sensor noise i_n is the shot noise due to I_d, the current flowing through the diode in the reverse bias mode, with spectral power density:

$$i_n^2 = 2e_0 I_d. \tag{3.23}$$

The noise of the amplifier is a combination of e_a, the voltage and i_a the current source with associated spectral densities, which are quoted in the amplifier documentation. The amplifier internal noise is only treated as an input noise, but appears in fact at the amplifier output. The noise sources are not correlated and therefore added in quadrature. The derivation of the noise appearing at the circuit output (v_{out}) is given in Appendix A. The ENC of the

output is determined to be:

$$\sigma_n = \sqrt{\frac{\mathrm{e}^2}{8}\left(e_a^2 C^2 \ \frac{1}{\tau_s} + (2e_0 I_d + i_a^2)\ \tau_s\right)}, \tag{3.24}$$

with $C = C_d + C_p + C_r + C_{in}$ the total capacitance seen by the pre-amplifier, including C_{in}, the amplifier input capacitance and C_r, the stray capacitance which includes the capacitance of the lines connecting the sensor output and the pre-amplifier. In order to reduce C_r the proximity of electronics and sensor is of vital importance. Equation 3.24 has an optimization parameter, τ_s, which can be selected to minimize σ_n. The shape of (3.24) ensures the existence of a minimum:

$$\tau_s^E = \frac{e_a C}{\sqrt{2e_0 I_d + i_a^2}}, \tag{3.25}$$

which depends on the diode current and the parameters of the amplifier.

3.2.2 Trigger part

The trigger gives a logic pulse signaling that an event has occurred. A similar signal is generated in the absorber, and the timing correlation of both triggers is used to match the Compton scattering event in the scatterer with the absorption of the scattered photon in the absorber, making the coherence of the scatterer and absorber trigger of vital importance. Another important parameter is the minimal energy of the Compton electron required for separation of a scattering event from the electronic noise. This energy determines the range of detectable scattering angles via the Compton relation (2.1). Compton camera performs best in a certain scattering angle range and the reduction of this range with a threshold cut decreases the efficiency of the camera, hence reducing the image quality.

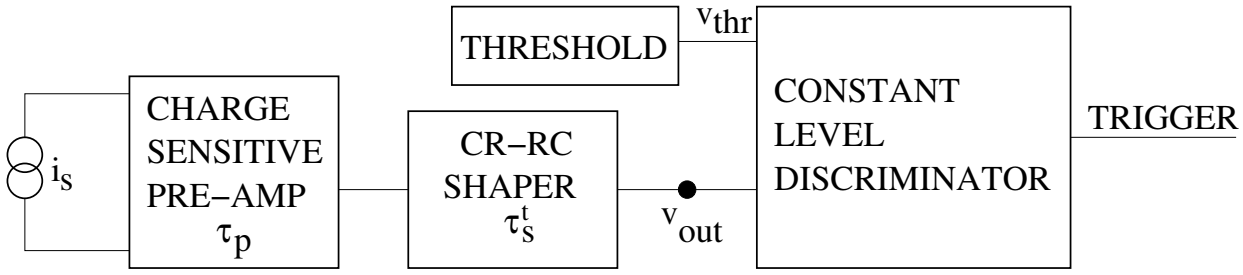

Figure 3.8: A schematic representation of the trigger generation.

The trigger generation circuit is shown in Figure 3.8 and can be divided into the analog part ending at the discriminator input with the voltage pulse v_{out} and the digital part which generates the trigger at the moment the pulse v_{out} crosses the analog threshold v_{thr}. The

important parameters of the trigger are the timing resolution and the minimal detectable energy for a given noise rate.

Minimal detectable energy. The derivation of the minimal detectable energy of the interaction electron is given in two parts: first the minimal detectable charge is calculated and then the corresponding energy. The minimal detectable charge is related to the ENC of the analog trigger part. The parameters of the analog output v_{out} are described by the equations derived for the analog signal (3.24,3.20), since the architectures of the trigger analog part and the analog signal are identical (shown in Figure 3.5). Furthermore, since the trigger shaping time τ_s^t is much shorter than the shaping time τ_s^E, which minimizes (3.24), the noise in the trigger pulse is dominated by voltage noise of the pre-amplifier and current noise can be ignored. Hence, the noise (ENC) of the trigger analog pulse is approximated by:

$$\sigma_n^t = \frac{\mathrm{e}}{2\sqrt{2}} e_a C \, \frac{1}{\sqrt{\tau_s^t}}, \tag{3.26}$$

and the minimal charge giving an analog pulse exceeding the threshold voltage is given by $Q_{min} = v_{thr} C_p e$ using equation (3.20). The distribution of base-line fluctuation amplitudes is Gaussian, and the rate of excursions exceeding voltage v_{thr} (or charge Q_{min}) is given with [Ric45]:

$$f_n = \frac{1}{4\sqrt{3}\tau_s^t} \mathrm{e}^{-\frac{Q_{min}^2}{2(\sigma_n^t)^2}}, \tag{3.27}$$

Selecting a rate of noise triggers f_r which can be tolerated in an operating setup sets Q_{min}, by inversion of (3.27):

$$Q_{min} = \sigma_n^t \sqrt{-2 \log\left(4\sqrt{3}\tau_s f_r\right)}. \tag{3.28}$$

Expressing the rate of noise triggers as:

$$f_r = 10^{-\alpha_r}/\tau_s^t, \tag{3.29}$$

the minimal detectable charge for a fixed σ_n^t is given by:

$$Q_{min} = \sqrt{4.6\alpha_r - 3.9}\sigma_t. \tag{3.30}$$

For example, $\alpha_r = 6$ gives Q_{min}=$5\sigma_n^t$. The minimal detectable energy can be further compromised by a charge loss due to τ_s^t shorter than the charge collection time t_c. The effect is characterized by a factor B representing charge collection efficiency, with $B \leq 1$. Since charge collection time t_c (equations (3.17) and (3.16)) depends on the position of the interaction, the same is valid for charge collection efficiency. The charge collected on the electrode is $Q_c = BQ = BE_e e_0/\eta$, and the minimum detectable energy $E_{e,min}$ of the interaction electron is:

$$E_{e,min} = \frac{\eta}{B \, e_0} \, Q_{min}. \tag{3.31}$$

Timing resolution. Two sources contribute to timing resolution of the trigger signal: the jitter and the time-walk. The source of the jitter is the base-line fluctuation: the analog voltage $v_{\text{out}}(t)$ is the sum of the signal and the fluctuation and the voltage v_{thr} may be exceeded sooner or later than the time designated by the signal alone. For small fluctuations, the distribution of the trigger time will be Gaussian, centered at the trigger time of the bare signal and the width σ_{jitter} given by:

$$\sigma_{\text{jitter}} = \frac{V_n^t}{\frac{dv_{\text{out}}}{dt}}, \tag{3.32}$$

with dv_{out}/dt the slope of the voltage pulse at the time of the trigger, and the V_n^t the noise of the analog trigger pulse. The slope is estimated using the impulse response (3.19), evaluated for $t < \tau_s^t$ as $v_{\text{out}}(t) = \frac{t}{\tau_s^t}\frac{Q}{C_p\text{e}}$, with the derivative:

$$\frac{dv_{\text{out}}}{dt} = \frac{1}{\tau_s^t}\frac{Q}{C_p\text{e}}. \tag{3.33}$$

Converting V_n^t to (ENC) σ_n^t (3.21) and inserting expression (3.33) back into (3.32), the variance of the jitter is obtained:

$$\sigma_{\text{jitter}} = \frac{\sigma_n^t}{Q}\tau_s^t, \tag{3.34}$$

proportional to τ_s^t for a fixed ENC σ_n^t and Q, the signal charge. For example - setting the charge Q=$2Q_{min}$, which sets the threshold at $Q/2$, the slope of the pulse at the threshold is well approximated with (3.33) giving a jitter of approximately $\sigma_{\text{jitter}} = \tau_s^t/10$.

The time-walk originates in dependence of the trigger time on the energy of the detected Compton electron. Since the energy information is not available when the events of the scatterer and the absorber are matched, this dependence should be minimized for a proper event matching. The time-walk is illustrated on the inset of Figure 3.9, showing the trigger timing difference of a signal pair: one with the minimal detectable charge Q_{min} and another with 5-times larger amplitude. This is a good approximation of the situation encountered in a Compton electron detection: the electron energy spectrum is a continuum and all possible charges between Q_{min} and the maximum detectable charge Q_{max},(the Compton edge) are detected, and the ratio $r = Q_{max}/Q_{min}$ is fixed for a given threshold. The large curve shows the time difference of such signal pairs as a function of r, in units of the shaping time. With r of 5 and more encountered in a real system, the time-walk is well approximated with the shaping time τ_s^t.

The jitter and the time-walk are both proportional to τ_s^t, and minimized for $\tau_s^t \rightarrow 0$. The proportionality is valid until τ_s^t is decreased to values comparable with the charge collection time t_c. Below that limit the charge collection efficiency B drops, which also decreases the signal rise time and the derivative dV/dt. To assess the effects of finite t_c, the sensor response $i_s(t)$ was modeled by a square function of duration t_c.

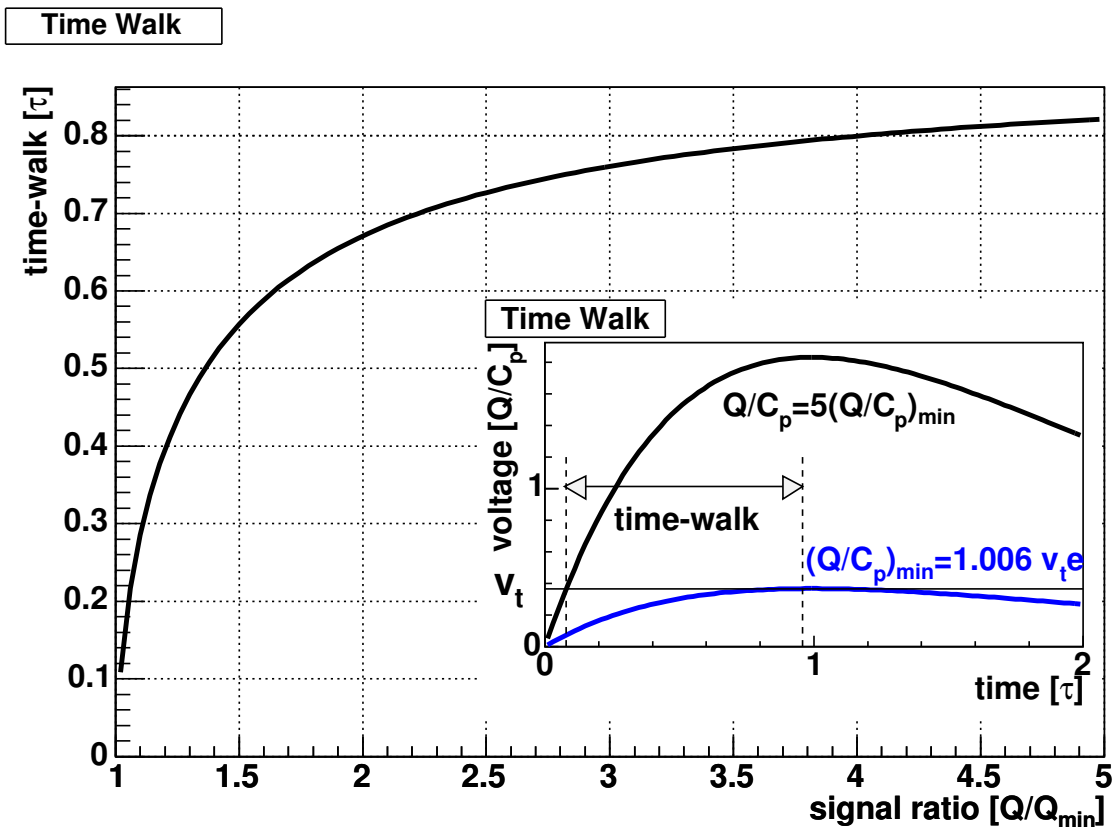

Figure 3.9: An illustration of the time-walk generated by a constant level discriminator. Large graph: the time walk as a function of the ratio of the detected signal amplitudes. Inset: the time walk for a fixed signal ratio of 5, the minimum detectable signal given by $(Q/C_p)_{min}$=1.006$v_{thr}e$.

The dashed line of Figure 3.10 shows the collected charge efficiency B as a function of the shaping time decreasing below t_c. A deficit of 10% is estimated for $\tau_s^t = 0.8t_c$, which increases E_{min} by the same amount. The solid curve shows the time-walk for fixed $r = 5$, with the linear decrement in the $\tau_s \gg t_c$ range tailing off to a constant of t_c for $\tau_s^t \ll t_c$. The jitter is increased by the smaller slope response, the maximum derivative changing from $1/\tau_s^t$ to $1/\tau_s^t \exp(-t_c/\tau_s^t)$. Combining the above facts we realize that a shortening of the τ_s^t in the range below t_c does not improve timing properties of the trigger pulse, it only causes deterioration of the signal amplitude. The shaping time is optimized for $\tau_s^t > t_c$, with the exact value a compromise between the minimum detectable energy, falling as $1/\sqrt{\tau_s^t}$ and the timing error, growing linearly with τ_s^t.

To conclude, the trigger of the scatterer is derived using the circuit 3.8. The jitter and time-walk of the trigger are minimized for τ_s^t as short as possible and the best timing performance is achieved for $\tau_s^t \approx t_c$. In that range, the minimum detectable energy is increased by the

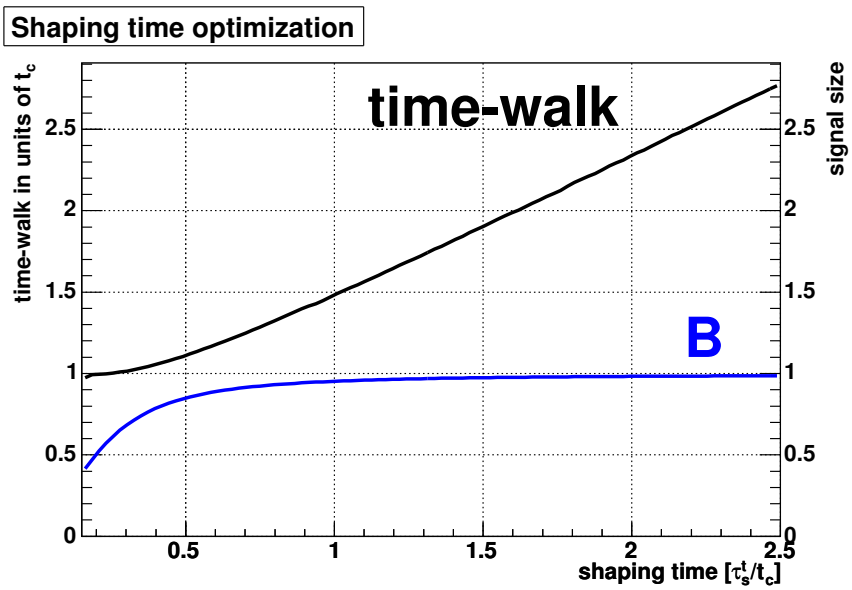

Figure 3.10: The time-walk for a fixed Q_{max}/Q_{min}=5 in units of t_c and the ballistic deficit, both as a function of τ_s/t_c.

charge collection efficiency and the optimal trigger performance is achieved for $\tau_s^t > t_c$, with the exact value a compromise between the minimal detectable energy and the timing error. The ENC (σ_n^t) is dominated by voltage noise of the amplifier and increases with $1/\sqrt{\tau_s^t}$ and is very sensitive to the input capacitance C. The timing error falls linearly with decreasing τ_s^t, with time walk approximately equal to τ_s^t. For a noise trigger rate of $10^{-6}/\tau_s^t$, the minimum detectable charge is $Q_{min} = 5\sigma_n^t$, and the variance related to jitter for pulses barely exceeding threshold equals $\sigma_{\text{jitter}} = \tau_s^t/5$.

3.3 Scatterer module assembly

The previous section concluded the theoretical aspects of scatterer design considerations and the chapter continues with the presentation of the actual assembly used. The scatterer module consists of a silicon pad sensor and the front-end electronics, realized as an application specific integrated circuit (ASIC) embedded on a micro-chip. This section will implement the considerations discussed in the previous sections.

3.3.1 Silicon pad sensor

Encouraged by performance of earlier detectors [WND+96], a new batch of silicon sensors was designed[2] specifically for the Compton camera scatterer. This part will describe the sensor layout and the fabrication procedure. The important parameters of the sensor are the pad size (with related spatial resolution) and the production dependent current-voltage (I-V) and capacitance-voltage (C-V) characteristics.

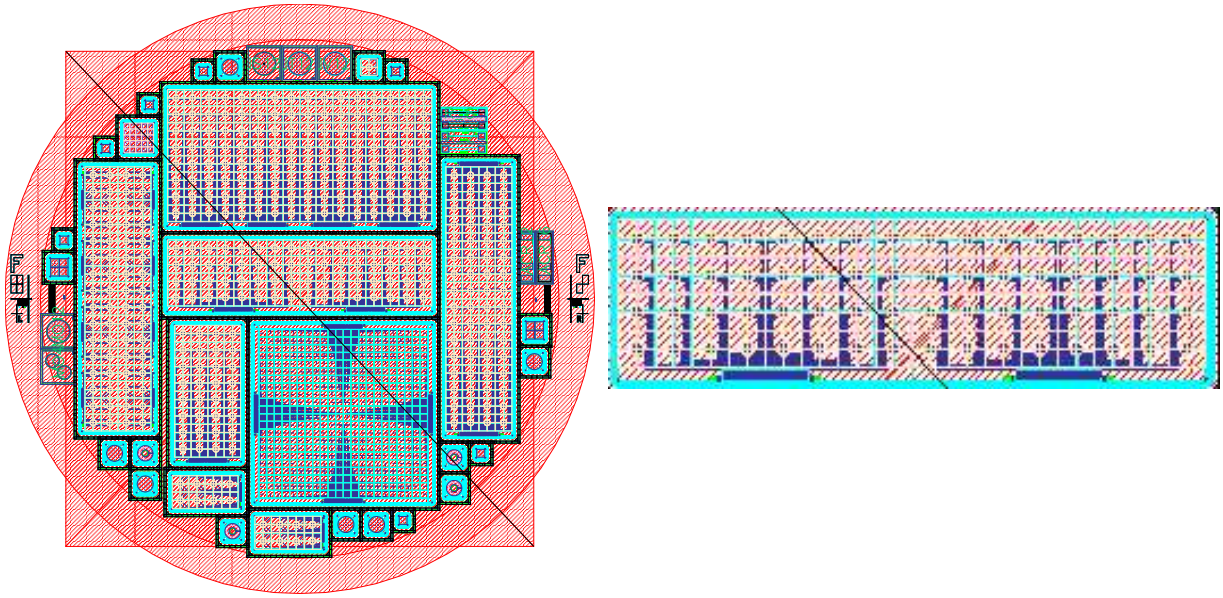

Figure 3.11: Left: Layout of the wafer containing sensors for different applications. Right: Layout of the sensor selected for the scatterer of the Compton camera prototype.

Sensors with thickness of 500 μm and 1 mm, exceeding the standard particle detector thickness of 300 μm, were fabricated and tested to evaluate the influence of increased thickness. The sensor with layout shown in Figure 3.11 and a pad size of 1.4×1.4 mm^2 was selected for the scatterer. The sensor consists of 256 pads, arranged in an 32 by 8 array. The cross-section of the sensor is shown in Figure 3.12. Two metal layers are used: the bottom layer is segmented into pads, each pad directly connected (DC coupled) to the respective p^+ implant to collect the signal charge, and the lines in the top layer route the signals from the pad to the side of the detector where pads for connection to the ASIC are available. The metal layers are separated by a 10 μm thick insulating layer of polyimide, which is also used for sensor passivation. A guard ring structure is employed to reduce the influence of edge effects on sensor parameters.

The sensors were manufactured and processed by SINTEF[3]. The basis of the sensor is a

[2]Sensors designed by W. Dulinski, LEPSI, Strassbourg, France.

[3]The Foundation for Scientific and Industrial Research at the Norwegian Institute of Technology (NTH),

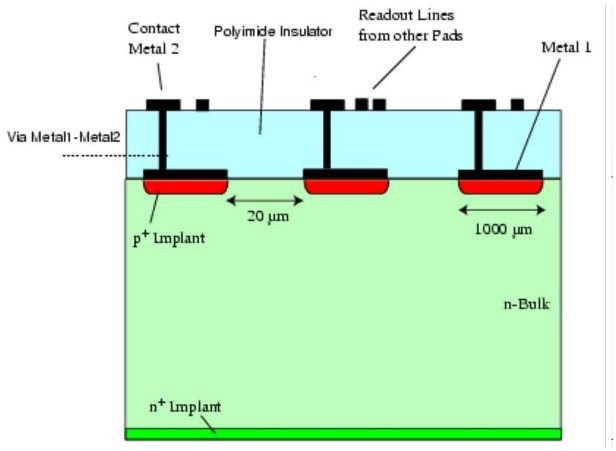

Figure 3.12: Schematic drawing of the cross-section of silicon pad sensor. An additional metal layer (Metal 2) bears the readout lines which route the signals from pad electrodes on bottom metal layer (Metal 1) to bonding pads at the sensor's side, and polyimide is used to insulate Metal 1 from Metal 2.

single silicon crystal with a very low concentration of impurities, save for the donor dopants required for the p^+nn^+ diode construction. The dopant density should only suffice to mask the impurity effects and the required high resistivity is met with a careful sample purification. The crystal is subsequently cut into thin slices (or wafers), which are processed independently. The sensor processing is based on the planar technology developed for micro-electronics, but the purity of the crystal sample requires special equipment and procedures.

To construct the pads, photo-lithography, followed by etching and dopant implantation (boron for implants forming p^+ layer) is used. The back side is treated in a similar manner, with a n^+ layer stretching over the whole sensor surface. The metal electrodes are formed using metal deposition and the sensor is passivated with polyimide, providing stress and electronic protection. After cutting and testing, the sensors can be mounted on the prototype and connected to the electronics.

Figure 3.13 shows static properties of the silicon sensors. From capacitance-voltage (CV) dependence, a typical full depletion voltage of $V_{FD} = 130V$ of 1 mm sensors can be inferred, and current-voltage characteristics shows a typical diode current of a single pad not exceeding 100 pA.

Trondheim, Norway, `http://www.sintef.no`

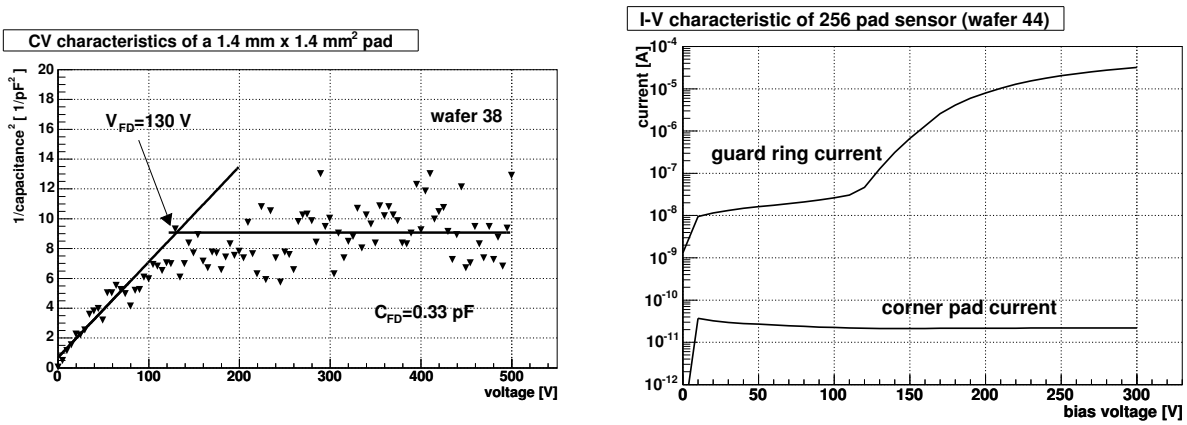

(a) (b)

Figure 3.13: Static properties of 1 mm thick silicon sensors: (a) Capacitance-voltage (CV) characteristic of a typical sensor, showing V_{FD} and C_{FD}. (b) Current-voltage (I-V) characteristic, showing a corner pad current and the current of the guard ring. Logarithmic scale on the y-axis is used to combine graphs.

3.3.2 ASIC

The application specific integrated circuit (ASIC) provides the front-end electronics for each of the detector pads. An off-the-shelf ASIC was chosen to minimize the design and fabrication time, and the VATAGP chip family, designed and fabricated by IDEAS[4] is a good match for the scatterer requirements. The chip selected for the prototype was a 128 readout channel VATAGP3 chip, each sensor read by two chips, with the layout of the chip input pads matching the layout of the signal connection pads of the sensor.

The chip functional schematic is shown in Figure 3.14. The core of the circuit is the generation of the analog and trigger signal for each readout channel, which implements the schematic introduced and discussed in Section 3.2. A special section of this chapter is devoted to the analog and the trigger signal properties of VATAGP3. The continuation of this part will describe the peripheral circuits which determine the function of the core: the `bias`es, the `mask`, the SAMPLE & HOLD circuit and the analog signal multiplexers.

The analog parameters of the core circuit are determined by the `biases`, analog DC voltage signals applied to the designated inputs on the VATAGP3. To list the most important, bias `vfp` determines the feed-back resistor value of the pre-amplifier, `vfsf` the shaping time of the fast and `vfss` the shaping time of the slow shaper, both over a limited range. There is also a master bias `mbias` which sets all biases to an optimal value according to a preset map, optimized in the chip simulation, and the rest can be left unconnected.

The parameters of the chip for a specific run are controlled via a sequence of bits called a

[4]Ideas ASA, Snarøya, Norway,`http://www.ideas.no`

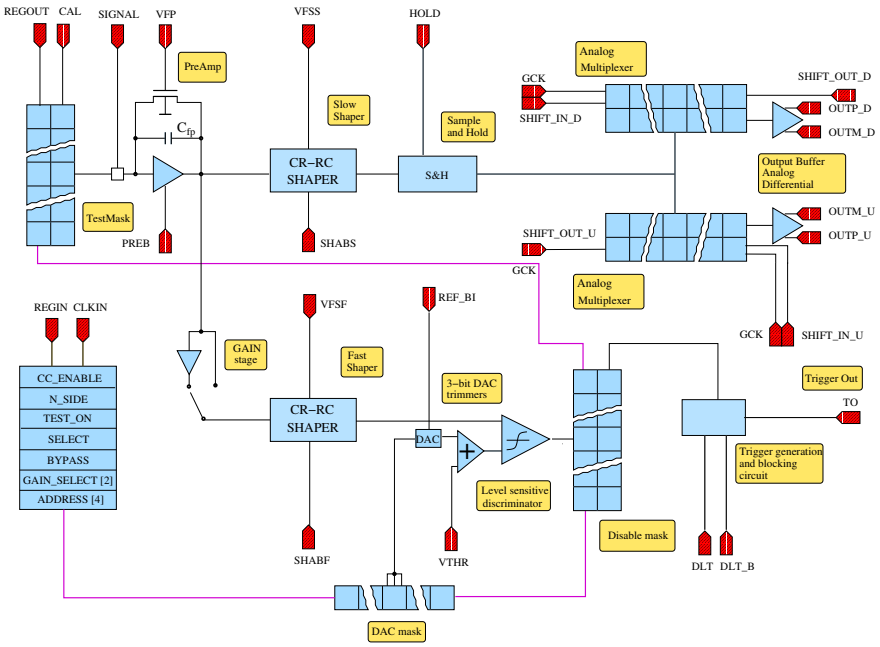

Figure 3.14: Approximate schematic of a single readout channel of VATAGP3 ASIC. The schematic also includes the signals determining the overall chip performance (shaping times of the fast and the slow shaper, feed-back resistor of the pre-amplifier, trigger, test and DAC align masks, gain setting,...).

`mask`, which is downloaded to the chip before the run. The full mask consists of two parts: the chip specific settings and the masks for each of the readout channel: the `test mask`, the `trigger mask` and the `DAC mask`. The `test mask` is combined with the `TEST` bit of the chip specific settings, and sets the chip into the TEST mode, which enables charge injection directly into the readout channel, determined by the `test mask`. The channels set in the `trigger mask` are prevented from triggering, and noisy channels can be masked away. The `DAC mask` is a 3-bit wide channel-specific correction of the common trigger threshold voltage, with the voltage step of a bit determined by `mbias`.

The role of the SAMPLE & HOLD circuit is illustrated in Figure 3.15. The screen-dump of an oscilloscope shows the following traces: the top line is the charge injection – a voltage step discharged over a capacitor, the second line is the generated trigger, the third line is the externally applied `HOLD` signal, which triggers the SAMPLE & HOLD circuit that fixes the value of the analog output. The peak of the analog pulse (the bottom trace) is sampled by a proper adjustment of the delay between the trigger and the `HOLD` signal.

The sampled value of the analog outputs of all channels are stored in a pair of multiplexers (UP and DOWN). Each multiplexer is shifted by the higher level electronics, making the sampled analog value available on the output buffer. The DOWN multiplexer is shifted in descending and the UP multiplexer in ascending order with respect to the readout channel

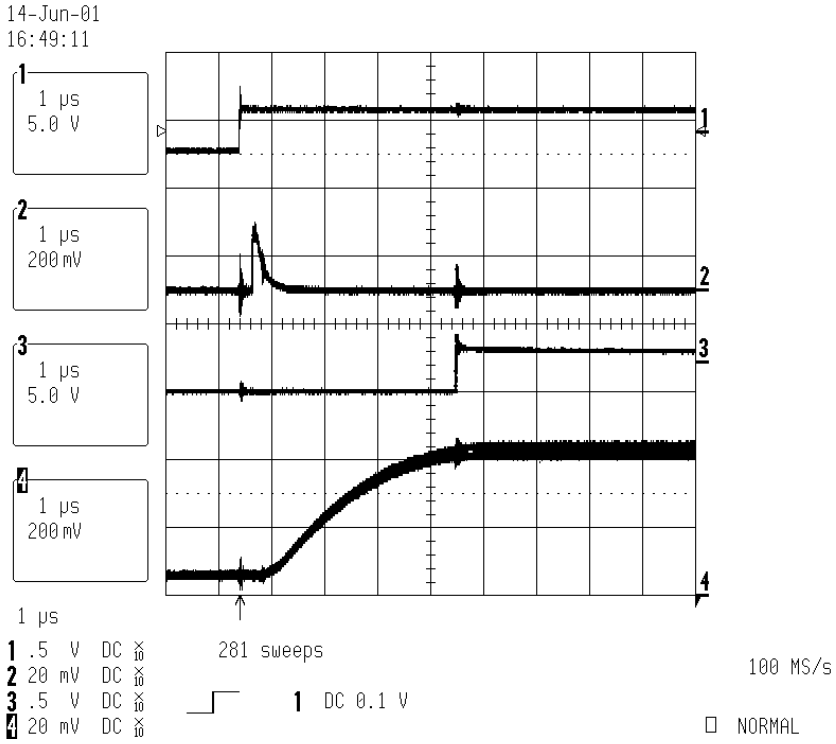

Figure 3.15: Oscilloscope screen-shot of test charge injection into VATAGP3. The top trace shows the voltage step which, discharged over a capacitor, injects charge into a readout channel input. The second trace is the digital trigger pulse generated by the chip. The third trace is the externally applied HOLD signal which fixes the voltage level of the analog signal. The analog signal is the bottom trace with a constant (held) value when the HOLD signal is applied. The noise observed on the analog line is an artifact of the oscilloscope probe.

number. Using the pair of the multiplexers, there are three ways of reading the analog values from the buffer:

- Serial readout. The DOWN (UP) output produces all channel samples from the first (last) to the last (first) channel.
- Sparse readout. The channel that triggered is stored in a buffer and only the hit channel signal is available on both outputs.
- Sparse with adjacent channels readout. After the channel that triggered (i), on output DOWN (UP) the samples of channels i+1 (i-1), i+2 (i-2), etc., are available.[5]

[5]Note that channels adjacent on the readout chip are not neccesserarly adjacent in the pad space of the sensor.

.

The chip produces a trigger[6], if the (trigger) analog signal exceeds the threshold voltage `vthr` in any of the channels not masked by the `trigger mask`. During readout the generation of further triggers in the chip is blocked by a high level of `DLT/DLTB` logic signal.

3.3.3 Scatterer module

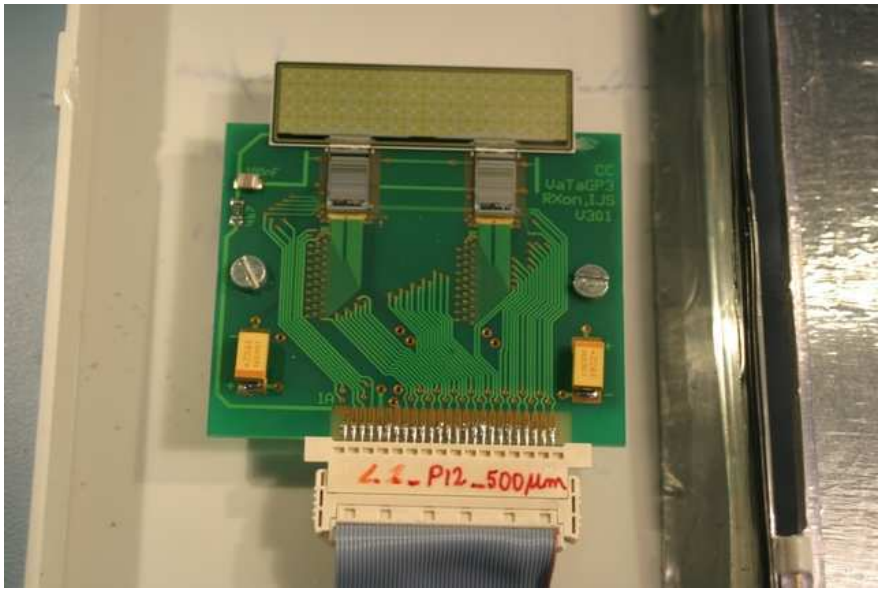

Figure 3.16: A photo of the scatterer module, containing the silicon pad sensor bonded to a pair of VATAGP3 chips on a PCB hybrid.

Figure 3.16 shows a photo of the scatterer module, consisting of a silicon sensor and a pair of VATAGP3 chips on a hybrid. The hybrid is a printed circuit board (PCB), which routes and fans out the chip signals and provides mechanical support for the chips and the sensor. The sensor-chip inter-connections are formed with wire-bonds, 22 μm thick wires bonded with ultra-sound to the respective metal contacts. The same technology is used to connect the chip contacts to the traces on the PCB.

Mechanically, the hybrid is an approximately 70 mm wide and 85 mm long board, the sensor measures approximately 45 mm by 12 mm and the ASIC is a 0.6 mm thick, 7 mm wide and 10 mm long silicon die. The sensor is glued to the hybrid, conductive glue electrically connecting the back-side electrode to the sensor bias trace on the hybrid. The sensor top electrodes are connected to the inputs of the chip, which hold the top electrodes at ground potential. The sensor is biased using a positive voltage applied to the sensor back-side.

[6]The trigger pulse produced by the chip is also referred to as a fast-or (FOR).

3.4 Data acquisition and processing

3.4.1 Data acquisition

The scatterer module is driven by a data acquisition (DAQ) system. The DAQ system provides signals controlling chip operation and managing data flow. The custom designed DAQ system for the scatterer module is sketched in Figure 3.17. It consists of four parts: the distribution board, the intermediate board, the VME board and a personal computer (PC). The function of each will be described briefly.

The task of the distribution board is the routing of signals between the intermediate board and the individual modules. The distribution board allows for more scatterer modules to be connected to the same readout chain, providing a simple way for sensor stacking, increasing the photon interaction probability and thus the full scatterer efficiency.

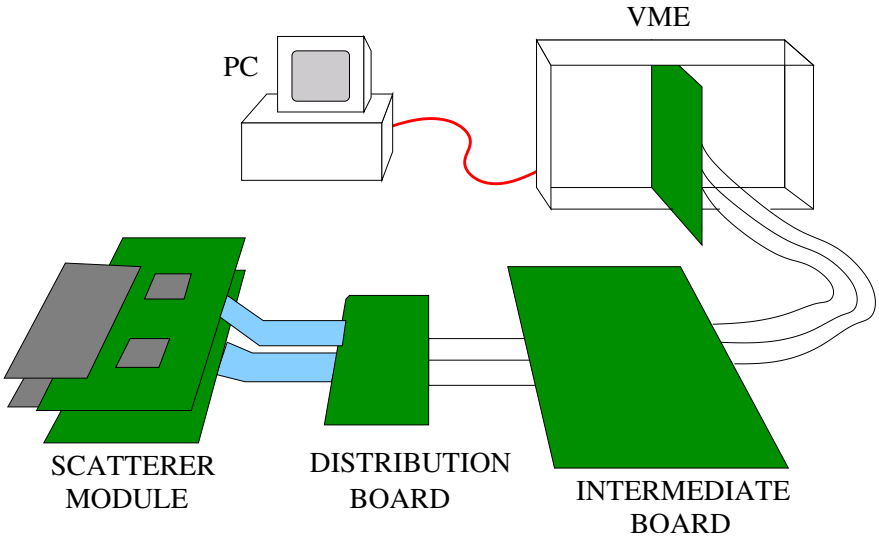

Figure 3.17: Diagram of the scatterer DAQ system.

The intermediate board (IB) represents an intermediate phase of electronic processing. Being close to the modules it supplies the analog values: biases and the threshold level for all modules. During the readout IB blocks the triggering of the scatterer by `DLT` signal generation. The multiplexed signal outputs are amplified on the IB and relayed to VME for subsequent processing. The IB also serves as a relay for logical signals passing between the chip and the VME.

The last part of the DAQ hardware is the VME board. Before the run, the VME board generates the sequence that loads the `mask` supplied by the DAQ software to the chip, with IB serving as a relay. During the readout, the VME board receives the trigger signal from the chip, generates the delay and sends the `HOLD` signal. The readout sequence determining

the readout mode is generated and sent to the chip, along with the channel shifting clock (set to 1.2 MHz). The same clock is used by the pair of flash (up to 10 MHz) ADCs which digitize both (UP & DOWN) outputs, amplified by the IB. The digitized signals are packed into an event and stored in the output buffer of the VME controller. Physically, the VME board is a PCB, inserted in a VME crate which provides the necessary power supply. The VME standard (IEEE-1014-1987) is used for communication between the PC and the VME board. The software which controls the board's function is partially executed by the FPGA of the board (readout sequence generation, event packing) but mostly reserved for the PC.

A personal computer (PC) closes the DAQ system loop. PC serves as a master control device and storage media. The DAQ software developed and used in the scope of this work collects and stores the events prepared by the VME board and allows the user to change the mask of the chips and determine the readout mode. A brief on-line analysis program is added for quality check of collected data. The complete data analysis is performed off-line on the stored data sets.

3.4.2 Data processing

The aim of processing of the scatterer data is to extract the scatterer-relevant parameters, i.e. to measure the energy and position of the Compton interaction[7]. This sub-section is devoted to the description of the software algorithm which determines those parameters. The algorithm will be illustrated on a scatterer calibration run: ^{241}Am γ-rays are detected by a single scatterer module (Figure 3.16 sensor with 256 pads, 0.5 mm thick, read by 2 VATAGP3 chips), and both interaction types (photo-absorption, Compton) are observed.

An event e corresponds to a set of raw ADC digitized values s_i^e for all readout channels, with channel number (or ID) i. To obtain the base-line or the pedestal p_i of channel i, the raw values s_i^e are histogramed. A typical histogram is shown in Figure 3.18. Since either of the $N_c = 256$ channels produces the trigger, the probability that a specific channel i contains a signal charge q is small enough[8]. Observing Figure 3.18 we can see that a majority of collected values is contained in the first peak, exhibiting a Gaussian shape. It corresponds to the sampled fluctuations of the baseline and a Gaussian fit (shown on the inset) is used to determine the mean, p_i and the variance or noise σ_i of channel i. The sampled values above the peak correspond to the detected signals, with the corresponding detected charge $q = s_i^e - p_i$. Subtracting the pedestal p_i the signal spectrum is obtained, which corresponds to the spectrum of interaction electrons.

The variance σ_i obtained from a single channel histogram over-estimates the channel noise, as a part of the base-line fluctuations is caused by power-supply variation of the chip. The

[7]The scatterer also provides a timing signal, but coincidence timing is done by the front-end electronics and no additional processing is needed.

[8]Providing that the source illuminates the whole sensor and the range of the interaction produced electrons is smaller than the pad size.

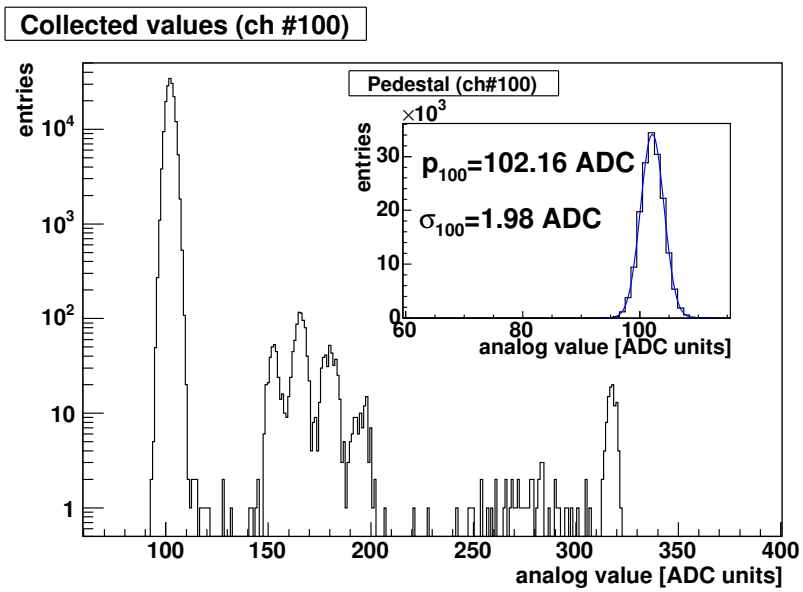

Figure 3.18: A histogram of digitized analog values of channel 100 over all collected events read out in serial mode. The spectrum contains photon interactions in addition to the first and largest peak corresponding to base-line fluctuations. The inset shows the Gaussian fit to this peak yielding the pedestal (mean) and the noise (variance).

result of such variation is a common shift of all analog values in an event, which can be effectively removed by a common mode c^e calculation:

$$c^e = \frac{1}{N_c} \sum_{i=1,\text{nothit}}^{N_c} (s_i^e - p_i), \tag{3.35}$$

where the sum runs over all output channels which are below a noise cut, i.e. not hit. The noise cut can more or less severely separate the signal from the noise, and for the used cut of $s_i^e - p_i > 3\sigma_i$ 2.7 ‰of the empty channels are exempt from common mode calculation. The common mode can be effectively calculated for serial readout mode, where all channels are available, making N_c large enough so that the error on c^e is small. In sparse mode with adjacent channel readout, the number of adjacent channels determines the precision of the calculated common mode shift. In sparse mode with no adjacent channels, the common mode shift can not be removed. Figure 3.19 shows the calculated common mode distribution for serial mode and sparse mode with 10 adjacent channels readout. The wider common mode distribution of the sparse readout mode with adjacent channels is due to the error of the common mode calculation with N_c to low. The effect on the signal will be assessed later in this section.

The calculation of the common shift improves the signal, which is now given by $q = s_i^e - p_i - c^e$. If q is small, i.e. below the noise cut, it is interpreted as the base-line fluctuation and used

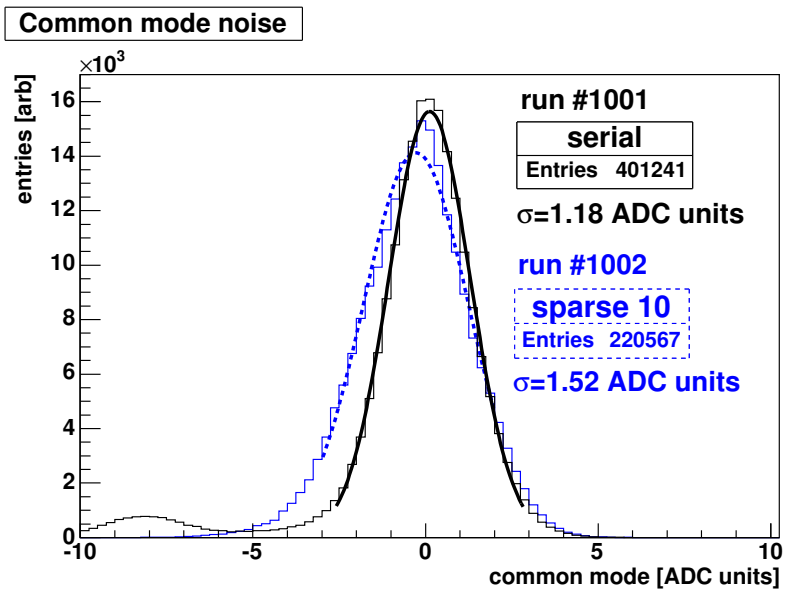

Figure 3.19: Common mode noise calculated in serial (solid line) and sparse mode with 10 adjacent channels (dashed line) readout mode. The Gaussian fit is used to determine the variance of the common mode, which is listed in the figure.

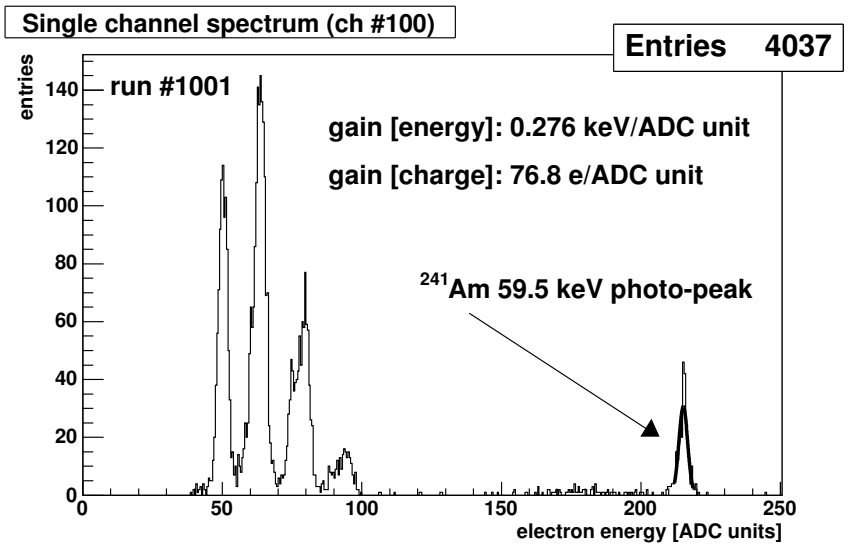

Figure 3.20: A histogram of the collected charge in a single channel. A Gaussian fit on the photo-absorption peak of the 59.5 keV photons from ^{241}Am is used to obtain the calibration values shown on the figure.

to update the pedestal and the noise with a weight $1/N_e$ (running pedestal):

$$p_{i,\text{new}} = p_{i,\text{old}} + \frac{1}{N_e}\, q, \tag{3.36}$$

$$\sigma^2_{i,\text{new}} = \sigma^2_{i,\text{old}} + \frac{1}{N_e}\left(q^2 - \sigma^2_{i,\text{old}}\right), \tag{3.37}$$

and if q is above the noise cut it is considered as signal and histogramed. For a specific channel, a single channel spectrum is obtained, and a typical spectrum is shown in Figure 3.20. The single channel spectrum is used to calibrate the processing circuit: the photo-absorption peak of ^{241}Am 59.5 keV line is fit with a Gaussian and the energy divided by the mean value is the gain in units of [keV/ADC unit]. Similarly, using equation (3.7), gain is expressed in units of [e/ADC unit].

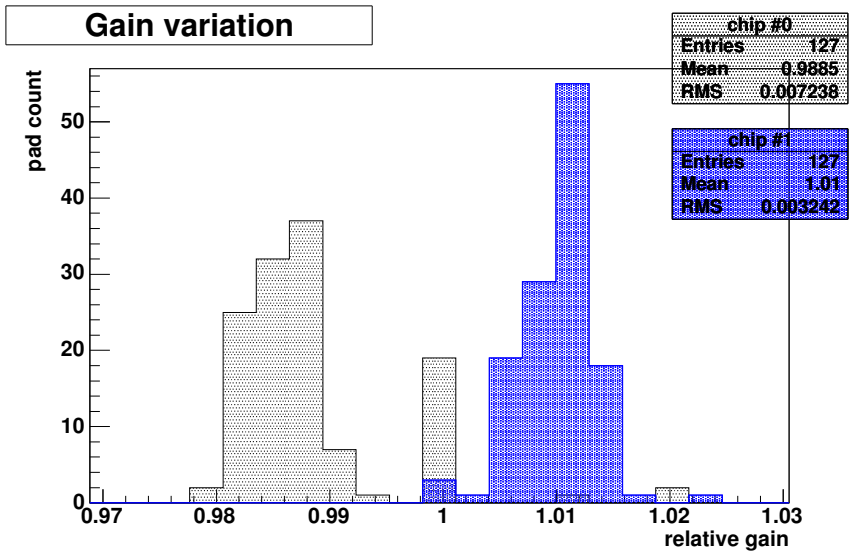

Figure 3.21: The distribution of relative gains of the readout channels in the first and the second chip. Normalization on average gain of both chips.

The variation of the gain across the sensor and ASIC is assessed by comparing gains extracted from the respective single channel spectra. The relative gains are calculated dividing the gains with the average gain of all channels in the module. The distribution of pads with respect to their relative gain is shown in Figure 3.21 and within a chip the gain varies for less than 1 %, while larger variations exist between the chips. This variation is comparable to the readout channel noise and a gain map has to be used to prevent degradation of the energy resolution. The final spectrum is obtained by reprocessing of the data using the gain map and a summation of all single channel histograms.

3.5 Calibration results of scatterer

Calibration of scatterer modules is required to determine the gain of individual readout channels and to assess the overall module performance: the resolution on the impact point, the energy and the timing resolution. The performance is compared to the requirements of the Compton camera and it is not uncommon for a prototype to fail at this stage of

development. The following subsection list the properties of the scattering modules. The exhibited average energy resolution of 1.2 - 1.4 keV FWHM combined with the spatial resolution of 1.4 mm FWHM and the timing resolution determined by the shaping time of 150 ns allows the modules to be used in a Compton camera prototype.

3.5.1 Energy resolution

The energy resolution of the scatterer is composed of two contributions. The first is the inherent resolution of the scatterer and the second the electronic noise. The inherent resolution was described among the properties of silicon sensor operation and the values for typical photon energies are listed in Table 3.1.

Table 3.2: The noise parameters of VATAGP chip

τ_s^E [μs]	A [e]	B [e/pF]	C_0 [pF]	e_a [e$\sqrt{\mu s}$/pF]
2	82.2	21.8	3.8	32
5	67.7	11.9	5.7	28

The electronic noise was derived in the description of the front-end of electronics and given by equation (3.24) with the optimal shaping time given by (3.25). The implementation of the chip in NMOS technique gives a negligible contribution of the current noise i_a and the noise is dominated by the contributions of the diode reverse current I_d and the pre-amplifier voltage noise e_a. The voltage contribution is parameterized as:

$$\sigma_v = \frac{e}{2\sqrt{2}}\, e_a C\, \frac{1}{\sqrt{\tau_s^t}} = A + B(C_d + C_r), \tag{3.38}$$

the second step assuming a fixed shaping time τ_s^t and the total capacitance C split to contributions of the pre-amplifier $C_0 = C_p + C_i$, with C_p the feedback and C_i the input capacitance, and the load capacitance $C_L = C_d + C_r$, with C_d, the detector and C_r the stray capacitance. For a VATAGP chip, the first of the VATAGP family, the parameters A and B were estimated [SCC+03] for a shaping time of 2 and 5 μs, yielding the values shown in Table 3.2, and the values of VATAGP3 are not expected to differ significantly, since the core implementation has not changed. Averaging the values in Table 3.2 we obtain e_a=30 e$\sqrt{\mu s}$/pF and C_0= 5 pF. Table 3.3 shows the optimal performance of the circuit for different C_L and different diode currents I_d.

Table 3.3: Optimum performance of a VATAGP chip for different input capacitances and diode currents.

Capacitance $(C_d + C_r)$ [pF]	I_d [pF]	τ_s^E [μs]	σ_n^E [e]	^{241}Am resolution	
				σ_n^T [e ENC]	$FWHM_E$ [keV]
0.5	100	4.6	104	112	0.95
2	100	5.9	117	124	1.05
0.5	200	3.3	123	130	1.10
2	200	4.2	140	145	1.23

The total resolution includes the contribution of the statistical fluctuation of the ionized charge (equation (3.8)) equal to 41 e for photo-electrons created by initial photon with energy of 59.5 keV, which was used for calibration. The energy resolution is derived from the ENC using equation (3.22).

Table 3.4: Emission spectrum of ^{241}Am showing γ and X-ray emission with relative intensity exceeding 0.1 %.

Energy [keV]	emission type	Relative intensity [%]
13.761	X-ray (Np $L_{\alpha,2}$)	1.07
13.946	X-ray (Np $L_{\alpha,1}$)	9.6
15.861	X-ray (Np L_h	0.153
16.109	X-ray (Np $L_{\beta,6}$)	0.184
16.816	X-ray (Np $L_{\beta,2}$)	2.5
17.061	X-ray (Np $L_{\beta,4}$)	1.5
17.505	X-ray (Np $L_{\beta,5}$)	0.65
17.751	X-ray (Np $L_{\beta,1}$)	5.7
17.992	X-ray (Np $L_{\beta,3}$)	1.37
20.784	X-ray (Np $L_{\gamma,1}$)	1.39
21.099	X-ray (Np $L_{\gamma,2}$)	0.65
21.342	X-ray (Np $L_{\gamma,3}$)	0.59
21.491	X-ray (Np $L_{\gamma,6}$)	0.29
26.3448	γ-ray	2.40
33.1964	γ-ray	0.126
59.5412	γ-ray	35.9

The energy resolution of the scatterer was measured using ^{241}Am, a γ-ray source with the principal photon energy equal to 59.5 keV. The α particles, which are also emitted by the source are absorbed in the air before they reach the sensor. The DAQ setup shown in Figure 3.17 was used. The sensor was shielded from ambient radio-frequency noise in a metal box,

which also served as a light shield. The point source was set on top of the box, 5 cm from the sensor, almost homogeneously illuminating the whole sensor. The sensor covered 1 % of the solid angle and the attenuation coefficient of silicon (Figure 2.11) is 3 % at 59.5 keV. A single module efficiency is therefore $3{\times}10^{-4}$. Sources with activity up to 150 MBq were used, giving expected event rates of 50 kHz in a single module. The actual event readout rate was saturated at approximately 5 kHz in the sparse readout mode and 500 Hz in the serial readout mode.

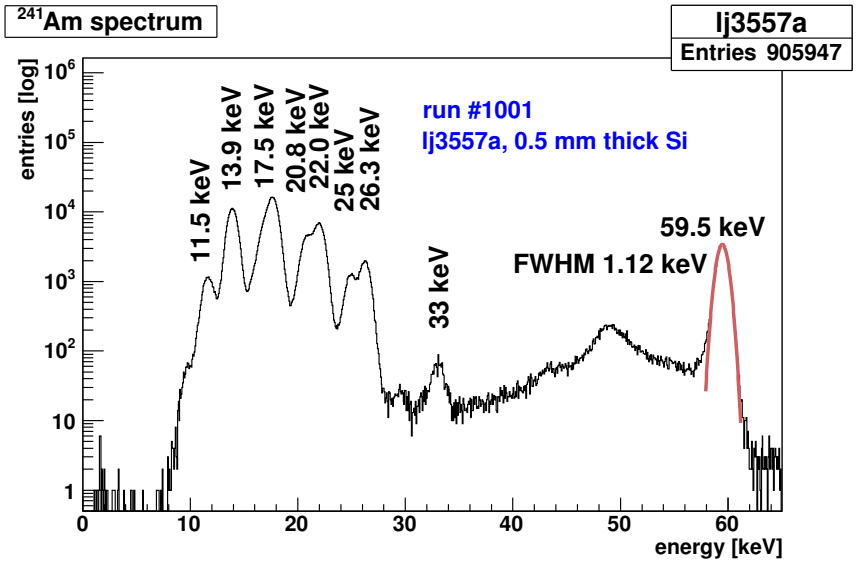

Figure 3.22: ^{241}Am spectrum recorded in a scatterer module. The selected module `lj3557a` was mounted with a 0.5 mm thick sensor. The most important run parameters are the following: shaping time of the slow shaper 4 μs, reverse bias 120 V was equal to V_{FD}, threshold at 8 keV. The resolution is obtained with a Gaussian fit to the photo-peak. Note the logarithmic scale.

Figure 3.22 shows the ^{241}Am spectrum obtained with scatterer module `lj3557a` utilizing a 0.5 mm thick sensor. In addition to the principal line at 59.5 keV the remaining lines take a part in the ^{241}Am spectrum and are listed in Table 3.4, save for the 22.0 and 25.2 keV lines which correspond to the characteristic X-rays of silver (Ag), present in the conductive glue at the sensor's back side. The energy resolution of 1.12 keV is determined by a Gaussian fit to the photo-peak.

The resolution of the combined spectrum is in agreement with the values shown in Table 3.3, for I_d varying between 100 and 200 pA per pad and the total load capacitance below 2 pF. A more precise estimate is hard to obtain since the spectrum is a combination of pads with different noise. The noise of a pad is affected by the length and capacitive coupling of the routing lines in the top metal layer and the quality of the sensor material which may vary throughout the wafer. This variation is illustrated in Figure 3.23, where a distribution

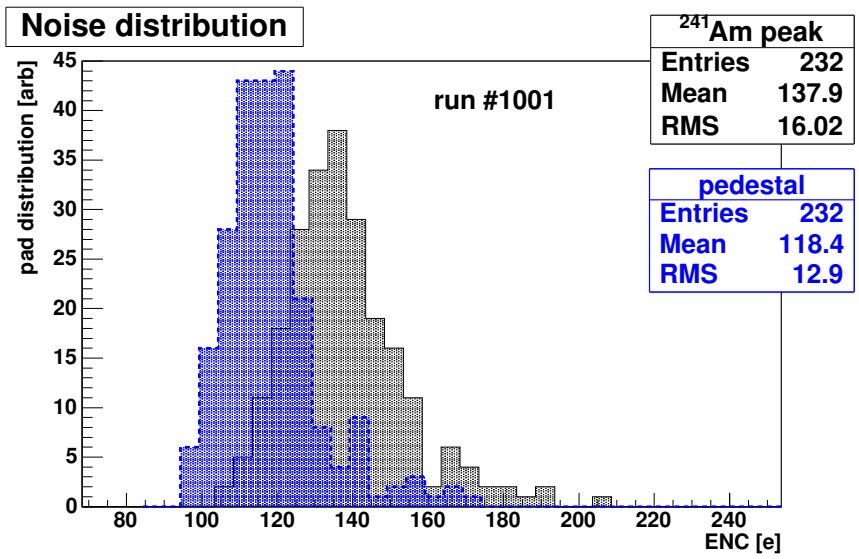

Figure 3.23: The distribution of pads with respect to their pedestal (dashed line) and signal (solid line) noise. A subset of 232 operating channels out of 256 available is drawn.

of pads with respect to their pedestal and signal noise is shown. The pedestal noise is the base-line fluctuation and the signal noise is the resolution of the 59.5 keV photo-peak, obtained from the fit to the single channel spectrum. The root-mean-square (RMS) of the pedestal noise is 12 e over the sensor, and 16 e for the signal noise. One can conclude that the estimation of the signal noise in Table 3.3 agrees with the measured noise within the interval set by the RMS of the pad distribution.

The common mode variation is comparable with the noise of each of the channels and the common-mode subtraction substantially improves the energy resolution of the scatterer. The improvement is illustrated in Figure 3.24, where the resolutions of the aligned ^{241}Am photo-peak are compared for various readout-modes. In pure sparse mode no common-mode subtraction is possible and the width of the peak includes the common-mode variation. The common-mode is estimated well by including 10 adjacent channels, with the energy resolution approximately equal to the energy resolution obtained for a full set of channel values, available in the serial read-out mode. Reading 10 instead of the 256 channels allows for 25-times higher rate of event readout, providing a way for fast image generation.

The performance of the module `lj3557b`, equipped with a 1 mm thick sensor, was also tested with ^{241}Am source. The resulting spectrum is shown in Figure 3.25. The resolution of 1 mm thick sensors was in general worse than of their 0.5 mm counterparts. A large current flowing through the guard ring was observed which might deteriorate the module performance. The average resolution was 1.4 keV FWHM, obtained by a Gaussian fit to the ^{241}Am photo-absorption peak.

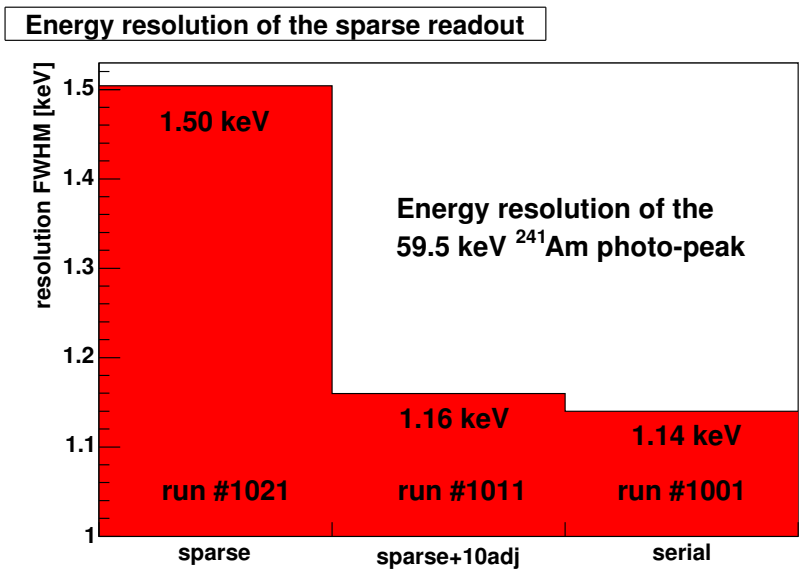

Figure 3.24: The resolution of the photo-peak obtained in different readout-modes.

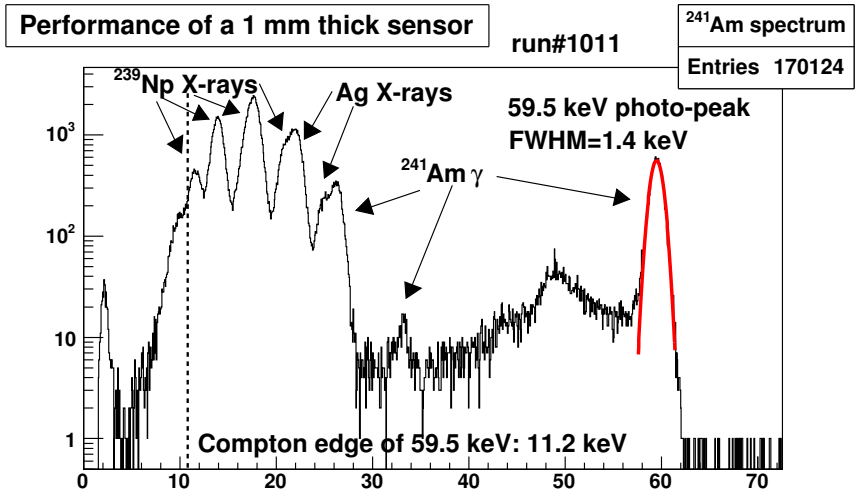

Figure 3.25: The ^{241}Am spectrum recorded on `1j3557b` hybrid with a 1 mm thick sensor. The recorded γ and X-ray lines conform to the emission lines given in Table 3.4. The threshold was set just above the Compton edge.

Tests were also performed using ^{99m}Tc source, a candidate for imaging with the Compton camera. The photons with initial energy of 140.5 keV are either photo-absorbed (a peak at interaction electron energy equal to 140.5 keV) or Compton scattered (the continuum below the Compton edge at 49.8 keV) in the sensor. The additional lines are the X-rays of lead,

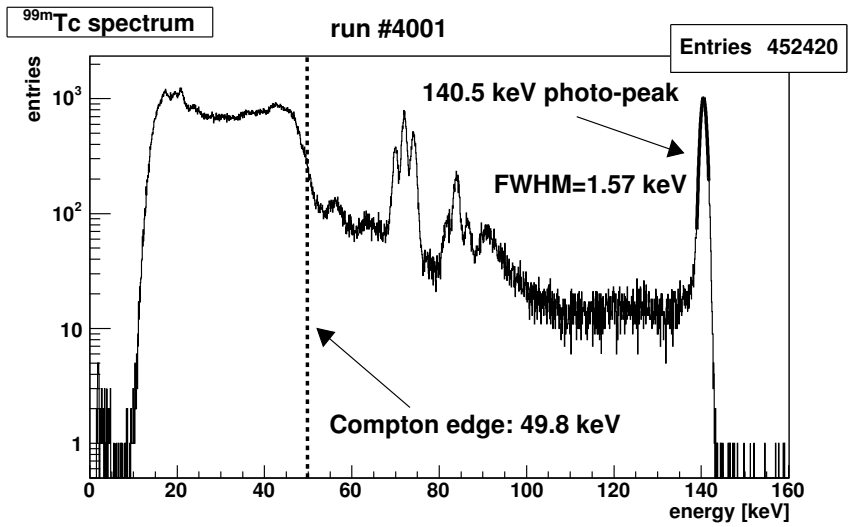

Figure 3.26: ^{99m}Tc spectrum recorded with `lj3557a` hybrid and a 0.5 mm thick sensor. The spectrum consists of a clear 140.5 keV photo-absorption line of ^{99m}Tc, the Compton continuum of the same photons and X-ray lines of lead. Lead was used for shielding. The spectrum was not taken with an optimized chip and the resolution of 1.6 keV could be improved.

which was used for shielding. The recorded resolution of 1.6 keV is slightly worse than for ^{241}Am, which is partly due to the module being part of a larger setup and additional issues discussed in Chapter 5 were involved.

To conclude, the scatterer module parameters conform to the expected values. A resolution of 1.12 keV was obtained on a hybrid with a 0.5 mm thick sensor for ^{241}Am photons with energy equal to 59.5 keV. The performance deteriorates for thicker modules, with resolution of 1.4 keV observed on a 1 mm thick sensor. The measurements were repeated for 140.5 keV photons from ^{99m}Tc and and a resolution of 1.6 keV was exhibited, which is a slight deterioration compared to the performance for ^{241}Am source. The decrease of resolution was due to the insertion of several modules in the coincident setup and issues discussed later in this thesis.

3.5.2 Spatial resolution

The position of the interaction equals to the center of the electron-hole cloud generated by the interaction electron. Spatial resolution is greatly improved if the signal is shared among the pads. But the gain in spatial resolution is over-ruled by a decrease in the energy resolution, with the error growing approximately as $\sqrt{n}$ with n number of pads which collect the signal charge. Therefore it is convenient for a Compton camera to make pads larger than the expected range of interaction electrons. Comparing the pad size of 1.4 mm to ranges of

interaction electron shown in Figure 3.2 almost no charge sharing is expected and the spatial resolution is determined by the pad size.

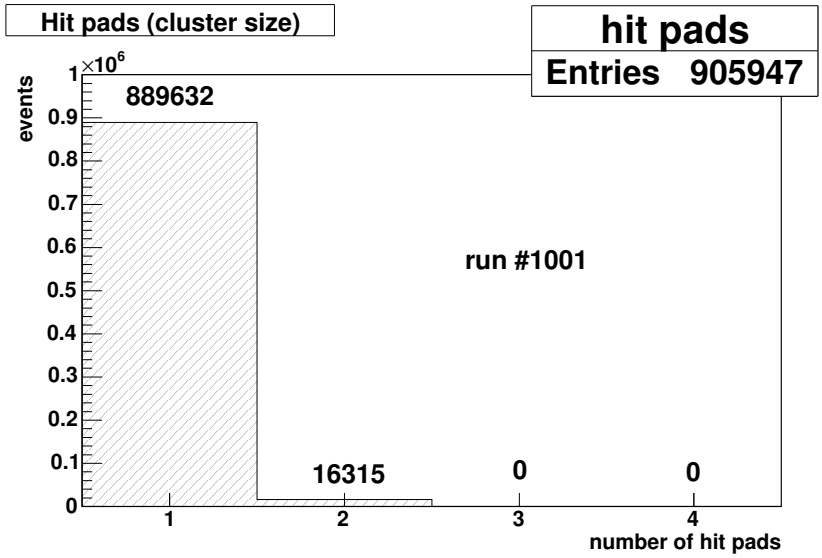

Figure 3.27: Distribution of events with respect to the number of adjacent pads containing the signal; the pad is considered hit if it contains more than 3% of the signal.

Figure 3.27 shows the distribution of events over the number of pads collecting the signal of photons from ^{241}Am source in a 0.5 mm thick sensor. Only 1.7 % of the events have signal spread over more than one pad and their contribution to the spatial resolution is negligible. The Figure confirms the expectations and the spatial resolution of the scatterer equals to 1.4 mm FWHM.

3.5.3 Trigger properties

The properties of the trigger are determined by the ASIC and cannot be improved by subsequent processing. There are two properties that need to be evaluated: the timing resolution, composed of time-walk and jitter and the minimum detectable charge.

Timing resolution. Timing resolution of the trigger was measured in the TEST mode of the chip, illustrated in Figure 3.15. The injected charge equals $Q_i = \Delta V/C_t$,with ΔV the voltage step and C_t the test capacitance. The timing of the chip can be tested because the time of charge injection is known. The relevant quantity is the delay t_r between the moment of charge injection and the edge of the digital trigger pulse and the timing resolution is determined as the variation of t_r.

Figure 3.28 shows the results of the measurement of t_r. A fixed $Q_i = 2.7$ pF = 17000 e was selected and the threshold voltage v_{thr} varied. Each histogram in the main frame corresponds

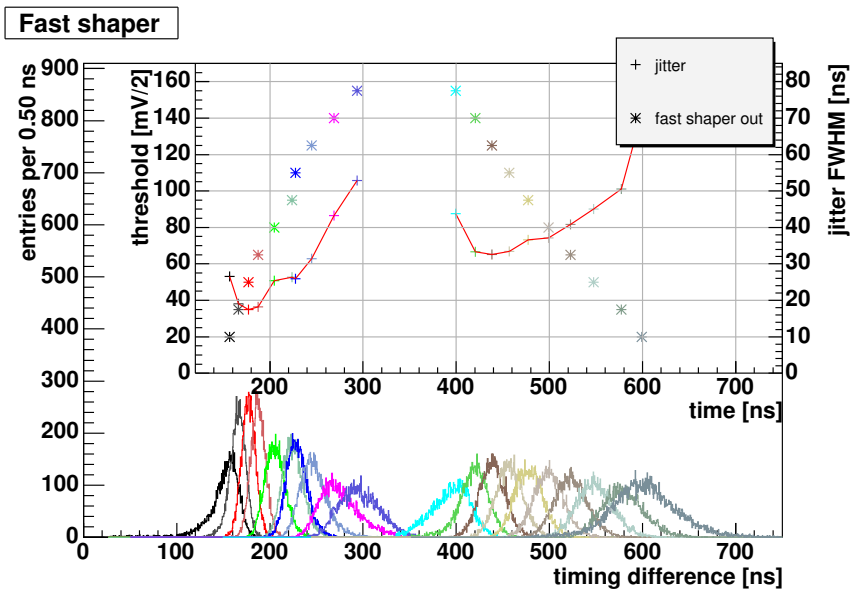

Figure 3.28: Measurement of the VATAGP3 timing resolution for a fixed charge injection of 2.7 fC and a variable threshold. The histograms in the main frame show the distribution of the trigger time for a fixed threshold. The dependence of the distributions' means of the selected thresholds is shown on the inset, effectively tracing the shape of the trigger pulse appearing at the discriminator input. The widths of the distributions are plotted versus the distribution means.

to the distribution of t_r for a fixed v_{thr}. The inset shows the mean of the histograms as a function of v_{thr}, effectively tracing the shape of the analog pulse $v_{\text{out}}(t)$ which appears at the input of the discriminator. The shaping time of the pulse can be estimated to equal to 150 ns.

The time-walk is the variation of the trigger time due to the variation of the signal amplitude for a fixed threshold. The same effect is observed if the threshold is varied and the pulse amplitude is fixed, as was the case in our experiment. The measured time-walk is the interval covered by the mean values of the t_r distributions. Only the triggers on the rising edge of the signals are considered and the measured interval is spanned between 150 and 300 ns. This gives a time-walk of 150 ns which is approximately equal to the shaping time in agreement with the prognosis given in the trigger description.

The jitter is the variation of the trigger time for at fixed pulse amplitude, or conversely, at fixed threshold. The measured jitter is hence the width of each of the histograms shown in Figure 3.28. The FWHM of the distributions is plotted on the inset as a function of the respective histogram mean. The FWHM of the jitter is related to the slope of the input signal for given threshold and extends between 17 and 50 ns for the rising part of the signal. The best performance with FWHM=17 ns is obtained where the slope is the steepest, i.e

at low thresholds. The jitter in that range is given by equation (3.34) and depends on the noise of input signal of the discriminator. The noise is evaluated using equation (3.26), the parameters of the chip obtained from Table 3.2. For the load capacitance between 0.5 and 2 pF, the noise is between 400 and 500 e and the corresponding jitter between 8 and 10 ns FWHM. The disagreement between the estimate and the measurement is due to increased noise of the chip in TEST mode and the variance of the voltage step amplitude ΔV.

Minimal detectable charge. The rate of threshold crossings by the oscillating base-line as a function of threshold voltage is given by equation (3.27). From equation (3.26) and the chip parameters given in Table 3.2 the ENC of the fast shaper is estimated between 400 and 500 e. For a noise rate of 1 Hz and the shaping time of 150 ns the equation (3.29) yields $\alpha_r = 5$ and inserting α_r into equation (3.30), the minimal detectable charge Q_{min} is between 1800 and 2200 e, which sets the minimal detectable energy of the interaction electron between 6 and 8 keV.

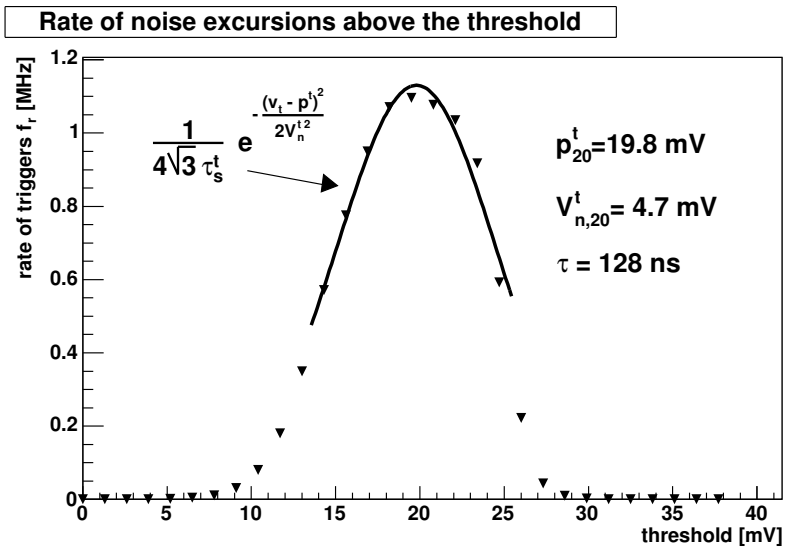

Figure 3.29: The rate of threshold crossings by the oscillating base-line as a function of the threshold voltage for channel #20 in `lj3557a` module.

The rate of noise triggers was measured by masking all channels except the measured one in the `trigger mask` and stepping through a set of threshold values. A typical graph of measured rates is shown in Figure 3.29. The model equation (3.27), is corrected for the shift of the base-line of the analog trigger signal, the trigger pedestal p_t^i:

$$f_r = \frac{1}{4\sqrt{3}} \tau_s^t \mathrm{e}^{-((v_{thr}-p_t^i)^2/2V_n^{t\,2})}. \tag{3.39}$$

ENC σ_n^t is determined from the voltage noise V_n^t with a trigger gain calibration. Photons from a mono-chromatic γ-ray source, e.g. ^{241}Am, are used and the maximal signals are caused

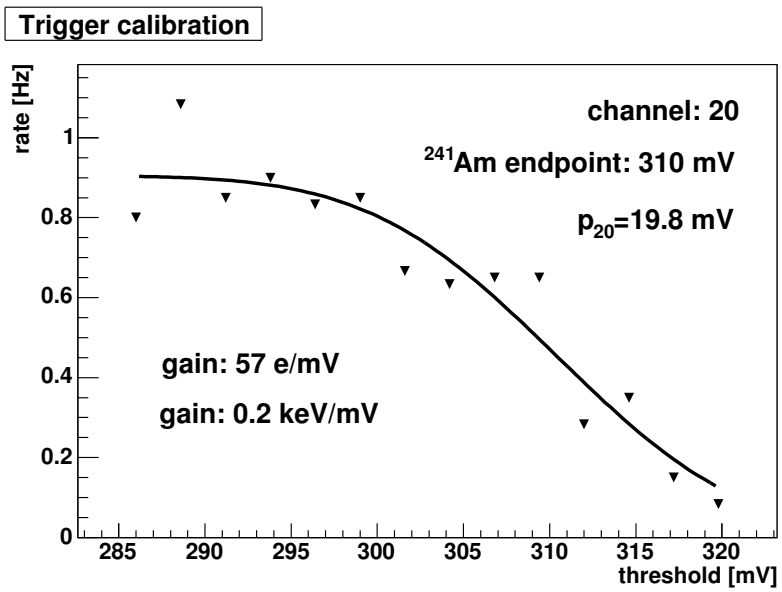

Figure 3.30: Analog trigger pulse calibration using ^{241}Am source: the rate of the triggers as a function of the increasing threshold voltage.

by photo-electrons with energy equal to the energy of the photons. When the threshold is between the Compton edge and the photo-peak, the trigger rate is practically independent of the threshold setting and drops abruptly when the threshold exceeds the photo-peak. The slope of the drop is determined by the noise of the analog trigger signal and a characteristic S-curve is measured. A typical S-curve is shown in Figure 3.30 along with the fit with the complementary error-function. The threshold where half of the maximum rate is measured equals to the average signal height caused by photo-electrons. The gain is calculated and expressed in e/mV (and keV/mV) and used to convert the measured V_n^t to ENC, e.g for channel #20 shown in Figures 3.29 and 3.30, $\sigma_{n,20}^t$= 268 e.

The distribution of the pads with respect to their ENC is shown in Figure 3.31. Approximately 70 % of the channels have noise below 300 e and the determined minimal detectable energy in those channels is less than 5 keV for a rate of random triggers equal to 1 Hz.

When an array of channel triggers is combined into a chip trigger, two issues need to be addressed. The first is a positive feed-back of the chip trigger, and the second the spread of trigger pedestals.

In any given circuit there are always parasitic couplings. One of such couplings is generated between the digital trigger pulse and the analog input to the discriminator. The positive feed-back causes the chip to oscillate when a critical noise rate f_c is exceeded. To avoid oscillations, the threshold has to be set high enough and the minimal threshold is determined by the strength of the feed-back. A stable operation was achieved for thresholds above 8 keV as illustrated in Figure 3.22.

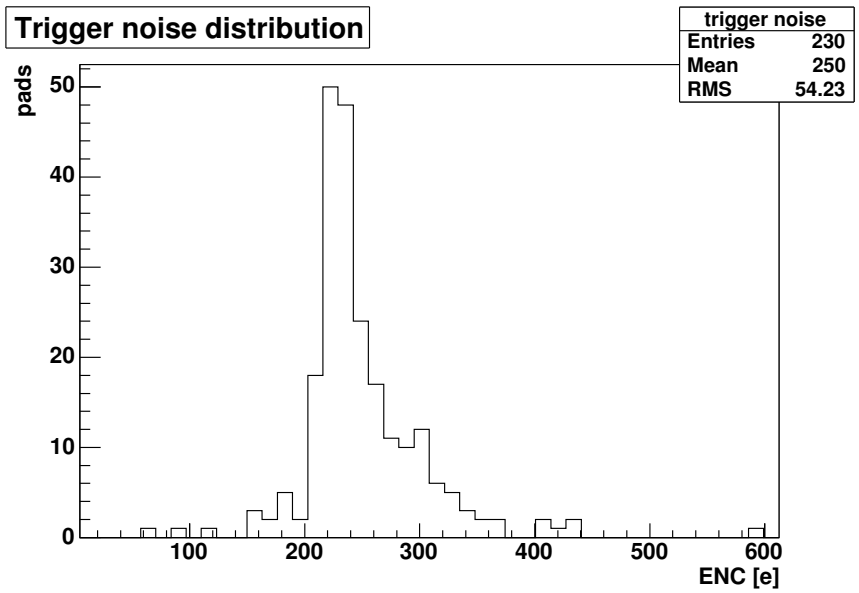

Figure 3.31: Distribution of the pads with respect to the noise of the trigger analog signal. The noise is obtained from a fit to the rate of the excursions of the noise above the threshold, and the gain is determined from calibration of the signal with ^{241}Am source.

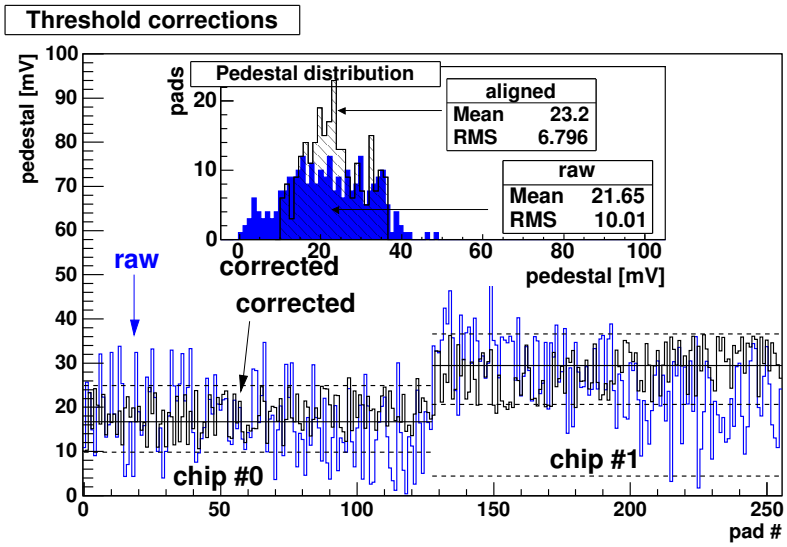

Figure 3.32: Comparison of pedestals obtained with and without DAC corrections. On the inset the distributions of the channels with respect to the pedestal value are shown.

The minimal detectable energy is determined by the relative threshold $v_{thr} - p_{t,i}$ of a readout channel i and depends on $p_{t,i}$, since the threshold v_{thr} is constant across the chip. The critical noise rate f_c will be therefore exceeded first in the channels with highest $p_{t,i}$. To lower the

relative threshold $v_{thr} - p_{t,i}$ in the rest of the channels, individual channel corrections to the common threshold line are used. The corrections are applied through the `DAC mask` which vary the relative threshold of the channel as

$$v_{t,i} - p_{t,i} = (v_{thr} + m_i * \delta_V) - p_{t,i} = v_{thr} - (p_{t,i} - m_i * \delta_V), \tag{3.40}$$

with δ_V a voltage step determined by `mbias` and m_i the channel-specific correction. The last expression of equation (3.40) shows that the correction of the threshold can be interpreted as a correction to the pedestal. m_i are 3-bit numbers coded in the `DAC mask`, varying between -3 and +3. Figure 3.32 shows pedestals obtained with and without applying corrections. The chip allows for correction of pedestals within the chip and the module performance is determined by the inter-chip variation of the threshold[9]. The inset shows the distribution of channels with respect to their pedestal values, and the root-mean-square (or the variance) of the distribution is decreased from 10 to 7 mV. The operating threshold for the spectra shown (Figures 3.22 and 3.25) was set at 60 mV, which gives an average minimal energy of 6 keV in chip #1 and 8.6 keV in chip #0, using the average gain of the module of 0.2 keV/mV.

3.6 Conclusion

The scatterer module for a Compton camera is based on a silicon pad sensor coupled to off-the-shelf application specific integrated circuit (ASIC) named VATAGP3 at the sensor's output. The performance parameters are the energy resolution of the interaction electron, the spatial resolution of the interaction position and the timing resolution of the trigger signal.

The energy resolution of the silicon sensor is dominated by electronic noise and optimal performance is achieved when the signal charge is collected in a single readout channel. This compromises the spatial resolution, which is given by the pad dimension and equals to 1.4 mm FWHM. The readout channel of VATAGP3 is composed of a charge-sensitive amplifier, a CR-RC shaper and an externally driven SAMPLE & HOLD circuit. The shaping time is optimized for minimum noise to 4 μs, and the achieved energy resolution equals 1.12 keV FWHM in 0.5 mm thick and 1.4 keV FWHM in 1 mm thick sensors.

The minimal detectable energy is determined by the strength of the positive feed-back between the circuit generating the digital trigger and the analog trigger pulse. A further improvement is achieved with alignment of base-lines of the analog trigger signals. Operating thresholds down to 8 keV were achieved.

The trigger signal is generated from the sensor signal using a charge-sensitive amplifier and a CR-RC shaping circuit producing an analog trigger pulse, which is then discriminated by a level discriminator. The shaping time of the trigger shaper should exceed the time necessary

[9] Application of chip dependent thresholds is foreseen.

to collect the charge. The time varies with the interaction depth in the sensor and, for voltages below $2V_{FD}$ foreseen for the module operation, equals up to 70 ns. The shaping time of the trigger is set to 150 ns. There are two contributions to the timing resolution of the trigger: the time-walk which equals to the shaping time and the jitter, which equals to a fraction of the shaping-time, the fraction determined by the ratio of the signal and the noise of the analog trigger pulse. Because the minimal detectable signal must exceed the trigger noise by a factor, the timing resolution is dominated by the time walk.

Chapter 4

Absorber

The absorber is the second detector in a Compton camera and detects the scattered photons by photo-absorption. The requirements for a Compton camera absorber are approximately identical to the requirements of the Anger camera detector and it is not uncommon for Compton camera prototypes to use sensors developed for an Anger camera. The signals produced by the absorber should provide the scattered photon absorption position and a trigger signal to correlate the absorber with the scatterer. The energy resolution of the absorber is of secondary importance and is only used for offline rejection of background.

Our absorber was a part of the second generation Single Photon RINg Tomograph (SPRINT) [RCS+88], which was initially used as an Anger camera for SPECT imaging. The ring had already been used as a part of the Compton camera prototype [LCH+98] and showed excellent imaging qualities. The sensor material is Tl doped NaI coupled to a set of photo-multiplier tubes (PMT), and the performance of the scintillator-PMT combination shows several qualities, including large sensitive area of NaI crystals, good spatial resolution of the order of few mm, low cost, simplicity of use and high light output and related energy resolution. The only draw-back of the sensor is the relatively low stopping power of NaI (cf. Figure 2.12) for energies of photons above approximately 200 keV. The alternatives are rare (CsI,BGO) and have their own draw-backs.

This chapter will describe the properties of the SPRINT module which was used as the absorber for the Compton camera prototype, the mechanical layout and the absorber related part of the data acquisition system. The modules were calibrated using point-like radio-active sources. Based on data from calibration run, the energy and impact position are determined, and performance, i.e. the spatial and energy resolution, is evaluated on the same set of data. A modified setup used for determination of the timing properties is described and the timing resolution evaluated.

4.1 SPRINT module

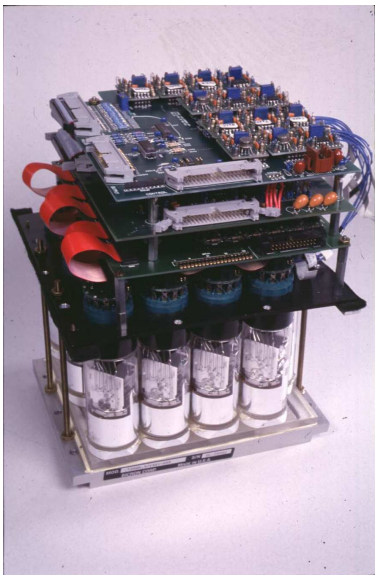

Figure 4.1: Photography of a single SPRINT module.

SPRINT was a ring tomograph, composed of 11 identical modules. The absorber of our prototype consists of a subset of these modules. Figure 4.1 shows a photography of one of the modules. Starting from the bottom of the module, it is composed of the sensitive part, NaI(Tl) crystal, photo-multiplier tubes (PMTs) and associated electronics.

The sensitive material used, sodium iodide (NaI) is a scintillation material, and as such converts the energy of high-energy photons and other fast particles into quanta of visible light. The mechanism for photon detection is the following: first an interaction electron is produced by the photon interaction, and the interaction electron further ionizes the atoms of the medium. Since the medium has an energy gap around the Fermi energy, the ionization produces pairs of electron and holes moving around the crystal. The pairs recombine to light quanta on activation centers in the crystal, with the energy of the produced photons smaller than the energy of the band-gap and the number of produced photons proportional to the energy of interaction electron. The crystal is transparent for the produced light, and the light is collected at the crystal boundaries by an appropriate light sensor. Table 4.1 lists some properties of the NaI(Tl) used as a scintillator sensor.

Mechanically, the crystal is set in a metal gantry which protects it from ambient influences. The crystal is made of 44 bars, each bar 15 cm long, 3 mm wide and 1.27 cm thick[1].

[1]In the ring the bars were set along the ring circumference and enabled light sharing among the modules. The light spread along the ring axis was significantly limited with the stripping of the crystal.

Table 4.1: Properties of NaI(Tl) scintillator crystal.

Density [g/cm^3]	Maximum wavelength [nm]	Refractive index	Decay time [μs]	Energy per photon [eV]
3.67	415	1.85	0.23	26

The crystal is coupled to 20 Hamamatsu R980 circular photo-multiplier tubes (PMTs) with 38 mm diameter, arranged in a densely-packed hexagonal array. The bialkali photo-cathodes of each tube convert photons of visual light produced by interaction in the scintillator to photo-electrons with average quantum efficiency of 20-30 %. The number of photo-electrons is then multiplied on 10 subsequent dynodes with a gain factor of approximately 1×10^6 for voltage difference between the cathode and the last anode set to 1 kV. Gains of individual PMTs in the assembly can vary up to 50 %.

The contribution σ_S of statistical fluctuation to the energy resolution of the module is determined by the stage with minimal number of signal carriers, which is the first dynode stage. Assuming Poisson statistics, the error is proportional to the square root of the number of generated photo-electrons on the photo-cathode which is in turn proportional to the square root of energy:

$$\sigma_S = K\sqrt{E_e}, \tag{4.1}$$

where E_e is the energy of the interaction electron and K the proportionality constant. K in our setup, exceeds 0.5 $\sqrt{keV}$.

The top three layers of the module provide electronics support. The function is divided as follows: the lower layer contains the voltage divider for the PMTs, the middle layer hosts 20 identical readout channels and at the top there is a summation board, providing partial sums and the total sum of 20 amplified signals. The readout channel of the SPRINT module consists of a charge-sensitive preamplifier which integrates the charge and a shaper which limits the bandwidth of the signal pulse for a decent signal-to-noise ratio. The shaping time is set to 1 μs and exceeds the charge collection time of 230 ns for NaI(Tl) (Table 4.1). The electronic noise is small compared to the statistical contribution to the energy resolution and the noise performance of the readout electronics is of secondary importance.

4.2 Data acquisition system

The data acquisition system (DAQ) for the SPRINT module is sketched in Figure 4.2. The maximums of all 20 PMT signals are digitized using a peak sensing ADC[2], during an externally supplied gate. The gate is generated by the energy sum signal, which is a

[2]VME based, model # V785, produced by CAEN.

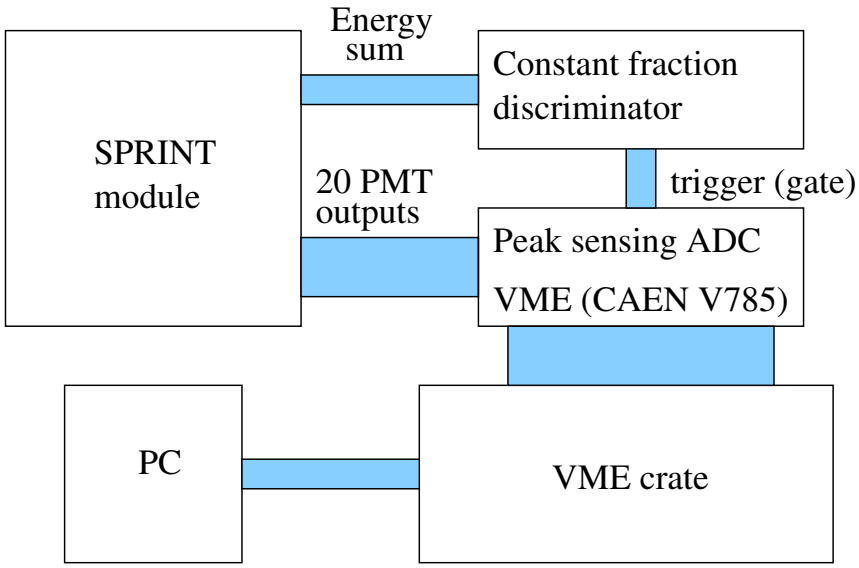

Figure 4.2: A block schematic of the data acquisition system for the SPRINT module calibration.

signal provided by module electronics, and corresponds to a sum of shaped outputs of all 20 PMTs. The sum is fed into a constant fraction discriminator (CFD) and the resulting trigger starts the gate. The digitized values are organized in an event and supplied to the PC for subsequent data processing.

All modules were calibrated individually and the setup described above was used. In a multi-module setup each module was hooked to a separate peak sensing ADC with an individual gate. The events are collected individually for each module and combined at the PC level.

4.3 Module calibration

Prior to their use in the Compton camera setup, SPRINT modules were calibrated in order to determine and improve their energy and position resolution. The tests were performed with a custom calibration setup.

The principal reason for the calibration run is the variation of both crystal properties and PMT characteristics for different interaction positions. The variations were determined by a scan with a point-like radio-active source across the crystal surface of each module. Since the features of the crystal (e.g. the bar width) have dimensions on a mm scale, the source was collimated to a 1 mm wide beam and placed immediately below the crystal surface. The following will illustrate the calibration procedure on a 5 mm $\times$ 5 mm mesh with a ^{57}Co source, with principal γ-ray energy of 122 keV and a second strong emission line at 136 keV

with 12 % intensity of the principal line. A constant number of events ($N_e = 30000$) was taken at each position and the data were stored for off-line analysis.

The energy of the scattered photon E_s is calculated as the sum of the collected light L_i on each (i) of the total number $N_{PM} = 20$ of the PMTs:

$$E_s = \sum_{i=1}^{N_{PM}} L_i, \tag{4.2}$$

assuming equal gain of the PMTs. If the relative gains are given as g_i, the gain corrected energy is calculated as:

$$E_s = \sum_{i=1}^{N_{PM}} g_i L_i, \tag{4.3}$$

The interaction position $\vec{\mathbf{S}}$ was initially calculated as a centroid of the collected light on the PMTs, combined with a known PMT positions $\vec{\mathbf{r_i}}$:

$$\vec{\mathbf{S}} = \frac{1}{E_s} \sum_{i=1}^{N_{PM}} g_i L_i \vec{\mathbf{r_i}}, \tag{4.4}$$

Later on the method was compared to more sophisticated position reconstruction methods, such as maximum likelihood estimation. The methods showed comparable results over the majority of the sensor surface, and the centroid method was kept because of its relative simplicity. The centroid method, however, suffers from the imaging distortion due to the relatively small number of PMTs. The distortion is readily corrected with a mapping of reconstructed positions back on the true positions using a map generated by a calibration run.

For a successful use of equations (4.3-4.4) the determination of relative gains g_i of PMTs is necessary. With determined gain the energy and spatial resolution of the module can be inspected. This will be the issues covered in the following subsections.

4.3.1 Determination of PMT gain

The first step in processing of the calibration data is the determination of gain g_i of the individual PMTs, required for energy and position determination. The gain of the PMT is the response of PMT to photons with known energy divided by the energy of the photons. The simplest method of gain determination is observing the response of the PMTs to source placed directly under their centers. To avoid errors from mismatch of source and PMT placement, the gain was determined from the data collected on the calibration mesh.

In each point, the average light collected in each of the PMTs was determined, as illustrated in Figure 4.3. The inset shows a two dimensional histogram with entries separated according

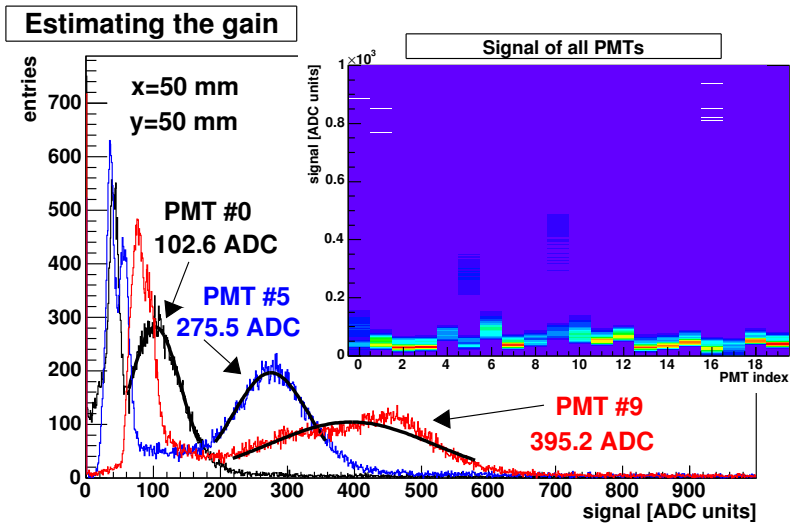

Figure 4.3: Data from a single calibration point. Inset: the two dimensional histogram with entries separated based on the PMT index and the collected light in ADC units. On top of the pedestals, PMT #0, #5 and #9 collected data from the source. Main frame: histograms of single PMTs with respect to the collected light, with average determined by a Gaussian fit to the signal peak. The average responses for respective channels shown in the figure.

to the PMT index and the digitized energy. In this case, photo-absorption was detected by PMTs #0, #5 and #9 which have entries exceeding their base-line value. The data of those PMTs is shown in the large frame, and the average amount of collected light by a PMT is estimated using a Gaussian fit.

The distribution of light around the interaction point is approximately Gaussian, since it was created by the interaction electron along its windy path. This is reflected in the Gaussian shape of the average amount of collected light of each PMT as a function of the source position, as illustrated in Figure 4.4a. A two-dimensional Gaussian fit to this function determines the centers of the PMTs and the hypothetical response of the PMT to the source placed at the PMT center. Dividing the response by the photon energy the gain of the PMT is obtained.

Figure 4.4b shows the variation of gain among the PMTs. The parts of Gaussian distribution corresponding to each PMT are combined in a single graph and the response is color-codded. The variation of the response at the PMT center determines the variation of the gain, and variations of up to 50 % are observed among the PMTs. Since all PMTs are connected to the same resistive divider chain, the variation of the gain has to be corrected off-line by a gain map, which is used in subsequent processing.

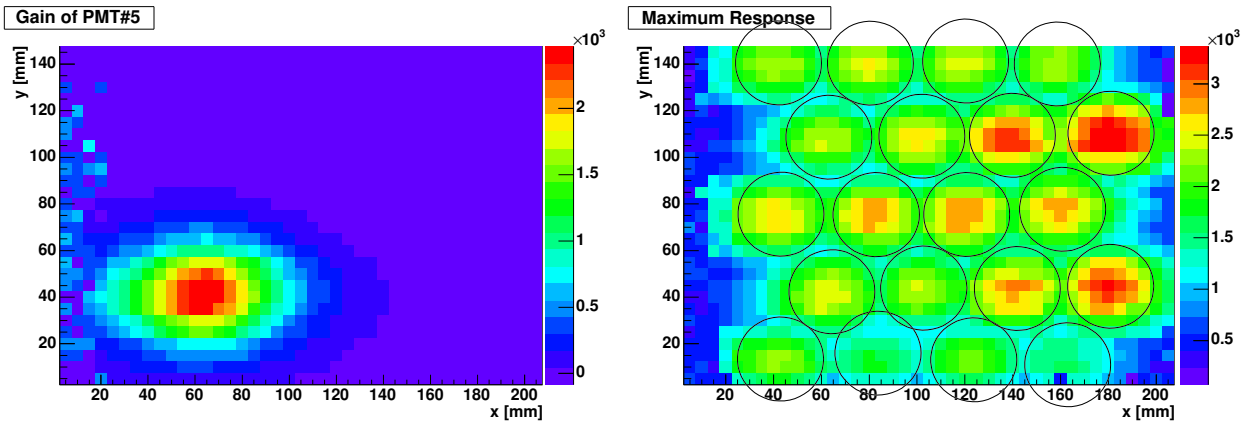

(a) (b)

Figure 4.4: (a): The average collected light in a single PMT (#5 shown) as a function of the source position. (b): The maximum collected light by a PMT as a function of the source position. Near the position of the PMT, that PMT dominates and the gains can be compared. The determined positions of PMTs are drawn as black circles.

4.3.2 Determination of impact position

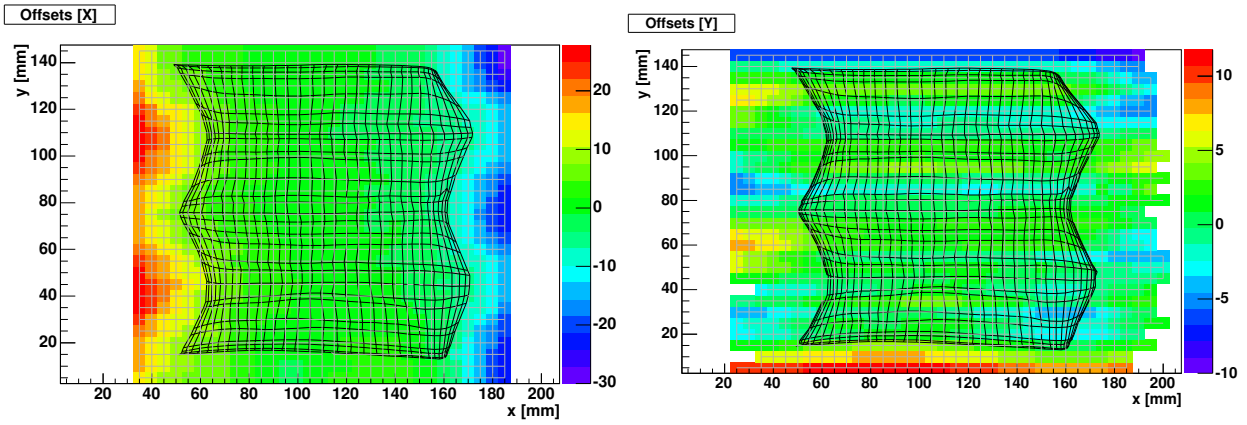

(a) (b)

Figure 4.5: The distortion of the reconstructed points. The original points are on the intersections of the gray grid, the points reconstructed with the centroid method on the intersections of the black grid. In (a) the offset in x direction is color-coded and the same method is used to show offsets in y direction in (b).

The calculation of g_i allows for determination of the interaction position based on equation (4.4). Figure 4.5 shows the original source placement grid (gray) and the distorted reconstructed grid, part (a) showing the shift of the reconstructed position $\vec{\mathbf{S}}$ from the true position $\vec{\mathbf{S_0}}$ in x (along the bars) and (b) the shift in y (perpendicular to the scintillator

bars). The histograms represent correction functions $\Delta x(x, y)$ and $\Delta y(x, y)$, defined at the true position (x, y) of the source, and the measured position of the source is given by:

$$x' = x + \Delta x(x, y) \text{ and } y' = y + \Delta y(x, y). \tag{4.5}$$

The distortion is corrected for with a distortion map $\Delta' x(x', y')$, $Delta' y(x', y')$, which is the inverse of functions given in equation (4.5). Then the position of the impact is determined as:

$$x = x' + \Delta' x(x', y') \text{ and } y = y' + \Delta' y(x', y'). \tag{4.6}$$

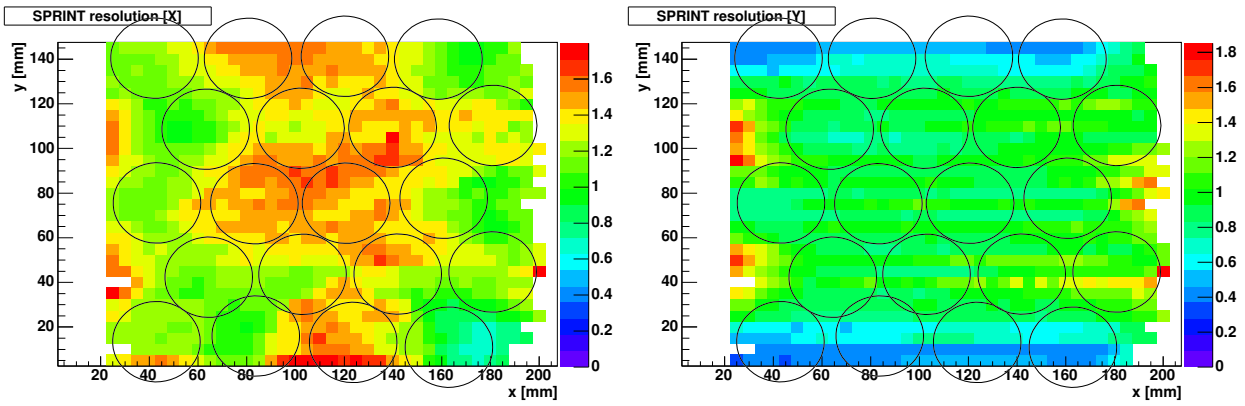

(a) (b)

Figure 4.6: The resolution of the calibration points obtained as the spatial resolution (mm variance) of the reconstructed source position. Figure (a) shows the resolution in x and Figure (b) the resolution in y.

The obtained resolution of the impact point is shown in Figure 4.6. The interaction point is reconstructed with a resolution below 1.5 mm (variance) or 4 mm FWHM for most of the module area. The resolution in y is slightly better since the steps in the detected light when the source is shifted from one bar to another are large enough that the hit bar is obvious to identify.

4.3.3 Energy resolution

The energy resolution of the absorber does not limit the angular resolution of the prototype in the same way the energy resolution of the scatterer does. Nevertheless the information on the energy of the scattered photon combined with the determined energy of the Compton electron in the scatterer is useful to separate true Compton from background events. This is extremely important in real imaging application when numerous photons are scattered in the imaged tissue, especially when low-energy radio-tracers such as ^{99m}Tc are used.

The energy resolution was measured for data collected in the calibration run. The source

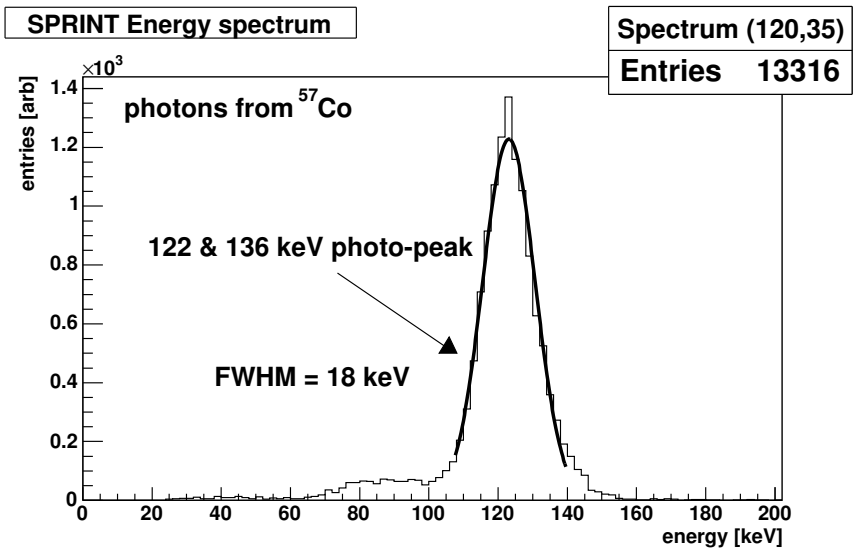

Figure 4.7: Energy spectrum of photons detected by SPRINT module in a single calibration position. Resolution is obtained by a Gaussian fit to the photo-peak of the 122 keV and 136 keV photons.

used was ^{57}Co source with principal γ-ray energies of 122 and 136 keV. The energy of the interaction was calculated using equation (4.3) and the determined gain map. Figure 4.7 shows a typical spectrum collected at a single calibration point. The threshold set for the CFD selects events with energy above the Compton edge, thus only events detected by photo-absorption are recorded. The measured energy resolution of 18 keV FWHM does not allow for the separation of the two ^{57}Co energy lines and a single peak is obtained. The resolution is determined by a Gaussian fit to the spectrum.

4.3.4 Timing resolution

A good timing resolution of the SPRINT module is required to correlate Compton events from the scatterer with the absorption of the scattered photon in the absorber.

The timing resolution was measured using a positron source. The positron annihilates in the shielding of the source and a pair of back-to-back photons is created simultaneously. In a calibration run, the first photon was detected in a fast plastic scintillator coupled to a PMT, and the (raw) output of the PMT was used as a timing reference providing timing resolution of 100 ps. The second photon was detected in a SPRINT module where the energy sum was fed into a constant fraction discriminator (CFD) to yield a digital trigger pulse. The raw pulse from the plastic scintillator and the digital trigger of the SPRINT were fed into a digital oscilloscope, where the delay between the pulses was measured.

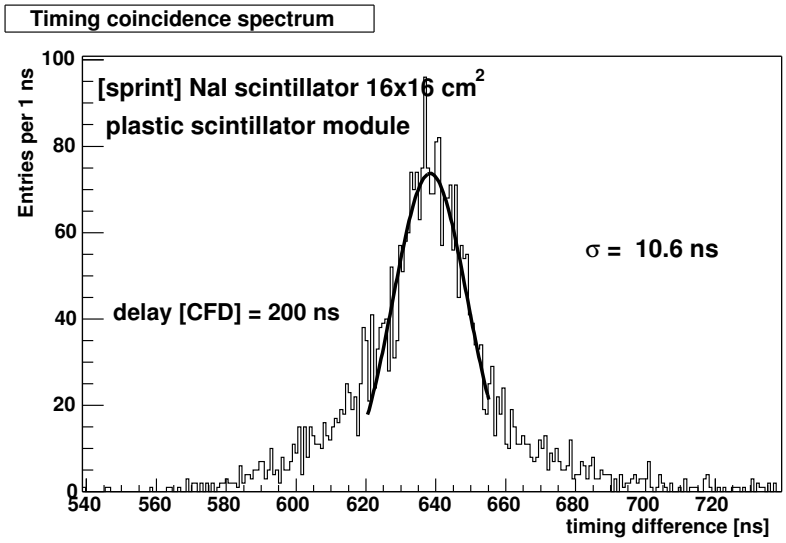

Figure 4.8: The difference between the trigger time of the plastic scintillator – PMT assembly and the SPRINT module, each sensor detecting a member of a photon pair produced by positron annihilation. ^{22}Na positron source was used.

Figure 4.8 shows the distribution of the delay between the pulses. A Gaussian fit to the distribution shows a timing resolution of 10 ns (variance) or 23.5 ns FWHM. Comparing this result to the timing resolution of the scatterer (Chapter 3) we see that the width of the timing correlation between the scatterer and the absorber will be dominated by the time resolution of the scatterer.

4.4 Conclusion

Suitability of SPRINT modules for the absorber in the Compton camera prototype was tested. A calibration setup was prepared to test the performance in terms of spatial, energy and timing resolution. The data were used to determine relative gains of the PMT, and improve the determined energy and position of the interaction.

A correction of the distortion based on the calibration data was used. After the correction an average spatial resolution of 4 mm FWHM was determined across the surface of the sensor. At a scatterer-absorber separation of 10 cm this corresponds to an angular resolution of 40 mrad which is comparable to the effect of the Doppler broadening and the angular resolution due to the finite energy resolution of the scatterer. While this may not be optimal for a final Compton camera, on the prototype level it only adds 40 % to the inherent spatial resolution and therefore complies to the requirements.

The angular resolution of Compton camera is not directly affected by the energy resolution

of the absorber, but the sum of energies recorded in the scatterer and the absorber is useful to reject the background events. The energy resolution of the sum is dominated by the energy resolution of the absorber which equals to 20 keV FWHM.

Timing resolution of the absorber is required for a proper matching of Compton scatter events in the scatterer to the capture of the scattered photon in the absorber. The trigger of a SPRINT module is based on the energy sum of the shaped outputs of all 20 PMTs discriminated by a constant fraction discriminator (CFD). The timing resolution of the trigger was measured to be 24 ns FWHM and the error on the timing correlation between the scatterer and the absorber is dominated by the resolution of the scatterer.

Using SPRINT at higher energies of the photons significantly affects the efficiency of the setup. At an energy of 140.5 keV the efficiency of the module with 1.27 cm thick NaI is close to 100 % and drops to approximately 60% at 250 keV and to approximately 10 % for 511 keV photons.

Chapter 5

Compton camera prototype

A Compton camera prototype was constructed in order to verify the theoretical principles and predictions for Compton camera performance. The prototype consists of two prototype parts: the scatterer and the absorber. The implementation of the prototype combines trigger signals from both parts into a system trigger; data from both parts represent a Compton scattering event. A set of scattering events is used by off-line software to reconstruct the source position. Performance of the prototype is determined primarily by the quality of data, which is given by performance of individual parts. The timing correlation between sub-detectors is also of great importance, because it provides interaction matching and data-sample purification. The timing correlation also determines the maximal source activity and amount of radio-active background, which can be tolerated in the setup. The last on the list of performance parameters is the data throughput in terms of event rate, a requirement directed towards read-out electronics rather than the core of the sensor operation.

The Compton camera prototype was constructed using the scatterer and absorber modules presented in the preceding chapters. The reasons for selection of the specific sub-detectors were given in the respective chapters. A simple geometry of the setup was chosen containing three SPRINT modules forming an incomplete ring with the scatterer modules set on the ring axis, following the arrangement suggested by previous Compton camera prototypes [LCH+98, MKW+93].

This chapter is devoted to the presentation of the prototype setup, both from mechanical and electronic point of view. The geometrical layout of the modules determines the theoretical properties that depend on the prototype geometry, such as the setup efficiency and the geometrical contribution to the error on spatial resolution of the source reconstruction. The procedure for the reconstruction of the source position is very complex and hence described in a separate chapter.

5.1 Mechanical layout

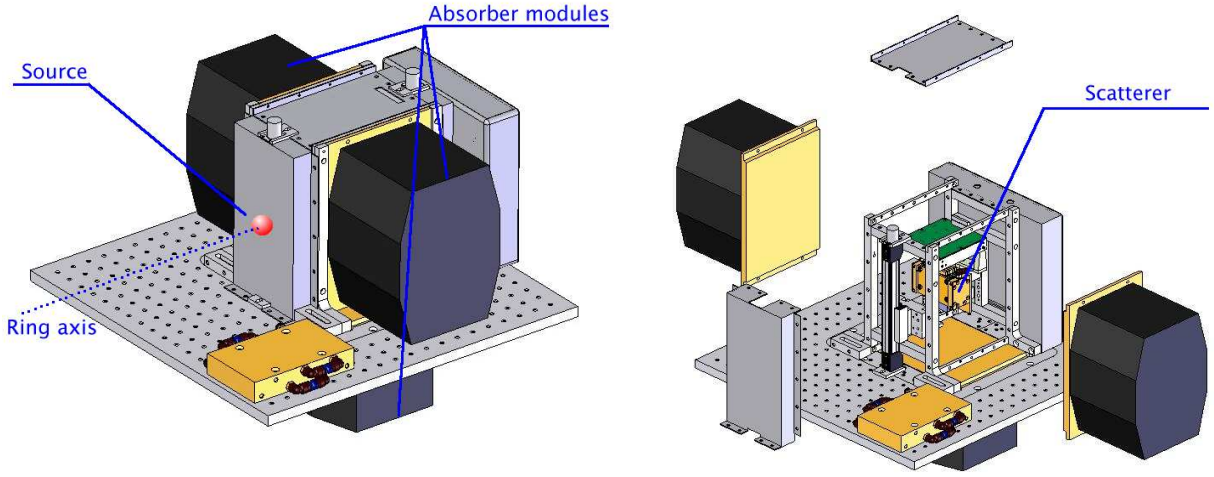

(a) (b)

Figure 5.1: Drawing of the layout of the Compton camera prototype: (a) – General view: three SPRINT modules (black) are arranged in an incomplete ring around the scatterer sensor in the center. (b) – Exploded view: the scatterer sensor is placed in the mechanical gantry at the center of the semi-ring.

The layout of the prototype is based on the ring concept developed by preceding Compton camera prototypes [MKW+93, LCH+99]. The layout of the prototype is illustrated in Figure 5.1. The central part of the prototype consists of the scatterer, which can made up of up to five scatterer modules, with inter-module spacing equal to 6.4 mm. The effective thickness of the scatterer can equal to 5 mm by using a set of five 1 mm thick scatterer sensors, thereby increasing the efficiency of the setup and Figure 5.2 shows the arrangement of the modules in the metallic gantry. Up to three SPRINT absorber modules can be used, two placed at opposite sides and one beneath the scatterer. The spacing between the center of the scatterer modules and the absorbers equals 6.7 cm for the two side modules and 8 cm for the module below the scatterer.

The prototype geometry is optimized for an on-axis source by means of scatterer module orientation and placement of absorber modules. The scatterer modules are placed perpendicularly to the ring axis to maximize the solid angle covered relative to the source. The absorbers provide detection of scattering angles centered around $\pi/2$ where spatial resolution is maximized. For on-axis source placement, ring geometry substantially reduces rate of direct hits of photons emitted by the source in the absorber [MKW+93], hence reducing pile-up effects. The alignment of scatterer and absorber modules is provided by precision mounting holes in the prototype frame.

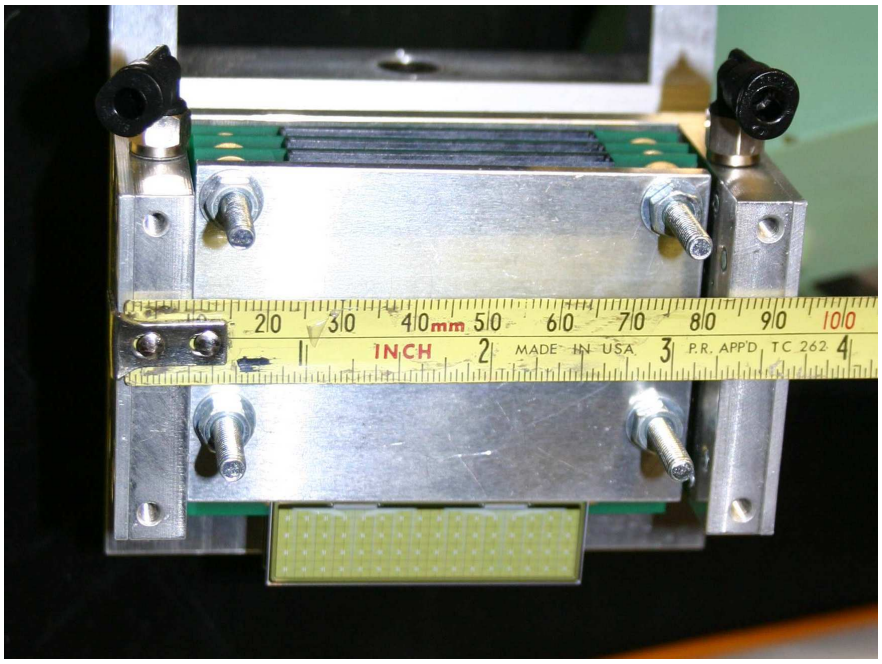

Figure 5.2: A photograph of the scatterer gantry with three out of the final five modules inserted.

5.2 Prototype parameters related to setup geometry

In Chapter 2 two prototype parameters that are related to specific prototype geometry were mentioned: the efficiency of the setup and the geometrical contribution to the angular resolution.

5.2.1 Setup efficiency

The efficiency of the setup for a given scattering angle θ and a fixed source position is given with:

$$\varepsilon(\theta) = P(\theta)a(\theta)(\Omega_1/4\pi)\varepsilon_2, \tag{5.1}$$

where $P(\theta)$ represents the probability that Compton scattering with a scattering angle θ will occur in the scatterer, $a(\theta)(\Omega_1/4\pi)$ is the combined geometrical probability that a photon emitted from the source hits the scatterer and that the photon scattered for θ is intercepted in the absorber, with Ω_1 the solid angle of the scatterer relative to the source, and ε_2 is the efficiency of the absorber for photo-absorption of the scattered photons.

The probability $P(\theta)$ is expressed with the Klein-Nishina differential cross-section $d\sigma/d\Omega$, given in the description of Compton scattering. Since $P(\theta)$ is defined per unit scattering

angle rather than the solid angle, the cross-section $d\sigma/d\theta$ is required. Using basic arithmetics and the fact that $d\sigma/d\Omega$ depends only on θ one gets:

$$\frac{d\sigma}{d\Omega} = \frac{1}{2\pi}\frac{d\sigma}{d(\cos\theta)} = \frac{1}{2\pi\sin\theta}\frac{d\sigma}{d\theta}, \tag{5.2}$$

$$\frac{d\sigma}{d\theta} = 2\pi\sin\theta\frac{d\sigma}{d\Omega}. \tag{5.3}$$

The differential cross-section is then expressed as the differential attenuation coefficient $d\mu/d\theta$ using equation (2.11) and multiplied by the sensor thickness w to obtain the probability:

$$P(\theta) = 2\pi\sin\theta\frac{w\rho Z N_A}{A}\frac{d\sigma}{d\Omega}. \tag{5.4}$$

For silicon, $Z = 14$ is the atomic number, $A = 28.086$ the atomic mass, $\rho = 2.33 g/cm^3$ the density of the scatterer material and N_A the Avogadro number.

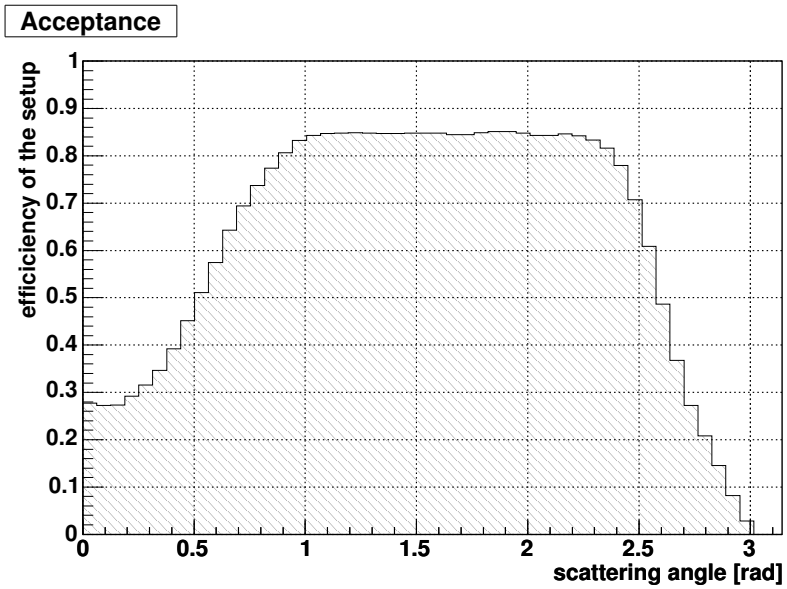

Figure 5.3: Acceptance $a(\theta)$ as a function of scattering angle θ for our prototype.

The geometrical factor $a(\theta)(\Omega_1/4\pi)$ or the acceptance depends on the source position and is composed of two related probabilities: the probability that a photon emitted by the source hits the scatterer in point $\vec{\mathbf{r_s}}$ and the probability that a photon scattered in point $\vec{\mathbf{r_s}}$ by angle θ hits the absorber. The average acceptance $a(\theta)$ equals to:

$$a(\theta) = \int_{S_s} d\,\vec{\mathbf{r_s}} p(\vec{\mathbf{r_s}})\frac{1}{2\pi}\int_{\Delta\phi_a} d\phi. \tag{5.5}$$

The average acceptance $a(\theta)$ is averaged over the surface S_s of the scatterer, with a geomet-

rical probability density that a photon will hit the area around $\vec{\mathbf{r_s}}$ given with:

$$p(\vec{\mathbf{r_s}}) = \frac{(\vec{\mathbf{r_s}} - \vec{\mathbf{r}})\hat{n_s}}{D^3}, \tag{5.6}$$

with $D = |\vec{\mathbf{r_s}} - \vec{\mathbf{r_a}}|$ and n^s normal vector of the face oriented towards the source. The directions of photon, scattered by scattering angle θ are parametrized using a polar angle ϕ, and the portion $\Delta\phi_a/2\pi$ of the cone is intercepted somewhere in the absorber. The average acceptance is then multiplied by the portion of the solid angle $\Omega_1/4\pi = UV/4\pi D_0^2$ covered by the scatterer with UV area of the side facing the source and D the distance between the source and the sensor. Figure 5.3 shows $a(\theta)$ calculated for the prototype geometry (Figure 5.1) and an on-axis source 5 cm from the scatterer.

The total efficiency of the setup is calculated as the integral:

$$\varepsilon = \int_0^{\pi} \varepsilon_2 \, (\Omega_1/4\pi) \, a(\theta) \, P(\theta) \, d\theta, \tag{5.7}$$

over the scattering angle θ. Under the assumption that all photons that hit the absorber are detected ($\varepsilon_2 = 1$), which is a reasonable assumption for photons of ^{99m}Tc, the efficiency for a point source set on axis of the absorber ring 5 cm from the scatterer equals to ε=3.7×10^{-4} per 1 mm of scatterer thickness.

5.2.2 Angular resolution

This sub-section continues the discussion on the angular resolution, first presented among the principles of Compton camera operation. The contributions to the resolution were described to be: the inherent resolution given by Doppler broadening, the contribution due to the limited energy resolution of the scatterer and the geometrical contribution due to the limited spatial resolution of the individual prototype parts. The former two were already described among the basic principles. The contribution to the energy resolution was given only with its functional dependence on the scattering angle while the amplitude was left to be determined after the energy resolution of the scatterer was discussed. The geometrical contribution depends on the setup geometry of a specific prototype implementation, and the determination of this contribution and combined angular resolution was reserved for this chapter.

For Compton scattering with a scattering angle θ the position of the source $\vec{\mathbf{r}}$ is related to the interaction positions $\vec{\mathbf{r_s}}$ in the scatterer and $\vec{\mathbf{r_a}}$ in the absorber via the geometric relation:

$$\cos\theta = \frac{(\vec{\mathbf{r_a}} - \vec{\mathbf{r_s}}) \cdot (\vec{\mathbf{r_s}} - \vec{\mathbf{r}})}{|\vec{\mathbf{r_a}} - \vec{\mathbf{r_s}}| \cdot |\vec{\mathbf{r_s}} - \vec{\mathbf{r}}|}. \tag{5.8}$$

Equation (5.8) hence determines the propagation of errors of measured impact positions to the error of the scattering angle. If $\sigma_S = (\sigma_{s,x}, \sigma_{s,y}, \sigma_{s,z})$ is the resolution of the scatterer and

$\sigma_A = (\sigma_{a,x}, \sigma_{a,y}, \sigma_{a,z})$ the resolution of the absorber, and $\vec{\mathbf{r_s}} = (x_s, y_s, z_s)$ and $\vec{\mathbf{r_a}} = (x_a, y_a, z_a)$, the geometrical contribution is determined as:

$$\sigma_\theta^2(\vec{\mathbf{r_a}}, \vec{\mathbf{r_s}}, \vec{\mathbf{r}}, \theta) = \left(\frac{\partial\theta}{\partial x_s}\right)^2 \sigma_{s,x}^2 + \cdots + \left(\frac{\partial\theta}{\partial x_a}\right)^2 \sigma_{a,x}^2 + \cdots . \tag{5.9}$$

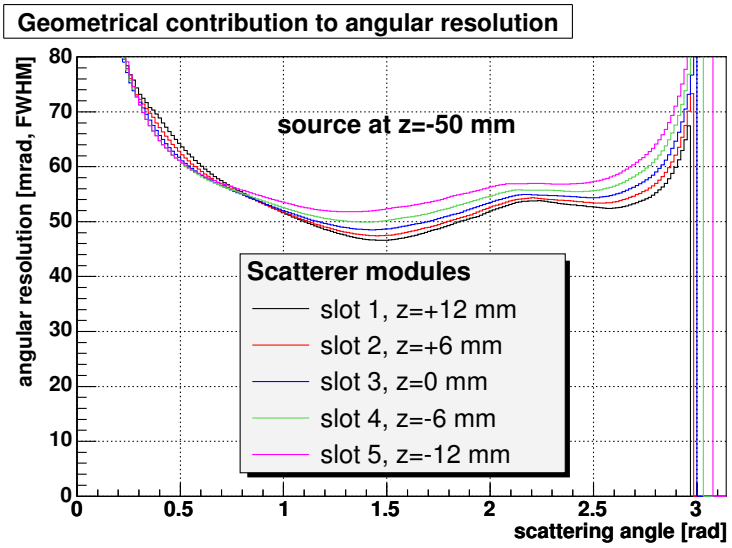

Figure 5.4: Geometrical contribution to the angular resolution for interactions in each of the five scatterer modules. The figure allows one to infer the average contribution approximately equal to the resolution of the central (z=0) module.

The partial derivatives are computed from equation (5.8):

$$\frac{\partial\theta}{\partial x_s} = \frac{1}{DR\sin\theta}\left[(x_a - x_s)(1 - \frac{D}{R}\cos\theta) - (x_s - x)(1 + \frac{R}{D}\cos\theta)\right], \tag{5.10}$$

$$\frac{\partial\theta}{\partial x_a} = \frac{1}{R^2\sin\theta}\left[\frac{R}{D}(x_s - x) - (x_a - x_s)\cos\theta\right], \tag{5.11}$$

where $D = |\vec{\mathbf{r_s}} - \vec{\mathbf{r}}|$ and $R = |\vec{\mathbf{r_a}} - \vec{\mathbf{r_s}}|$ and $\vec{\mathbf{r}} = (x, y, z)$. The derivatives with respect to the other components of impact points are obtained by a replacement of x with the corresponding component. The final resolution is obtained by averaging over all possible combinations $(\vec{\mathbf{r_s}}, \vec{\mathbf{r_a}})$ for a given scattering angle:

$$\sigma_\theta(\vec{\mathbf{r}}, \theta) = \frac{4\pi}{\Omega_1 a(\theta)} \int_{S_s} d\,\vec{\mathbf{r_s}} p(\vec{\mathbf{r_s}}) \frac{1}{2\pi} \int_{\Delta\phi_a} \sigma_\theta(\vec{\mathbf{r_a}}(\phi), \vec{\mathbf{r_s}}, \vec{\mathbf{r}}, \theta) d\phi, \tag{5.12}$$

where the outer integral runs over the scatterer's side facing the source and the inner over the azimuthal angles within the range $\Delta\phi_a$ covered by the scatterer. The azimuthal angle is

used to parametrize $\vec{\mathbf{r_a}}(\phi)$ which satisfy relation (5.8). When $a(\theta)$ equals 0, likewise $\sigma_\theta(\vec{\mathbf{r}}, \theta)$ is set to 0.

The integrals are calculated and shown in Figure 5.4, for interactions in each of the five slots available on the scatterer frame. Since the scatterer-absorber separation is not varied for different slot positions, the effect of variation of the source-scatterer distance is observed. The effect is negligible compared to the value of the resolution, and the average effect is well approximated by the contribution of the central slot.

The combined effect of Doppler broadening and limited energy resolution is calculated from the double-differential Klein-Nishina cross-section (DDKNXS) given by equation (2.10) and derived in the description of Doppler broadening. For a fixed scattering angle θ, the central energy of the Compton electron is calculated using the Compton equation (2.1). The Gaussian distribution centered at this energy with a width determined from the energy resolution Δ_E of the scatterer is then convoluted with DDKNXS, with the integral running over the energy of the Compton electron. The result of the convolution is a distribution with respect to the scattering angle, centered at θ and the FWHM of the distribution is the angular resolution for a specified scattering angle.

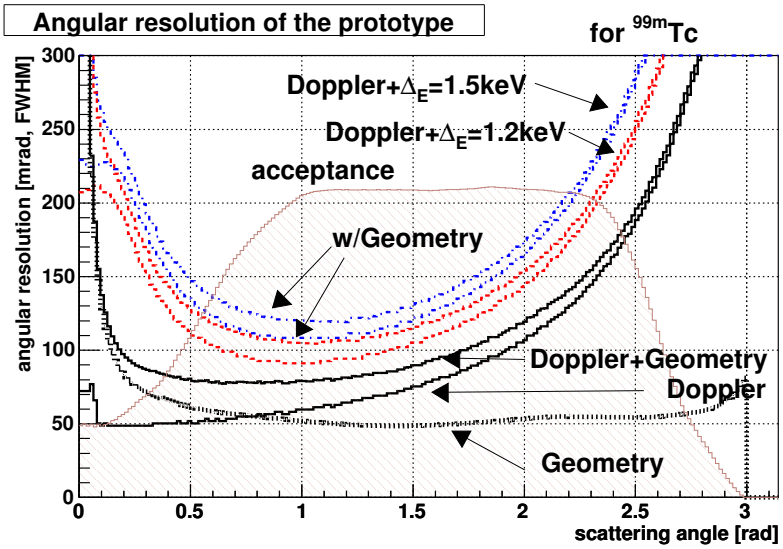

Figure 5.5: Angular resolution of reconstructed source position as function of scattering angle θ. Total resolution is shown for two scatterer energy resolutions (1.2 and 1.5 keV FWHM) and separate contributions of Doppler broadening and prototype geometry are shown. Geometrical contribution is calculated for the spatial resolution of 1.4 mm FWHM in the scatterer and 4 mm FWHM in the absorber and an on-axis source at 5 cm from the scatterer.

The combined angular resolution including all uncertainties is then calculated as a sum in squares of the uncorrelated geometrical contribution and the combined effect of Doppler

broadening and limited energy resolution. The graphs of all listed contributions and combinations is shown in Figure 5.5 for photons from ^{99m}Tc point source set on the axis of the absorber ring, 5 cm from the central slot of the scatterer gantry. The optimal performance is achieved for angles around 1 radian (60°), where all three contributions are approximately equal at 60 mrad FWHM, and overall predicted resolution of the prototype is at 120 mrad a factor of 2 larger than the inherent resolution.

5.3 Data acquisition system

The data acquisition (DAQ) system of the prototype is based on the DAQ systems of the parts of the prototype, with the readout triggered by a coincidence of interactions in both prototype parts.

For a Compton camera setup, the data is read out only when a coincidence of interactions in the scatterer and absorber occurs. The decision whether a pair of interactions is called a coincidence is based on the time difference between the trigger from the scatterer and the trigger from the absorber. The system trigger is generated if the time difference matches a pre-defined range.

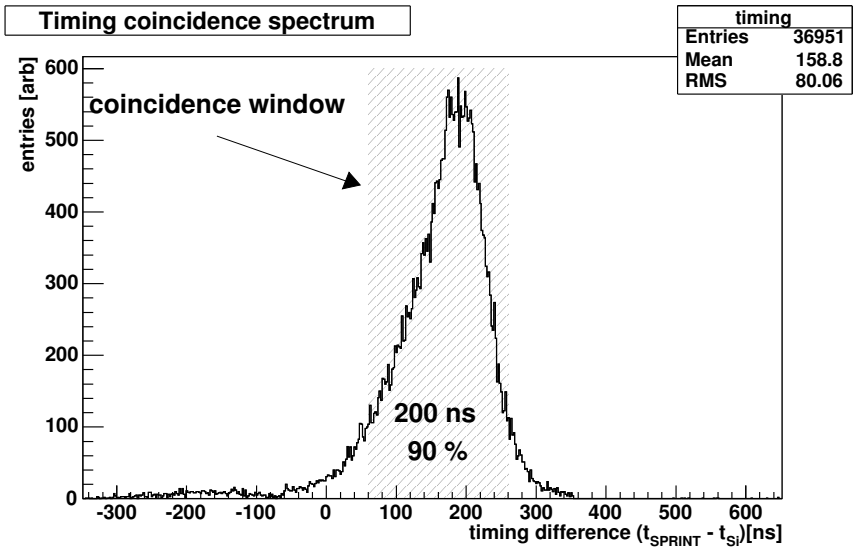

Figure 5.6: The coincidence peak in the difference between the trigger signal from the SPRINT module and the trigger signal from the scatterer. A coincidence window of 200 ns is shown which captures 90 % of the events in the peak.

Figure 5.6 shows the timing difference between the time t_{Si} of trigger from the scatterer and time t_{SPRINT} of trigger from a single SPRINT module, taken for source placed 5 cm from the scatterer. Direct hits in the absorber were prevented by lead shielding. A ^{57}Co source

was used as a replacement for ^{99m}Tc source. ^{57}Co source has two principal γ-lines in the emission spectra, 122 and 136 keV which are very close to the 140.5 keV line of ^{99m}Tc. The benefit of using ^{57}Co for on-bench experiments is its half life of 272 days which exceeds the half-life of ^{99m}Tc by several orders of magnitude. Figure shows a clear coincidence peak, dominated by the time-walk of the scatterer, and a time-window of 200 ns with a proper adjustment of additional delay of t_{Si} captures 90 % of the events in the peak.

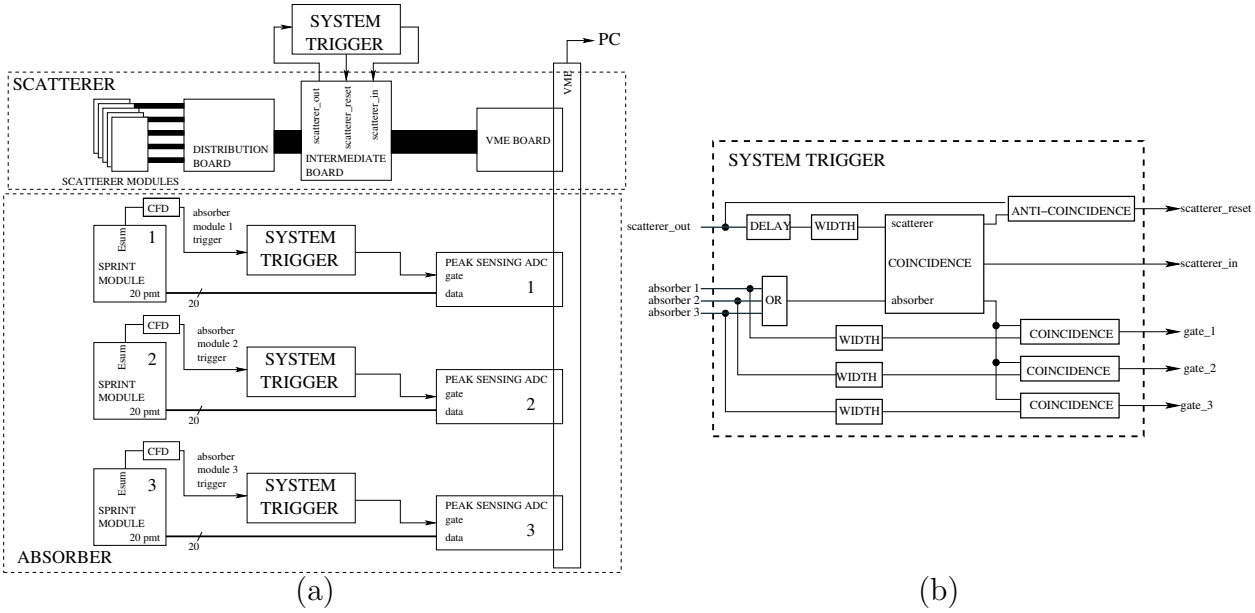

Figure 5.7: Block diagram of data acquisition system of the prototype: (a) general view, (b) schematic of the system trigger.

Figure 5.7b shows the implementation of the described technique for coincidence recognition. The pulse from the scatterer (`scatterer_out`) is generated by either of the scattering modules hooked to the readout chain by the distribution board. The additional timing delay of the trigger pulse is generated by a `DELAY` unit and the width of the timing-window where the interactions are considered coincident is set by the `WIDTH` unit. Each absorber has its own trigger pulse and a combination of each with the trigger signal of the scatterer signals a coincidence (`OR` unit). In the case of a coincidence, the scatterer readout is started by the `scatterer_in` signal, and a set of three `COINCIDENCE` units is used to identify the hit absorber module and to generate a gate for the corresponding Peak sensing ADC. If no coincidence is recorded a reset pulse (`scatterer_reset`) is sent to the scatterer. This is necessary since the interaction in the trigger starts a circuit which blocks all chips on the scatterer modules to prevent further triggers. The `scatterer_reset` unblocks the chips and enables subsequent triggers. The chips are normally enabled at the end of the data readout sequence.

The time necessary to read out the event is determined by two contributions: time necessary to read and digitize event in the VME module and time required by the PC to transfer and

manipulate the event. Presently the event read-out time is dominated by the contribution of the PC and up to 200 ms is required per event containing data from all five scatterer modules. This is reflected in the recorded event rate which is saturated at 50 Hz.

Figure 5.7a shows the full block schematic of the DAQ system. The individual parts were already presented in the chapters describing the corresponding prototype parts. A full event containing data from the scatterer and the hit absorber module is combined by the DAQ software on the PC. The subsequent processing is identical to combination of processing of the individual prototype parts with each part providing spatial and energy information.

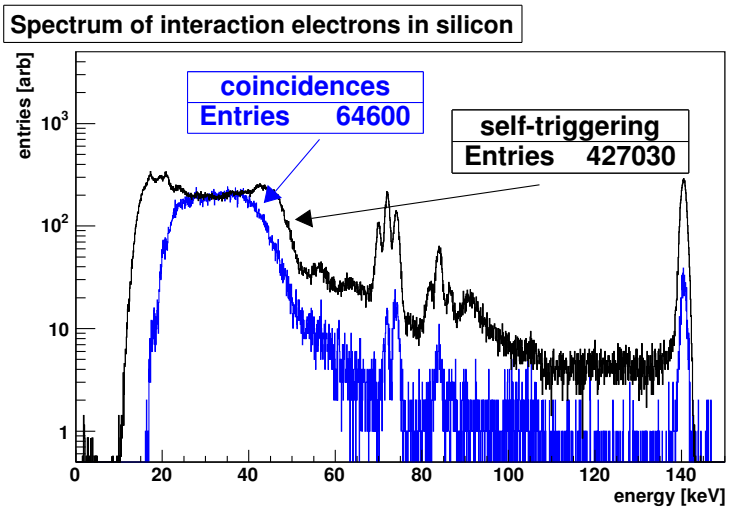

Figure 5.8: Spectrum of interaction electron energies recorded in the scatterer in self-triggering mode and during a coincidence data run. For a single module (`lj3557a`) and photons from ^{99m}Tc.

The scatterer data yields the ID of the hit pad, which is then converted to a location of the pad in arbitrary coordinate system using data on prototype geometry, and the common-shift-corrected pedestal-subtracted and gain-corrected energy of the Compton electron. A comparison of the energy spectra of interaction electrons recorded in the run with the absorbers and in self-triggering mode is shown in Figure 5.8. The run was performed with a ^{99m}Tc source. Most of the events in the coincidence spectrum were caused by Compton electrons; the rate of interactions due to photo-absorption is substantially reduced compared to the spectrum taken in self-triggering mode. Photo-absorption events in the scatterer in the coincidence run are only recorded for false coincidences and are a measure of data purity. The measured spectrum in Figure 5.8 points to a low rate of false coincidences. The events with low energy of the Compton electron are cut (as observed in the coincidence spectrum) by the coincidence timing window, since they represent a long tail to the left of the coincidence peak shown in Figure 5.6, and shifting the timing window in that direction, the rate of random-coincidences is substantially increased.

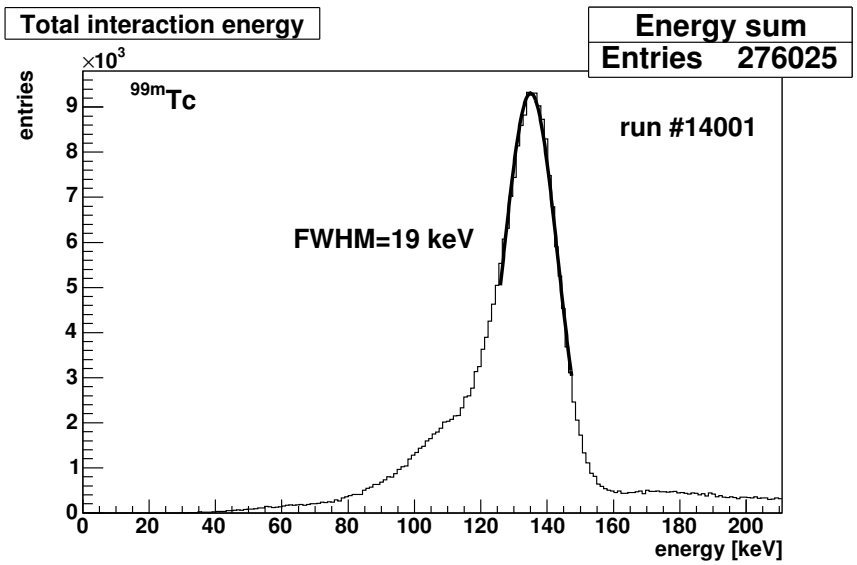

Figure 5.9: The spectrum of sum of energy recorded in the scatterer and the absorber. For 140.5 keV γ-rays from ^{99m}Tc recorded in 5 scatterer modules and a single SPRINT head.

The impact point in the absorber is determined using a centroid method, corrected by the distortion map (Chapter 4, equation (4.6)). The energy is calculated using the gain map from the calibration and with a further correction based on the determined impact position. Figure 5.9 shows a spectrum of the sum of interaction energy in the scatterer and in the absorber for a trial run with the maximum of 5 scatterer modules and the absorber consisting of a single SPRINT module. This sum spectrum is centered at approximately ^{99m}Tc principal γ-ray energy of 140.5 keV and the resolution of 19 keV FWHM is obtained from a Gaussian fit to the peak.

The final output of the processing routine is a list of variables for each interaction event: the impact position in the scatterer, the energy of the Compton electron, recorded in the scatterer, the impact position in the absorber and the energy collected in the absorber. A list of data for all events is then used by the program, which reconstructs the image – the spatial distribution of the sources.

Chapter 6

Image reconstruction

The Compton camera is an imaging device, and a vital part of data analysis is the image reconstruction. The task of the reconstruction algorithm is to determine the distribution of radioactive sources based on collected data. The input to the reconstruction algorithm is a list of events, with each event containing impact positions in both parts of the prototype and the respective recorded energies. The output is a three-dimensional histogram filled with probabilities that the source is present in a certain voxel–bin of the histogram.

The intention of the image reconstruction was the evaluation of the prototype, hence a simple back-projection was used. When a more precise source distribution is sought, there are a few more refined methods available. They can be split into analytical and approximate reconstruction methods, and an approximate method suitable for our application, called expectation maximization list-mode maximum likelihood is described in Appendix B.

6.1 Definition of problem

The imaging problem is posed as follows: the distribution of sources is given with a (scalar) field $S(\vec{\mathbf{r}})$ or an image, which describes the relative intensity (concentration) of the radionuclide at a point $\vec{\mathbf{r}}$ in real space, the space also referred to as the source space. The photons emitted by the sources are detected in the detector and each event consists of measurement of several parameters. For a Compton camera, those are the interaction position $\vec{\mathbf{r_s}}$ and energy E_s recorded in the scatterer and the hit position $\vec{\mathbf{r_a}}$ in the absorber[1], and an 7-dimensional vector $\mathbf{y} = (\vec{\mathbf{r_s}}, E_s, \vec{\mathbf{r_a}})$ representing a possible scattering realization is formed. The basic principles of Compton camera and the information on the geometry of the setup are used to

[1]The energy E_a recorded in the absorber is used only for rejection of background events and is not a part of image reconstruction data

determine the probability:

$$f(\mathbf{y}|S(\vec{\mathbf{r}})), \tag{6.1}$$

that a realization $\mathbf{y}$ is measured given a source distribution $S(\vec{\mathbf{r}})$. The vectors $\mathbf{y}$ span the measurement space and using the probability $f()$ a scalar field (image) $M(\mathbf{y})$ is formed as:

$$M(\mathbf{y}) = f(\mathbf{y}|S(\vec{\mathbf{r}})), \tag{6.2}$$

with values of $M()$ varying between 0 and 1. $M(\mathbf{y})$ is viewed as a representation of the spatial distribution $S(\vec{\mathbf{r}})$ in the measurement space. Also, equation (6.2) shows how a measurement image $M(\mathbf{y})$ is constructed from the given spatial distribution and the inverse - obtaining the source distribution from the measurement image - is called the image reconstruction.

Since the imaging system is linear, equation (6.2) can also be written in a matrix form, providing the measurements $M()$ and the source distribution $S()$ are discreticized. The measurement space is binned along all directions, i.e. the energy and position measured in each part of the prototype, and a single index is used to denote a bin in this multi-dimensional histogram. A similar procedure is done on the source space, where a single index is used to identify a position within the source distribution. The number of measurements m_j in each bin of the measurement space grows linearly with N_e, the number of detected events, and the approximation to the measurement image as defined above is obtained by division of m_j with N_e: $M() \rightarrow m_j/N_e$. The source distribution is given with $S() \rightarrow s_i$ and along with m_j they are viewed as vectors, related by the system transfer matrix $\underline{T}$:

$$m_j = \sum_{i=1}^{N} \underline{T}_{ji}\ s_i, \tag{6.3}$$

with N the number of bins used to discreticize the source space. The matrix elements T_{ji} are obtained as:

$$\underline{T}_{ji} = N_e \int_{W_j} d\ \vec{\mathbf{y}}_\mathbf{j}\ f(\vec{\mathbf{y}}|S_i), \tag{6.4}$$

where W_j is the (hyper-) volume of bin j in the measurement space, $\vec{\mathbf{y}}_j$ the central measurement vector of bin j and S_i a source distribution with a single source with unit intensity placed at $\vec{\mathbf{r}}_\mathbf{i}$, the center ob bin i.

The finite N_e of measurements allow for formation of an approximate image $M'(\mathbf{y})$ and there are two distinct approaches to obtaining the source distribution $S(\vec{\mathbf{r}})$: an analytic and an approximate reconstruction.

The analytic reconstruction inverts $\underline{T}$ directly, and based on the measurement collection m'_j the related source intensities s_i are obtained:

$$s_i = \sum_{j=0}^{M} \underline{T}^{-1}_{ij} m'_j, \tag{6.5}$$

with M the number of bins used to discreticize the measurement space. There are several complications involved in using the analytical approach: the errors of the data set m'_j, its incompleteness and a large amount of computer power required for storage and manipulation of the transfer matrix. The effect of the measurement errors on the obtained image can be quite large, since the transfer matrix $\underline{T}$ tends to be ill-conditioned. This was observed by Parra [Par00] and an adequate solution was proposed. The solution, however, requires a full set of measurement data to be known, i.e. all range of scattering angles. The problems related with obtaining a full set of measurements (threshold in the scatterer, solid angle covered by the absorber) combined with the fact that measurements will always contain errors remain a draw-back of the analytical method. New methods are proposed [TH03], which give an analytical solution even on a limited data set with measurements errors. However, even with this problems solved, harsh requirements related to the computational power remain. Analytical methods require the storage and manipulation of the transfer matrix $\underline{T}$, which is of dimension $M \times N$. For example - the prototype consists of $N_S = 10^3$ scatterer channels, $N_A = 10^4$ absorber channels and the energy of the scatterer is binned in $N_E = 10^3$ bins, which gives $M = 10^{10}$. Let's consider a cubic source grid with a lattice of 3 cm and a bin of 1 mm^3, or N=3×10^4. An analytical reconstruction would require manipulation of matrix with 3×10^{14} of entries, and assuming 4 bytes per bin, manipulation of PByte of data is required, which is practically impossible.

Approximate methods can operate without the complete knowledge of T_{jk} and are hence less demanding on the computing system. Because of that they were the reconstruction methods of most of the so-far constructed prototypes. A maximum likelihood approach was developed by Herbert and Singh [HLS90], and Wilderman derived an expectation maximization algorithm for maximum likelihood on list-mode data [WFC$^+$01] in 1998. The common approach of approximate methods is the following: assume a Poison distribution of m_j number of entries in each bin j of the measurement space, determine the average content $m'_j = \sum_{i=1}^{N} \underline{T}_{ji} s_i$ for the sought source distribution s_i, and use maximum likelihood to determine unbiased estimators for s'_i. Since maximum likelihood produces a set of N coupled equations for s'_i, the solution is sought iteratively, and an approximate solution is reached. The measurement errors are included in the system matrix elements $\underline{T}_{ji}$ and incompleteness of the data set is taken into account by evaluating m'_j only for a limited volume of measurement space; for list-mode only bins containing measurements are taken. Expectation maximization list-mode maximum likelihood as given by [WFC$^+$01] is described in Appendix B as an example of an approximate reconstruction method.

There are some remaining problems of Compton camera image reconstruction, which are not solved by any of the listed methods. For example, the image is reconstructed in a limited space, and a 0 probability is assumed for points lying outside of the reconstructed region. For extended objects this causes edge artifacts, which can be only removed by careful modeling of expected tissue uptake [Zha04] prior to measurement. Even so, the noise of those events remains in the reconstructed image.

6.2 Back-projection of data from Compton camera

The back-projection of the scatter data forms an image in the source space, with each bin reflecting the probability that a detected event was caused by a photon emitted from this bin of the image. The bins placed at the true location(s) of the source(s) will have this probability larger than their distant counterparts, and the back projection is a simple approximation of the source distribution. This approximation is then conveniently used as the initial approximation for the approximate reconstruction algorithms.

The back-projection of an event is determined from the measured impact positions in both parts of the sensor: $\vec{\mathbf{r_s}}$ in the scatterer and $\vec{\mathbf{r_a}}$ in the absorber. From the energy E_e of the Compton electron, measured in the scatterer, the scattering angle θ is determined via Compton equation (2.1).Then the back projection corresponds to a set of vectors $\vec{\mathbf{r}}$ which satisfy the equation:

$$\cos\theta = \frac{(\vec{\mathbf{r_s}} - \vec{\mathbf{r}}) \cdot (\vec{\mathbf{r_a}} - \vec{\mathbf{r_s}})}{|\vec{\mathbf{r_s}} - \vec{\mathbf{r}}| \cdot |\vec{\mathbf{r_a}} - \vec{\mathbf{r_s}}|\cdot}. \tag{6.6}$$

Geometrically, the set of $\vec{\mathbf{r}}$ form a cone of possible locations of the photon source. The three-dimensional problem is reduced to a two-dimensional (2D) one by calculating the projection of the cone on a fixed focal plain. The focal plain is set perpendicular to the axis of the absorber ring and a set of 2D slices is formed when three-dimensional (3D) information is required. The curves formed by intersection of the focal plane with a cone are of three mathematical types (ellipses, hyperbolas and parabolas), but will be henceforth labeled ellipses with no loss in generalization, since the exact shape of the curve plays no role. A fast list-mode back-projection algorithm, implemented by Wilderman [WRKE98] is used to find ellipses for individual events: first the intersection of the ellipse with the boundary of the plane is determined and then the ellipse is traced until another boundary is reached. The hit pixels are assigned a weight:

$$w_i^e = \frac{1}{c^e}\frac{1}{r_{is}}\frac{\ell_i^e}{\ell_{\text{total}}^e}, \tag{6.7}$$

with c^e circumference of ellipse corresponding event e, r_{is} is the distance between the hit pixel and the interaction point $\vec{\mathbf{r_s}}$ in the scatterer, and $\ell_i^e/\ell_{\text{total}}^e$ the length of the ellipse contained in pixel i scaled with total length ℓ_{total}^e of the ellipse segment contained within the plane boundary. The first weighting factor reflects the amount of information contained per unit length of the ellipse – a narrow cone may completely determine the position of the source as the circumference of the ellipse in the focal plane is small. Such events are obtained both for scattering angles close to 0 or π radians. The second factor accounts for $1/r$ dependence of the cone radius and the last aims at sub-pixel resolution by reducing the weights of pixels which contain only a small portion of the ellipse.

The back-projected image of the measured data set is obtained by summation of the weights

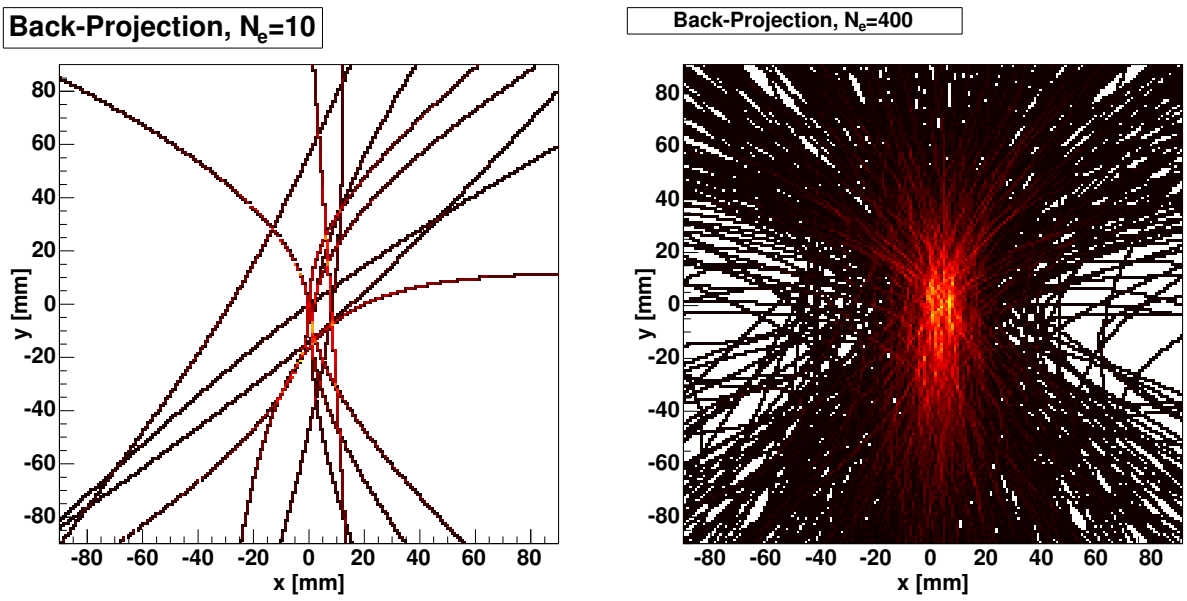

(a) (b)

Figure 6.1: Intermediate steps in back-projection after N_e=10 (a) and N_e=400 (b).

w_i^e over all events e:

$$w_i = \sum_{e=1}^{N_e} w_i^e. \tag{6.8}$$

This effectively shows the position of the source by intersection of the ellipses. For illustration, ellipses obtained for a sample of N_e=10 (a) and N_e=400 (b) events are drawn in Figure 6.1. For a final image $N_e = 10^5$ or more is used. Back-projection weighs events independently of the angular resolution, which was shown in Chapter 5 to be primarily related to the scattering angle. This information is however used in approximate reconstruction techniques such as expectation maximization list-mode maximum likelihood, which reduce the relative weight of events with low expected angular resolution.

6.3 Reconstructed images of point sources

The back-projection method described above was used to de-convolute the data collected for point-like radio-active sources in the prototype described in Chapter 5. The source was placed on the axis of the absorber semi-ring, at a distance of approximately 5 cm from the central scatterer module. The z-axis was chosen to point along the axis of the semi-ring, x-axis joins both modules at the side and the remaining y-axis is set in the direction which is covered by the single absorber module. A fixed number of counts N_e was collected, with N_e ranging from $1{\times}10^5$ to $1{\times}10^6$. The radio-nuclide used was ^{99m}Tc.

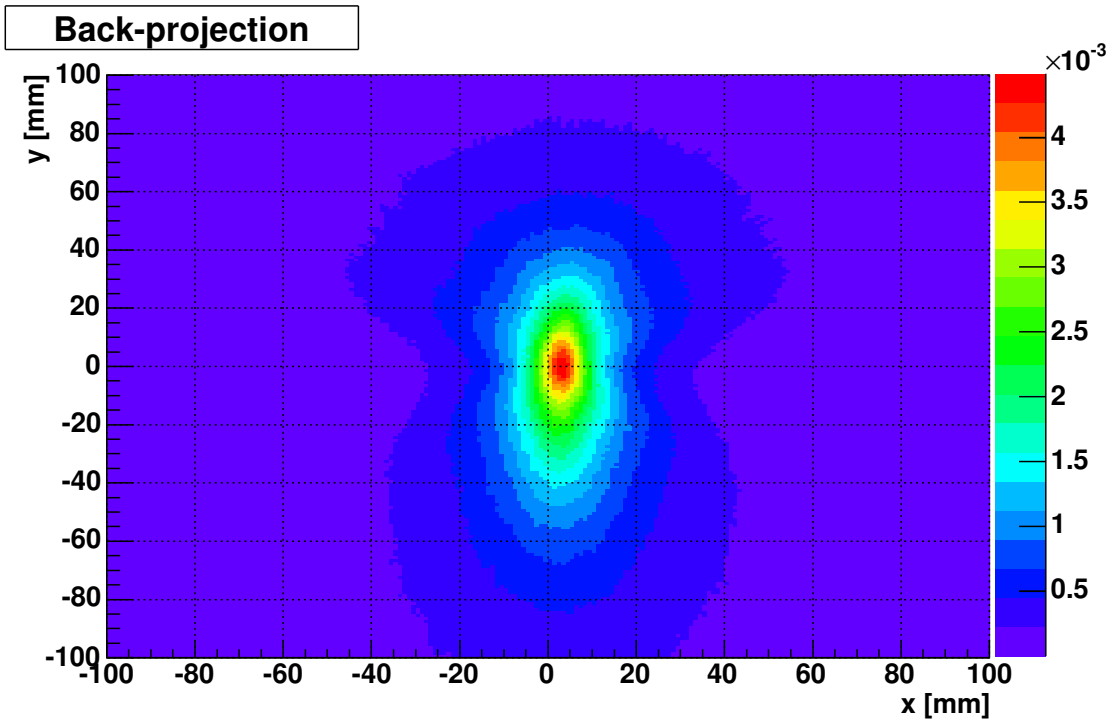

Figure 6.2: Reconstruction of a point source. The distance between the focal plane and the source was 5 cm, which is approximately equal to the actual separation. 250 000 events were used in the reconstruction.

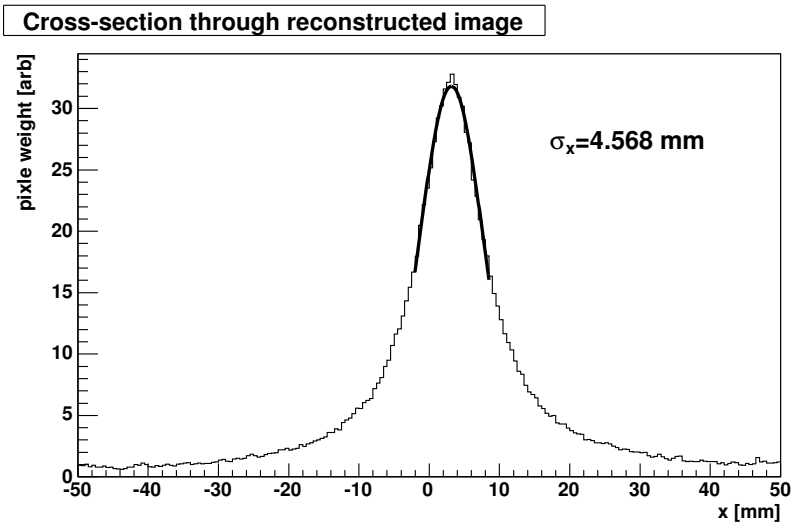

Figure 6.3: Cross-section along the image plane in x direction. A Gaussian fit is used to determine the resolution of the point source. The variance of σ_x=4.57 mm corresponds to an angular resolution of 210 mrad at 5 cm source-scatterer distance.

The result of the reconstruction is shown in Figure 6.2 The focal plane was located approximately at the position of the source, i.e. 5 cm from the face of the central out of the five scatterer modules. Only the two absorber modules at the sides of the prototype were used for technical reasons . Such setup gives a good resolution in x direction, and the lack of solid angle coverage reduces the resolution in y direction, which is observed in Figure 6.2. In further analysis only resolution in x dimension is given since it is judged representative of the prototype. For Figure 6.2, N_e= 250 000 events were used in the reconstruction.

Figure 6.3 shows a cross-section along x-axis of the histogram shown in Figure 6.2, cutting through the center of the source. A Gaussian fit in a narrow range around the histogram peak is used to determine the spatial resolution. The whole distribution is in fact far from Gaussian, with large tails added by the back-projection algorithm. For all events a reconstruction of 210 mrad full width at half maximum is determined. Since the angular resolution (Figure 5.5) depends on the scattering angle of the Compton interaction, this is an average resolution, obtained by averaging the resolution over the range of detected scattering angles. Since the angular resolution has a broad minimum around the scattering angle of 1 radian, selecting events around that minimum will improve resolution of the reconstructed image. Portion of such events depends crucially on the module geometry, i.e. acceptance, and the minimal detectable energy in the scatterer.

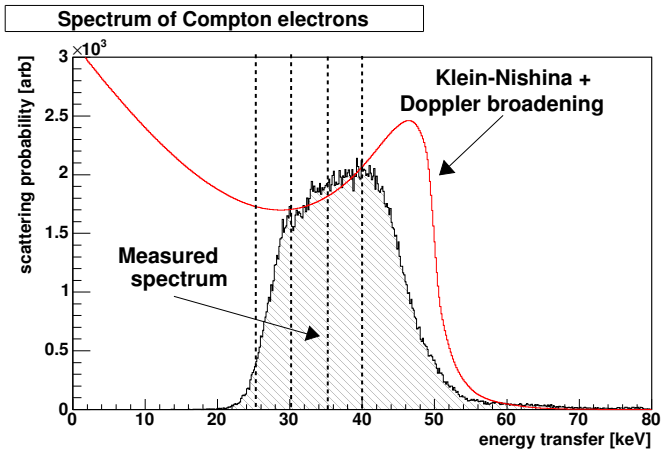

Figure 6.4: Spectrum of Compton electrons measured for recorded events. Combination of Klein-Nishina differential cross-section and Doppler broadening is added as a reference. The dashed lines represent bins of data for determination of the relation between angular resolution and scattering angle, shown in Figure 6.5.

The scattering angles are computed from the measured energy of Compton electrons in the scatterer by equation 2.1. The range of scattering angles is hence obtained from the range of Compton electron energies. Figure 6.4 shows the spectrum of Compton electrons, obtained from collected data. For comparison, the spectrum predicted by a combination of Klein-Nishina formula (2.13) and Doppler broadening (2.10) is drawn. The parts missing from the

measured spectra relative to the prediction are due to limited prototype acceptance and the cut in data caused by the setting of coincidence window. Data were segmented according to the scattering angles for further analysis.

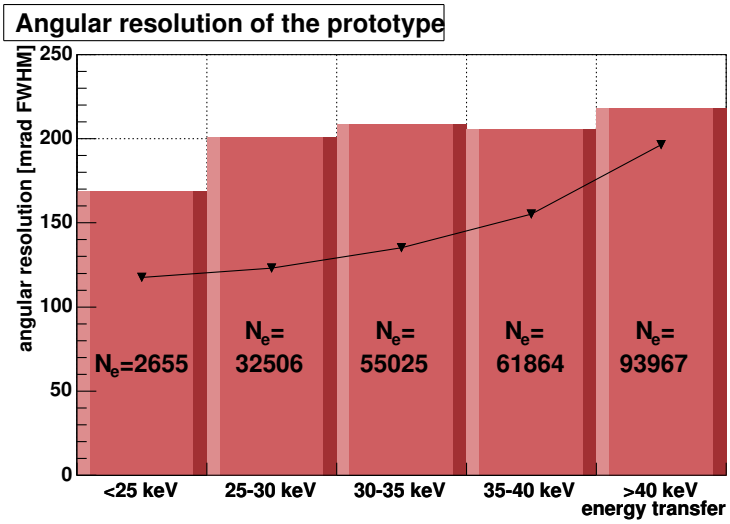

Figure 6.5: Measured angular resolution of prototype (bars) as function of energy transfer (or scattering angle) compared to the predicted resolution (triangles), taken from Figure 5.5. N_e corresponds to number of events reconstructed for each bin in energy.

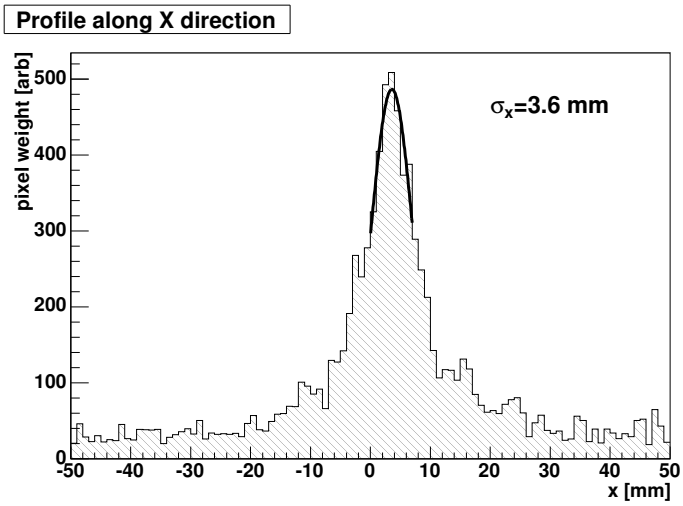

Figure 6.6: Cross-section along the image plane in x direction for events with energy transfer below 25 keV. The Gaussian fit is still reasonable, giving a variance of σ_x=3.6 mm corresponding to an angular resolution of 170 mrad at an average separation of 5 cm between the source and the scatterer.

Figure 6.5 shows the spatial resolution of the reconstruction, determined from the Gaussian fit as described above, for data within a limited range of energy transfer or conversely, scattering angle. As predicted, the resolution decreases with growing scattering angle and optimal resolution is obtained for the smallest measurable scattering angle. The limit of the lowest bin of histogram in Figure 6.5 was intentionally moved lower at the expense of lower statistics collected in the bin to achieve maximal resolution. In elaborate reconstruction methods the events with better resolution, i.e. those obtained at lower scattering angle are attributed larger relative weight.

Figure 6.6 shows a cross-section through the focal plane for Compton events with energy transfer below 25 keV. The statistics still allows for a reasonable Gaussian fit yielding spatial resolution of 3.6 mm (variance) corresponding to angular resolution of 170 mrad. This result agrees with the predicted resolution of 120 mrad within the reliability frame of the back-projection reconstruction method.

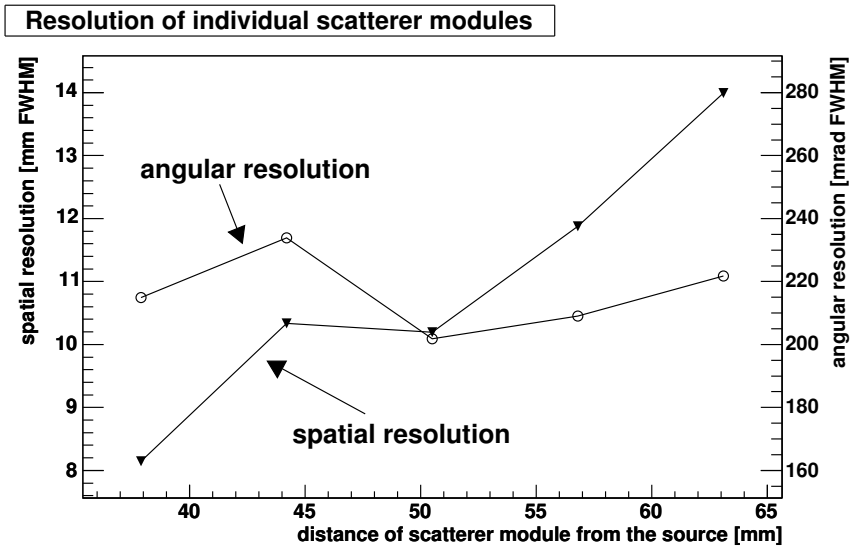

Figure 6.7: The resolution of the reconstructed source position as a function of the distance between a scatterer module and the source. The angular resolution (shown with circles) is determined from the spatial resolution (triangles) with the given separation between the individual module and the focal plane.

The fact that five scatterer modules were used allows for measurement of angular resolution as a function of the distance between the source and the scatterer. Ideally, the spatial resolution is proportional to the distance, and deviations are expected when distance decreases. Figure 6.7 shows that a good linearity is maintained for distances down to 4 cm, where the measured spatial resolution is 8 mm FWHM and, as expected, constant angular resolution.

6.4 Conclusion

Back-projection is a simple reconstruction method, which reconstructs the position of the source on an event-by-event basis. The three-dimensional problem is reduced to a two-dimensional one by selecting and binning a fixed focal plane. For each event, a cone of possible positions of the source is constructed and bins, intersected by the cone, are filled. The process is repeated for all detected events, yielding an approximate distribution of the sources on that plane.

The method was used to reconstruct data of a point ^{99m}Tc source placed on axis of the absorber ring, collected in the prototype described in this thesis. The prototype for the specific run consisted of all five scatterer modules and two absorber modules set at both sides of the scatterer gantry. Such setup allows for a good resolution along a single direction, the line joining both absorber modules, and results obtained in this direction are assumed representative.

Using all 250 000 events collected with all five scatterer modules and two absorber modules an average resolution of 210 mrad is obtained. The measured dependence of angular resolution on the Compton electron energy matched the predicted response within the reliability of the back-projection reconstruction method. The best resolution was obtained for data collected at energies below 25 keV or conversely, below a scattering angle of 1.35 rad (80°), where a spatial resolution of 8 mm (170 mrad) FWHM was measured. The resolution as a function of the distance between the source and the scatterer module was determined using data from different scattering modules. The prototype shows no degradation for small distances, and an angular resolution of 200 mrad FWHM is kept down to a 3.8 cm separation between the source and the scatterer module.

Chapter 7

Prototype evaluation

The imaging based on the Compton camera principle is a novel technique of SPECT imaging, used to reconstruct spatial distribution of γ-rays sources. As it requires no mechanical collimator between the sources and the detector it effectively overcomes the efficiency-resolution trade-off imposed by mechanically collimated imaging devices, i.e. Anger cameras. The imaging performance of Compton camera improves with growing energy of the initial photons, which may fuel the development of radio-pharmaceuticals with larger gamma-ray energies, where the imaging is less influenced by photon scatter in the patient's tissue.

The presented thesis focused on development of a suitable primary detector, the scatterer, for a Compton camera. Silicon pad sensors with optimized detector geometry and read-out were developed and found to meet the harsh requirements for a Compton camera scatterer. The absorber of the prototype on the other hand consisted of modules designed for a different setup, but fitting nicely to our requirements. The prototype was assembled on a custom made mechanical frame and the data acquisition system consisted partially of custom made electronics and partially of off-shelf integrated circuits. All parts of the setup were tested and calibrated prior to prototype operation, and the calibration data was used to improve and evaluate module performance. The assembled prototype was tested using point-like radioactive sources emitting photons of energies used for SPECT imaging. Image reconstruction was performed using a simple back-projection algorithm and spatial resolution of down to 170 mrad FWHM (for the optimal scattering angle range) was determined for a point source, which is in good agreement with expected performance.

This chapter evaluates the imaging performance of the presented Compton camera prototype, together with individual sub-detector performance. There are two main evaluation parameters of a Compton camera setup: its spatial resolution and efficiency. Both will be discussed in turn, along with possible upgrades of presented simple device to a more sophisticated Compton camera application. A comparison with elaborate Anger cameras is given showing how competitive Compton imaging is, even for a very crude prototype.

7.1 Measured results

7.1.1 Spatial resolution

The spatial resolution of the prototype was determined using a simple back-projection algorithm, which is not an optimal estimator for reconstruction of the source positions, and the resolution is expected to improve when elaborate methods (e.g. Expectation maximization list-mode reconstruction, Appendix B) are used. The back-projection however, is a good tool for evaluation of the performance of the prototype.

When Compton camera is discussed, spatial resolution is determined from angular resolution using the known separation between source and primary detector, the scatterer. The predicted angular resolution is composed of three contributions: Doppler broadening, effect of limited energy resolution of the scatterer and geometrical contribution. All three were found to be of equal magnitude when determined for photons with energy of 140.5 keV from ^{99m}Tc source. Since Compton camera is aimed to be also used at higher energies of initial photons where both Doppler broadening and the effect of energy resolution of the scatterer decrease significantly, the relatively large geometrical contribution is a draw-back of the current prototype.

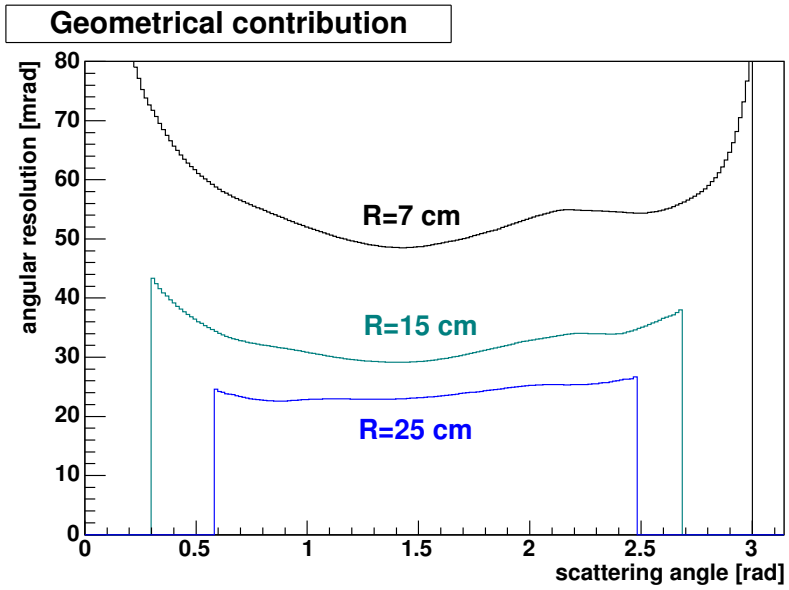

Figure 7.1: Geometrical contribution of a hypothetical prototype with a distance d between the scatterer and the absorber increased to R=15 cm and R=25 cm compared to the contribution of the present prototype with R=7 cm.

Geometrical resolution of the current prototype is determined by spatial resolution of the sub-detectors and their separation. Improving spatial resolution of the scatterer contributes

negligibly to geometrical contribution, and the improvement is at the expense of significant degradation of energy resolution because of signal sharing between adjacent pads. The spatial resolution of the absorber can be improved with a finer segmentation of NaI(Tl) crystals and decreased size (increased number!) of PMTs, but a much simpler method is to increase the separation between the scatterer and the absorber. Using equations used to determine the resolution of the present prototype (5.9-5.12), the resolution of a hypothetical prototype with the same absorber modules placed 15 cm or 25 cm from the scatterer is shown in Figure7.1. Without increasing the number of absorbers to maintain the same scattering angle coverage, increasing the separation however changes the prototype efficiency, as shown in Figure 7.3.

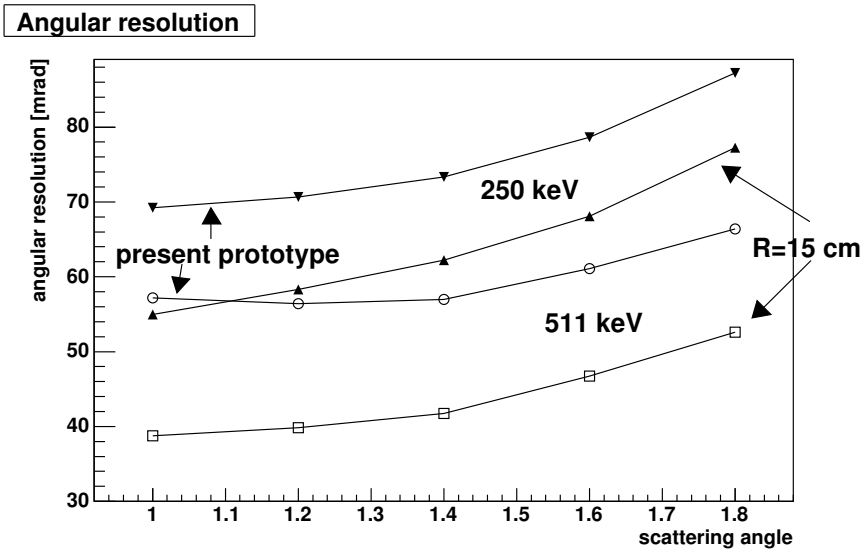

Figure 7.2: Total resolution of the prototype with a distance d between the scatterer and the absorber increased to R=15 cm compared to the original prototype with R=7 cm, for photons from ^{111m}In (energy 250 keV, solid markers) and a positron source (511 keV, shallow markers).

The improvement in angular resolution of the prototype when the absorbers are moved further from the scatterer becomes significant when initial photons with higher energy are detected. Figure 7.2 shows the angular resolution determined for photons from ^{111m}In with energy of 250 keV and annihilation photons, both for the original prototype and a hypothetical prototype with separation between scatterer and absorber increased to 15 cm. At a scattering angle of 1 radian, the improvement is approximately 10 mrad for 250 keV photons and 20 mrad or one third for 511 keV photons.

Previous Compton camera prototype, C-SPRINT [LCH$^+$99], had different geometry, with a larger ($d = 25cm$) distance between the scatterer and the absorber and scattering angles covered by the absorber were in a limited range (80° to 110°) where spatial resolution is optimized. To compare the obtained resolutions of both prototypes, the present prototype should be transformed to a hypothetical prototype with absorbers placed at the same dis-

tance and detected angles range should equal that of C-SPRINT. Using equations (5.9-5.12) the resolution of the hypothetical prototype with measured 1.4 keV energy resolution of the scatterer is 100 mrad compared to 150 mrad obtained in C-SPRINT. The significant improvement in angular resolution is due to a factor 2 improved energy resolution of the scatterer.

7.1.2 Efficiency

The predicted efficiency of the prototype was determined as ϵ=1.6×10^{-3} for a scatterer of thickness 4.5 mm and photons from ^{99m}Tc. For a 5 MBq source the expected event rate is therefore 8 kHz, but during the readout, the event rate is saturated at 50 Hz, the saturation determined by the readout electronics. The prototype readout should be drastically improved to confirm the predicted efficiency. Assuming no degradation related to readout electronics, the following comments are related to optimization of prototype geometry for higher efficiency.

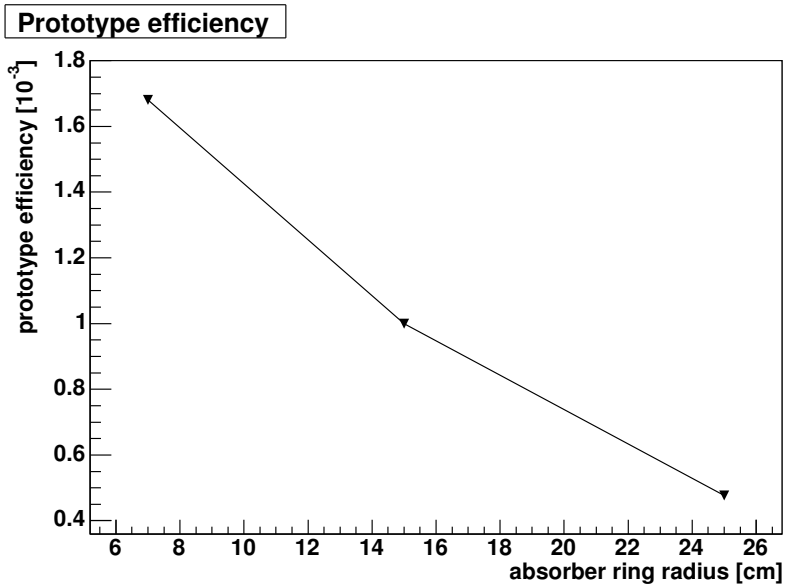

Figure 7.3: Efficiency of a prototype with a total scatterer thickness of 4.5 mm and three SPRINT modules as a function of the distance between the scatterer modules and absorber modules.

The total efficiency of Compton camera would be further increased if more modules would be stacked, with efficiency growing linearly with the scatterer thickness up to 1 cm [LCH$^+$98]. The efficiency is also proportional to the solid angle Ω_1 spanned by the scatterer relative to the source. Increasing the size of the scatterer is another handle of increase the efficiency of Compton camera. Assuming a setup where the same three absorber modules are moved

Table 7.1: Efficiency of the prototype for photons of commonly used radio-tracers ^{99m}Tc (140.5 keV), ^{111m}I (250 keV) and a positron source.

photon energy [keV]	efficiency of the scatterer [4.5 mm] + geometry [‰]	efficiency of the absorber [%]	total efficiency [‰]
140.5	1.7	88	1.5
250	1.4	60	0.83
511	1.0	10	0.1

further from the source to increase the spatial resolution and optimal electronic readout, the efficiency is halved for a doubled (d=15 cm) distance between the scatterer and the absorber, or quartered if the absorbers are placed d=25 cm away from the scatterer The hypothetical efficiency would hence be maintained by strategic placement of twice (four-times) the number of absorber modules at the specified distance.

The hypothetical performance of the prototype with improved electronic when used with higher energies of the initial photon is given in Table 7.1. The major efficiency loss at those energies is due to the low stopping power of the absorber.

7.1.3 Comparison to Anger camera

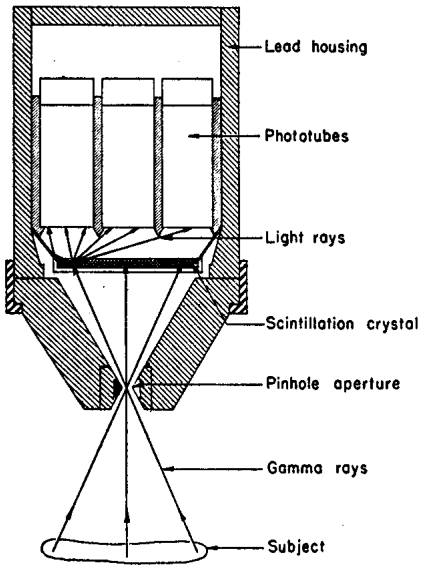

FIG. 1. Sectional drawing of scintillation camera.

Figure 7.4: A schematic drawing of an Anger camera [Ang58].

Gamma cameras for clinical use are based on the Anger camera principle, described by Hal Anger [Ang58] in the 1950-s. Figure 7.4 shows a schematic of the basic prototype: a mechanical collimator of lead shields the sensitive part, a scintillator - photomultiplier tube assembly, and only photons coming through the aperture are detected. The distribution of interactions on the sensitive plane is proportional to a two-dimensional projection of the spatial distribution of photon sources on the sensitive surface. A three-dimensional image is obtained by rotation of camera around the object.

Both efficiency and spatial resolution of the device depend on the aperture size. A large aperture increases efficiency at the expense of spatial resolution. The opposite is true for a small aperture, where higher spatial resolution is achieved[1] at the expense of lower efficiency, causing the already mentioned resolution-efficiency trade-off, characteristic for mechanically collimated imaging. This trade-off causes operating devices to assume either a high-efficiency (HE) or high-resolution (HR) modality: in HE mode the efficiency is optimized while maintaining a reasonable image resolution, and in HR mode, resolution is optimized. Comparison of performance parameters of both modalities in the state-of-the-art Anger cameras is given in Table 7.2. For comparison, values for Anger camera optimized for imaging of small animals is shown. This camera works in extreme proximity of the imaged objects, allowing it exhibit extreme spatial resolution and efficiency.

Table 7.2: Comparison of performance parameters of reported Anger cameras and Compton camera prototype at imaging of photons from ^{99m}Tc.

Camera type		Spatial resolution [mm FWHM]	Efficiency [‰]
Siemens Orbiter[2]	low-energy HR	5 [GFD$^+$96]	$\approx$ 0.05
	HE	11 [GFD$^+$96]	0.1-0.2
fastSPECT [LKS$^+$02]		1.5	0.4
Compton camera prototype		10	1.5 (0.04)

Comparing our simple prototype to elaborate devices presented in Table 7.2 seems like a futile task. The Anger camera principle is present for 50 years and many solutions were found to circumvent the draw-backs of the basic principle. Compton camera, however, is a new imaging method with practically no experience, and current prototype is aimed at confirming its principles rather than excelling in performance. The fact that parameters are comparable (Table 7.2) for a simple prototype with geometry and readout far from optimized and a very simple image reconstruction technique, makes Compton camera a very popular tool for the future. When radio-tracers with photon energies higher than 140.5 keV (used for comparison in Table 7.2) are used, performance of Compton camera improves, and performance of Anger camera degrades. Therefore Compton camera offers a whole new

[1] The spatial resolution of an Anger camera is saturated at the inherent resolution of the sensitive part.

dimension for SPECT imaging – higher photon energies – which Anger camera is not able to explore.

A further note should be given to comparison of efficiency of Compton and Anger camera. Conical ambiguity of Compton camera is overcome by an intersection of several events, and the information loss is quantified using a uniform Cramer-Rao bound, which is independent of the imaging mode. The results is a decoding penalty, which is a ratio of image variances calculated from Compton data (using EM/LML[3] algorithm for example) and Anger camera data. The decoding penalty depends on the location and extent of the object: for a uniform disk of ^{99m}Tc with 7.5 cm diameter the penalty is about 40, for a 15 cm disk of ^{99m}Tc it increases to 90 and for a 7.5 cm disk of ^{131}I (E_γ=364.5 keV) it is reduced to 1, all for the same imaging geometry. The decoding penalty has to be balanced by the sensitivity increase for Compton camera to break even with a mechanically collimated device.

7.2 Prostate probe: A possible Compton camera application

The evaluation of the prototype showed that the performance of the Compton camera is optimized when the separation between the source and the scatterer is decreased and the distance between the scatterer and the absorber increased. Those facts, combined with the robustness of silicon sensor lead to idea of a prostate probe [Zha04].

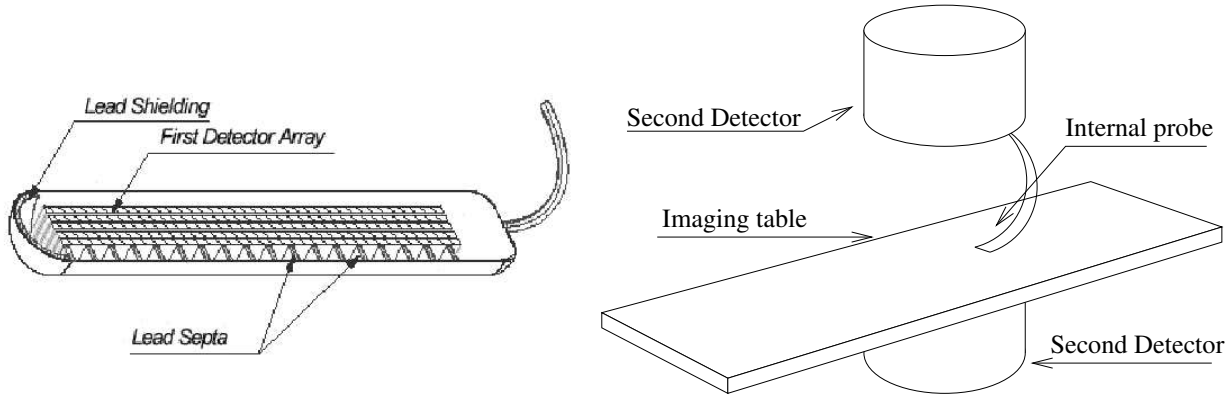

Figure 7.5: An image of the proposed prostate probe. Left: Scatterer or first detector array, consisting of densely packed layers of silicon pad sensors. Right: Absorber or secondary detector surrounding the bed for the patient.

Prostate cancer is the second most common cancer in men and one out of six males will develop it. The current diagnostics is aimed at detecting protrusions, either with X-ray or

[3]Expectation maximization/list-mode maximum likelihood presented in Appendix B

ultrasound. Currently, SPECT imaging is only used to trace the spreading of the disease to other organs [KWM+98, HBO+98], which is already a critical phase in cancer development. Present cameras placed 10 cm of further from the prostate do not exhibit required spatial resolution to determine the extent and location of the primary tumor. The prostate probe would be hence a pioneer in the field, exploiting both a near-field view of the prostate and a resulting high spatial resolution. A proposed probe could be composed as shown in Figure 7.5: a densely packed array of silicon pad sensors with thickness of 10 mm to be inserted intra-rectally, close to the prostate, and an absorber ring with a radius of 25 cm surrounds the body of the patient and detects the scattered photons. The radio-active agent used would be a ^{111m}In labeled antibody specific to prostate cancer, which is already used for present prostate-cancer related SPECT imaging.

The device is currently being modeled using Monte-Carlo studies. An elaborate computer phantom simulating the human body is used along with determined uptakes of radiation in other organs of the patient. The simulation shows the device efficiency equal to 1.8 ‰ and resolution of 2.58 mm FWHM. The prostate probe with such a performance would be able to detect lesions with a 5 mm diameter and radio-tracer related activity 5-times larger than the activity of the background, allowing for early detection of the disease and a precise monitoring of its treatment. For a comparison, the best resolution obtained by a collimated scintillator ring would be 11 mm FWHM in high resolution mode and 15 mm in high efficiency mode, where estimated efficiency equals to 0.1 ‰.

Chapter 8

Summary

SPECT is a diagnostic method where spatial resolution of disease specific substances, labeled with γ-ray sources is imaged. Traditional SPECT detectors, Anger cameras are limited in their performance, since they exhibit resolution-efficiency trade-off inherent to mechanically collimated cameras. Compton camera is a novel imaging technique, which uses kinematics of Compton scattering instead of mechanical collimator removing the coupling between efficiency and resolution. The thesis presents the development of a Compton camera prototype built in order to test the viability of the proposed approach.

Compton camera consists of two sub-detectors: the scatterer where Compton scattering of initial photons is observed, and the absorber, where scattered photons are detected. In Compton scattering a Compton electron is produced, and kinematics relates the kinetic energy of the electron to the photon scattering angle. The scatterer measures the energy of the Compton electron, and impact points in scatterer and absorber determine the scattered photon direction. All possible directions of the initial photon form a cone, with the axis along the scattered photon direction, the opening angle equal to the scattering angle and the apex fixed on the interaction point in the scatterer. Intersection of cones for multiple events reproduces the position of the source.

The spatial resolution of the device is driven by three contributions: inherent resolution from Doppler broadening, limited energy resolution of the scatterer and geometrical contribution related to spatial resolution of sub-detectors. In an optimized imager the inherent resolution is dominant and contributions of energy resolution of the scatterer and setup layout combined with spatial resolution of sub-detectors should be smaller.

The scatterer module of the developed prototype consists of custom developed silicon pad sensors, coupled to VATAGP3, an off-the-shelf front-end ASIC. Silicon exhibits one of the lowest Doppler broadenings in detection materials (80 mrad at the scattering angle of $\pi/2$) and silicon pad sensors provide suitable energy resolution at room temperature and (more than) adequate spatial resolution. A pad dimension of 1.4 mm was chosen to confine the charge produced by a Compton electron to a single pad, minimizing the dominating contri-

bution of front-end electronics noise on energy resolution. Sensors with thicknesses of up to 1 mm were used. Data were collected using a custom developed data acquisition system, partially based on VME technology. The excellent measured energy resolution of 1.2 keV on 0.5 mm and 1.5 keV on 1 mm thick sensors gave a contribution to resolution approximately equal to Doppler broadening for ^{99m}Tc photons. The trigger signal of the scatterer, required for correlation of interactions in the scatterer and the absorber, was measured to have a timing resolution of 150 ns FWHM.

The absorber of the setup was taken from the existing SPRINT II prototype, fitting nicely to requirements of the Compton camera. The calibration of the absorber gave a spatial resolution of 4 mm FWHM and timing resolution of 22 ns FWHM.

The prototype was assembled on a custom designed frame. Five scatterer modules with a total thickness of 4.5 mm were surrounded by three absorber modules forming an incomplete ring with an average separation of 7 cm between scatterer and absorber modules. A ^{99m}Tc source was placed on axis of the ring, approximately 4 cm away from the first scatterer module. For such placement of the source, the predicted efficiency of the setup was 1.6×10^{-3} and the geometrical contribution to spatial resolution was approximately equal to the contribution from Doppler broadening. The timing resolution of the prototype was dominated by the resolution of the scatterer and a timing window of 200 ns was used. Data from a 5 MBq source were collected with a maximal event readout frequency of 50 Hz, saturated due to the readout electronics.

A simple back-projection algorithm was used to reconstruct the position of the point source. The resolution of the reconstructed image matched the predicted resolution. For a limited number of events within the optimal scattering angle range, a spatial resolution of 8 mm FWHM was obtained, or angular resolution of 170 mrad FWHM, comparable to the performance of the state-of-the art Anger cameras. The estimated efficiency of the prototype was an order of magnitude larger than efficiency of a typical Anger camera, which would compensate for the conical ambiguity of Compton imaging reconstruction.

The performance of the simple prototype with a crude reconstruction algorithm was comparable to the performance of the state-of-the art Anger cameras, which shows a great potential for more elaborate Compton camera imagers. A proposed application, the prostate probe would consist of a densely packed scatterer, inserted intra-rectally with a near-field view of the prostate, combined with an absorber ring surrounding the patient. According to the simulations, the probe would exhibits spatial resolution and efficiency superiror to the present detectors for higher energy (^{111m}In, 245.5 keV) radio-tracers specific to prostate cancer. Thus the prostate probe should be capable of determining the location and extent of the primary cancer, a task present SPECT is not capable of, allowing for early treatment and precise monitoring of the disease.

Poglavje 9

Povzetek doktorskega dela

9.1 Uvod

Pri medicinski preiskavi SPECT[1] substanco, značilno za dano bolezen ali fiziološki proces, označijo s sevalcem žarkov γ. Porazdelitev izvorov žarkov ustreza razporeditvi substance, kar omogoča spremljanje njene presnove in akumulacij, to pa predstavlja pomemben korak k natančnejšemu diagnosticiranju bolezni. Tipične cne energije izsevanih fotonov so 140.5 keV (izvor ^{99m}Tc), 250 keV (^{111m}In) in 511 keV (^{11}C, ^{15}O, ^{18}F). Tradicionalni detektorji za SPECT so Angerjeve kamere, ki smeri, s katerih lahko fotoni zadenejo občutljiv del detektorja, omejijo s svinčenimi zaslonkami. S to metodo je neločljivo povezana izmenjava med izkoristkom in prostorsko ločljivostjo naprave: primerno ločljivost dosežemo, ko večino fotonov (99,99%) absorbira svinčeno ohišje. V izogib izmenjavi se razvijajo drugačne metode slikanja. Ena takih je comptonska kamera, ki zaslonke nadomesti s tako imenovanim sipalnim detektorjem ali sipalcem. Kinematika Comptonovega pojava fotonov v sipalcu nam poda smer vpadnea fotona. Namen doktorata je bil sestaviti prototip comptonske kamere s posebej za to razvitimi krajevno-ločljivimi silicijevimi detektorji in preveriti njeno uporabnost za slikanje z metodo SPECT.

Comptonov pojav (slika 9.1) je trk fotona z elektronom v snovi in ga izbije iz atoma. Nastane Comptonov elektron, katerega kinetična energija E_e je zaradi ohranitve energije in gibalne količine pri sipanju povezana s sipalnim kotom fotona θ:

$$\sin^2 \frac{\theta}{2} = \frac{m_e c^2 E_e}{2E_\gamma (E_\gamma - E_e)}, \tag{9.1}$$

z E_γ energijo vpadnega fotona, m_e mirovno maso elektrona in c hitrostjo svetlobe v vakuumu. Za merjenje Comptonovega pojava je comptonska kamera sestavljena iz dveh delov:

[1] angl. Single Photon Emission Computed Tomography

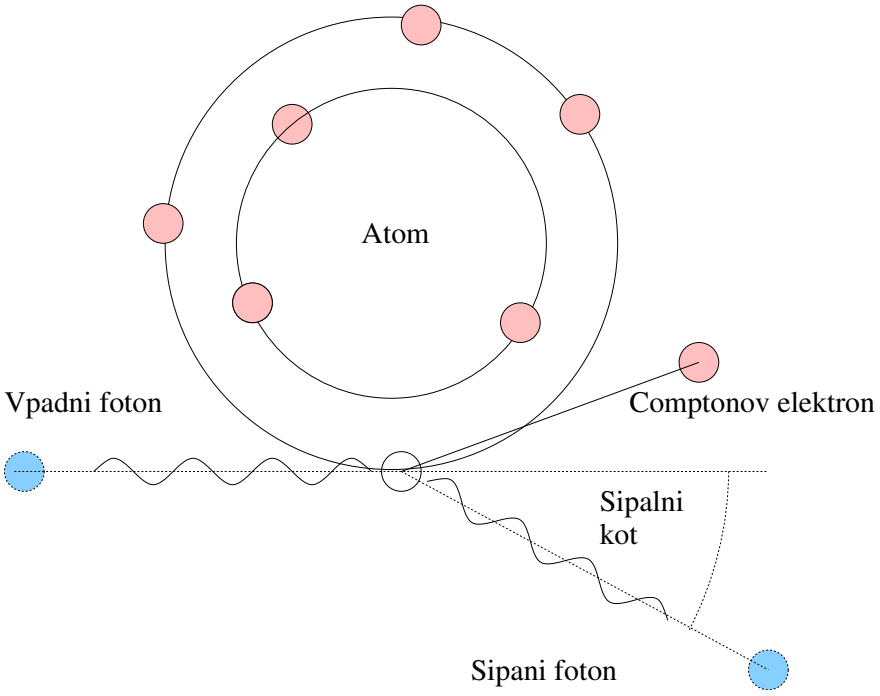

Slika 9.1. Ilustracija Comptonovega pojava.

v sipalcu se izsevani foton sipa – merimo točko interakcije in energijo Comptonovega elektrona; zadetek sipanega fotona v absorberju pa nam določi njegovo smer po sipanju. Pri danem dogodku smeri vpadnega fotona tvorijo stožec z osjo enako smeri sipanega fotona, vrhom pri interakcijski točki v sipalcu in vršnim kotom enakim sipalnemu kotu. Slika 9.2 kaže nastale stožce in kako lahko iz presečišč množice stožcev, ki ustrezajo zaporednim dogodkom, določimo lego sevalcev.

Energije Comptonovih elektronov so zvezno porazdeljene do maksimalne energije:

$$E_e^{\max} = \frac{1}{1 + \frac{m_e c^2}{2E_\gamma}} E_\gamma, \tag{9.2}$$

ki ji rečemo Comptonov rob. Pri energijah fotonov pri preiskavi SPECT je poleg Comptonovega pojava edina preostala interakcija fotoefekt. Pri fotoefektu se vpadni foton povsem absorbira v snovi, namesto Comptonovega elektrona pa dobimo foto-elektron, ki ima kinetično energijo enako energiji vpadnega fotona.

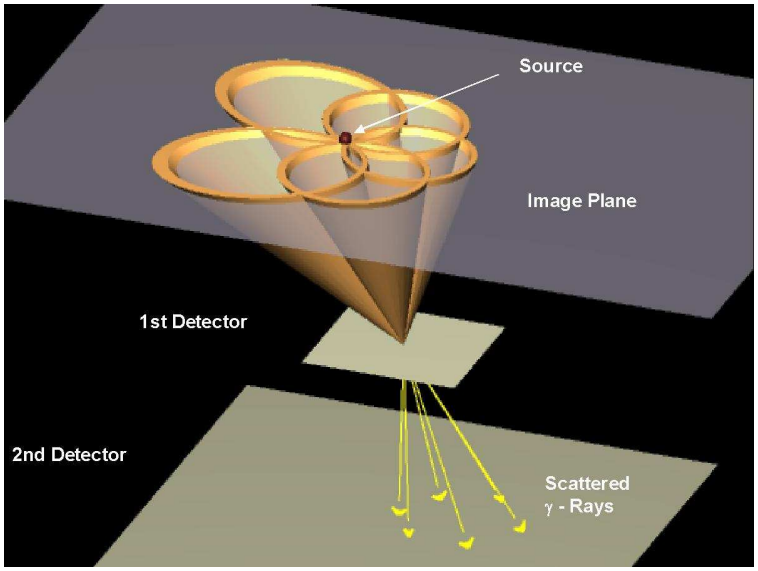

Slika 9.2. Shematičen prikaz rekonstrukcije izvora pri comptonski kameri. Vsakemu dogodku ustreza stožec možnih smeri vpadnega fotona, njihovo presečišče pa poda lego sevalca (Source).

9.2 Sipalec

Silicijev sipalec prototipa je sestavljen iz modulov, kakršen je prikazan na sliki 9.3. Na PCB hibrid je pritrjen silicijev detektor z 256 blazinicami kvadratne oblike s stranico 1,4 mm, razporejenimi v mreži oblike 32×8. Blazinice so pravzaprav diode, ki zbirajo naboj, nastal pri ionizaciji Comptonskega ali foto-elektrona. Stranica blazinice je dovolj velika, da v večini dogodkov naboj zbere le ena dioda, kar pomembno prispeva k dobri energijski ločljivosti modula. V 1 mm debelem detektorju je verjetnost za Comptonsko sipanje med 2 % (energija fotonov 511 keV) do 3 % (140,5 keV), v prav tako uporabljenem pol tanjšem detektorju pa ravno tolikokrat manjša. Signale z detektorja obdeluje par VATAGP3[2] čipov s po 128 bralnimi kanali, ki ob interakciji v pripadajočih kanalih generirata prožilni signal in zadržita velikosti signala v vsakem od kanalov.

Za komunikacijo s čipi je bilo potrebno razviti bralni sistem, ki delno temelji na VME standardu. Ob prožilnem signalu sistem prenese vrednosti signalov vseh (ali zadetega dela) kanalov s čipa na računalnik, ta pa služi kot orodje za obdelavo in trajno shranjevanje podatkov. Algoritem za obdelavo surovih podatkov še odšteje ničelni nivo vsakega kanala, izračuna in odšteje skupen premik kanalov v vsakem dogodku in poravna ojačanje po celem čipu oziroma detektorju.

Foto-elektroni imajo energijo enako vpadnim elektronom in so idealna sonda za določanje

[2]IDEAS A.S.A, `http://www.ideas.no`

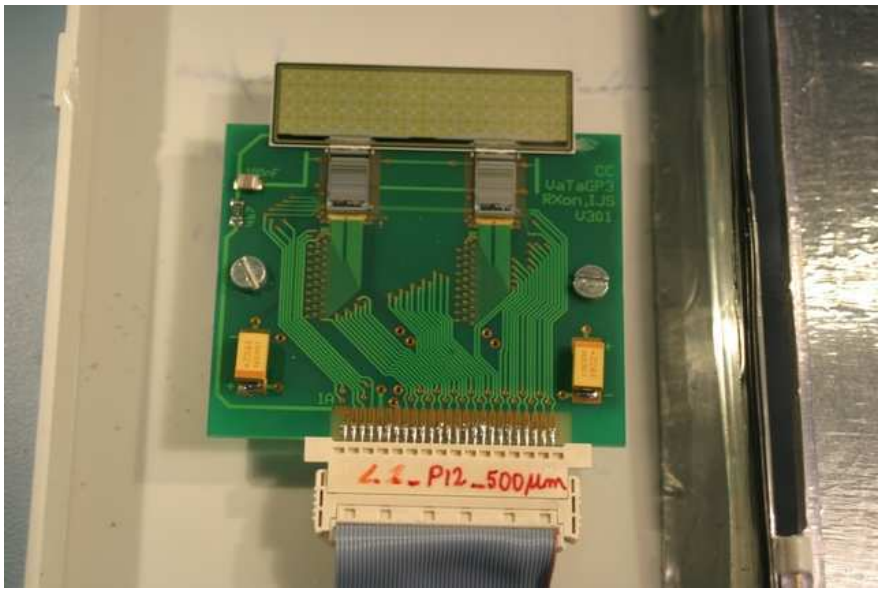

Slika 9.3. Fotografija modula sipalca.

energijske ločljivosti modula. Za preizkus smo izbrali izvor ^{241}Am, ki seva fotone energije 59,5 keV. Energijsko ločljivost izmerimo kot širino porazdelitve izmerjenih energij foto-elektronov. Za modul z 0,5 mm debelim senzorjem je spekter prikazan na Sliki 9.4a in širina porazdelitve na polovični širini vrha (FWHM) pri 59,5 keV znaša 1,2 keV, za modul z 1 mm debelim senzorjem pa smo izmerili energijsko ločljivost 1,4 keV FWHM, (slika 9.4b). Jasni vrhovi v obeh izmerjenih spektrih so del emisijskega procesa ^{241}Amali pa ustrezajo značilnim rentgenskim žarkom srebra (Ag), prisotnega na hibridu.

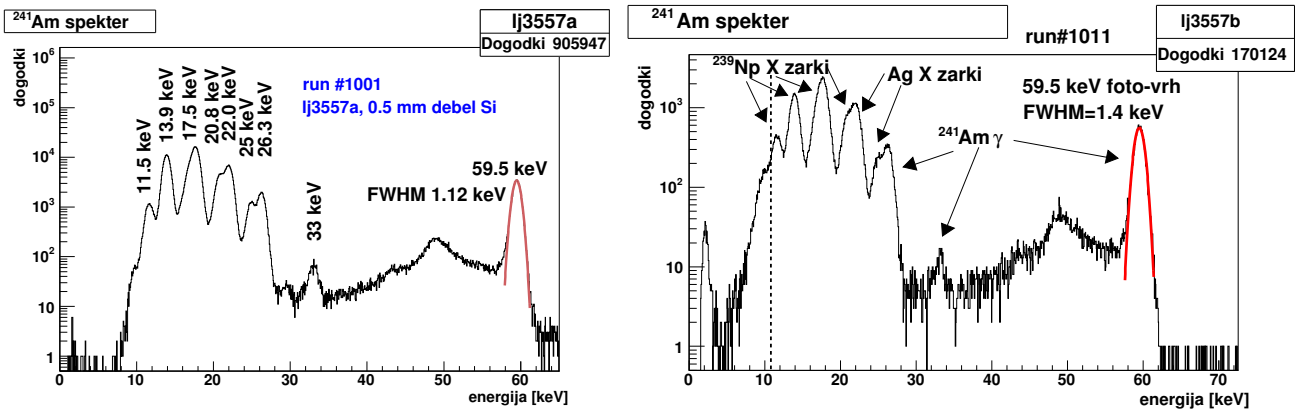

(a) (b)

Slika 9.4. Spekter ^{241}Amposnet na modulu z (a) 0.5 mm in (b) 1 mm debelim silicijevim detektorjem.

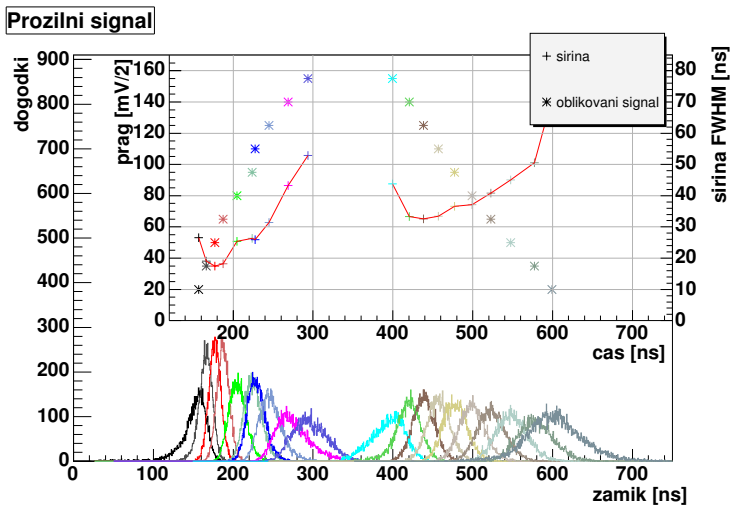

Slika 9.5. Časovna ločljivost prožilnega signala. Glavna os: Serija 20-ih histogramov, od katerih vsak kaže porazdelitev zamika med trenutkom vbrizga naboja in trenutkom proženja čipa za dano razmerje med (stalno) količino naboja in (spreminjajočim se) pragom. Vstavljeni graf: * - Odvisnost srednjih vrednosti porazdelitev zamika od nastavljenega praga; odvisnost sovpada z obliko signala namenjenega proženju. + - Širina porazdelitve, ki ustreza dani srednji vrednosti.

Signal iz detektorja za potrebe proženja čip VATAGP3 oblikuje z oblikovnim časom 150 ns. Oblikovni čas je izbran tako, da presega čas zbiranja naboja v detektorju. V trenutku, ko oblikovani signal preseže prag, čip odda prožilni signal. Čas proženja je odvisen od razmerja r med signalom v detektorju in pragom ter od šuma elektronike. Slika 9.5 kaže obe odvisnosti. Vsak histogram na osi glavnega grafa kaže porazdelitev zamikov pri izbranem r, njihova širina pa je posledica elektronskega šuma. Porazdelitve so izmerjene pri vbrizgu konstantne količine naboja neposredno na vhod bralnega kanala. Centri porazdelitev opišejo obliko vhodnega signala, ki je prikazan skupaj z širinami na vstavljenem grafu. Ker je spekter Comptonovih elektronov zvezen, je časovna ločljivost podana z intervalom, ki ga pokrijejo histogrami (za naraščajoči del krivulje), katerega dolžina je približno enaka oblikovnemu času, torej 150 ns.

9.3 Absorber

Za absorber smo uporabili detektorske module iz obroča SPRINT II (slika 9.6). Posamezni modul sestavljajo: na dnu NaI(Tl) scintilator, narezan v 3 mm debele, 15 cm dolge in 1,28 cm debele palice, v sredini nabor 20 fotopomnoževalk (PMT) in na vrhu tri plasti elektronskega vezja, ki nadzoruje napetosti na pomnoževalkah in oblikuje ter sešteva dobljene signale. Eden od izhodnih signalov z elektronskega vezja je energijska vsota, signal sorazmeren vsoti

analognih signalov vseh pomnoževalk. Ta je preko diskriminatorja konstantnega deleža (angl. constant-fraction discriminator, CFD) generiral prožilni signal. Ob prožilnem signalu smo amplitude signalov vseh 20 foto-pomonoževalk digitalizirali na VME ADC kartici[3] ter prenesli in shranili na osebni računalnik. Verjetnost za fotoefekt sipanega fotona v 1.28 cm debelem absorberju je od 10 % (fotoni z energijo 511 keV) do 90 % (140,5 keV).

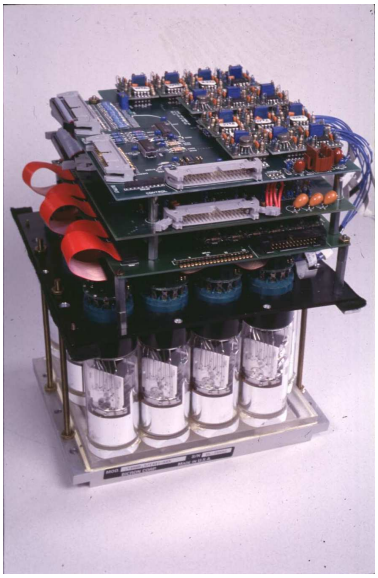

Slika 9.6. Fotografija enega od modulov, uporabljenih za absorber.

Pred uporabo v prototipu smo module umerili in določili njihovo krajevno, časovno in energijsko ločljivost. Pomnoževalke se napajajo iz skupnega delilca napetosti, zato smo njihovo ojačanje v obdelavi podatkov poravnali z naborom popravkov g_i. Nato smo določili energijo E_a fotona zaznanega v absorberju kot uteženo vsoto energij E_i, zbranih v posamezni (i) od dvajsetih (N_{PM}=20) PMT:

$$E_a = \frac{1}{\sum_{i=1}^{N_{PM}} g_i} \sum_{i=1}^{N_{PM}} g_i E_i. \tag{9.3}$$

Slika 9.7 kaže fotoabsorpcijski spekter fotonov iz ^{57}Coz energijo 122 keV in 136 keV. Ločljivost 18 keV ne dovoljuje ločitve obeh emisijskih črt, a zadošča zahtevam za Comptonsko kamero, saj omogoča ločevanje pravih dogodkov od ozadja.

Za določanje točke interakcije smo uporabili preprosto centroidno metodo:

$$\vec{\mathbf{r_a}} = \frac{1}{\sum_{i=1}^{N_{PM}} g_i E_i} \sum_{i=1}^{N_{PM}} g_i E_i \vec{\mathbf{r_i}}, \tag{9.4}$$

[3]mod. V 785, CAEN, Viareggio, Italija, `http:/www.caen.it`

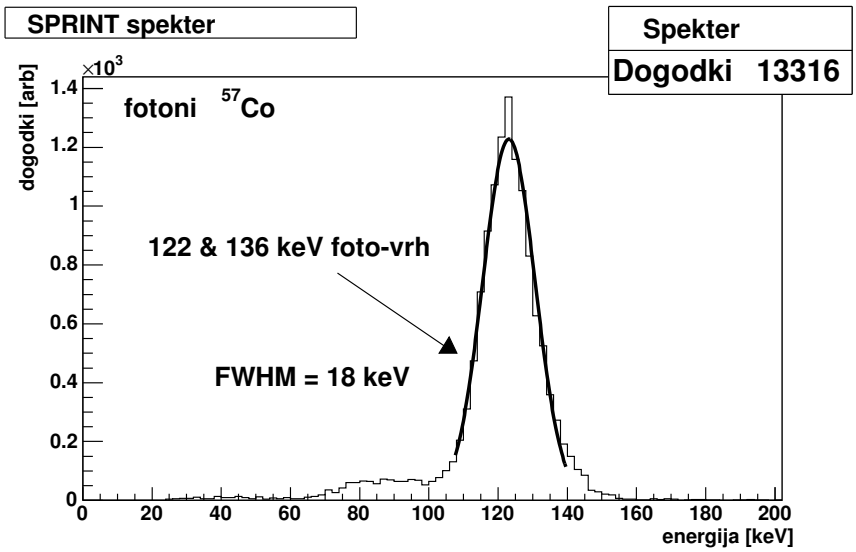

Slika 9.7. Spekter fotonov iz ^{57}Co(122 keV, 136 keV) zaznanih v modulu absorberja, z navedeno energijsko ločljivostjo določeno s prileganjem Gaussove porazdelitve na izmerjeni spekter.

kjer $\vec{\mathbf{r}_i}$ določajo center i-te pomnoževalke. Dobljeno popačitev slike smo popravili s podatki o točnih legah izvorov med kalibracijo.

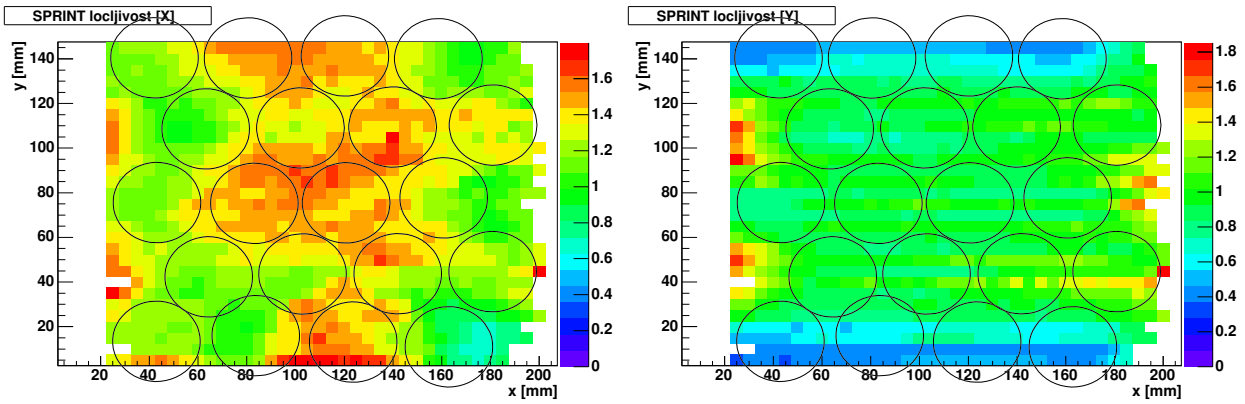

(a) (b)

Slika 9.8. Krajevna ločljivost SPRINT modula (varianca(!) porazdelitve zadetkov) po površini modula. Slika (a) predstavlja ločljivost v smeri x, vzdolž palic, in slika (b) v smeri y, prečno na palice NaI(Tl) kristala.

Odvisnost krajevne ločljivosti od točke interakcije podaja slika 9.8, in sicer del (a) podaja ločljivost vzdolž palic in del (b) ločljivost prečno na palice. Povprečna ločljivost izražena v FWHM porazdelitve zadetkov znaša 4 mm preko vsega detektorja.

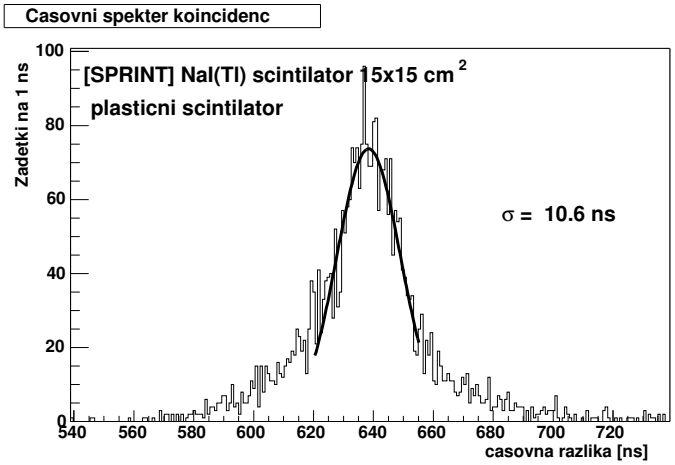

Slika 9.9. Časovna razlike med časom zadetka fotona v referenčnem sistemu – plastičnem scintilatorju, sklopljenem s fotopomnoževalko – in trenutkom proženja SPRINT modula, za par fotonov iz pozitronskega sevalca ^{22}Na.

Časovno ločljivost modula smo preverili s pozitronskim izvorom ^{22}Na, ki generira par fotonov letečih v nasprotnih smereh. Enega od fotonov zaznamo v plastičnem scintilatorju povezanim s fotopomnoževalko, katerega signal z ločljivostjo 100 ps nam služi kot časovna referenca. Drugi foton zaznamo v modulu in čas proženja primerjamo z referenco. Širino dobljene porazdelitve na Sliki 9.9 smo določili s prileganjem Gaussove porazdelitve na 22 ns FWHM.

9.4 Prototip

Za prototip smo izdelali ogrodje, ki ga kaže slika 9.10. Na Sliki 9.10b, ki prikazuje odprt prototip, vidimo v sredini ogrodja vstavljen nosilec modulov sipalca. V nosilec je bilo vstavljenih vseh 5 možnih modulov z razmakom med moduli 6 mm in s skupno debelino silicija enako 4,5 mm. Trije SPRINT moduli so sestavljajali polobroč na srednji razdalji 7 cm od sipalca. Izvor ^{99m}Tcje bil postavljen na premično mizico na povprečni razdalji 5 cm od modulov sipalca, približno v osi obroča. Bralni sistem je bil sestavljen iz sistemov obeh poddetektorjev, na ravni VME kartic pa smo dogodek sestavili iz podatkov sipalca in absorberja.

Ločljivost comptonske kamere je določena z njeno kotno ločljivostjo; krajevna ločljivost je produkt kotne ločljivosti in znane razdalje med virom in sipalcem. Kotna ločljivost je sestavljena iz treh prispevkov: neizogibne napake zaradi Dopplerjeve razširitve, energijske ločljivosti sipalca in geometrijskega prispevka, povezanega s krajevnimi ločljivostmi obeh poddetektorjev in njuno razpostavitvijo. V optimiziranem prototipu bo največji prispevek na račun neizogibne razširitve, medtem ko bosta preostala prispevka manjša. Razmerje med zgornjimi prispevki za naš prototip in izvor ^{99m}Tcpostavljen v os obroča kaže slika 9.11. Skupna

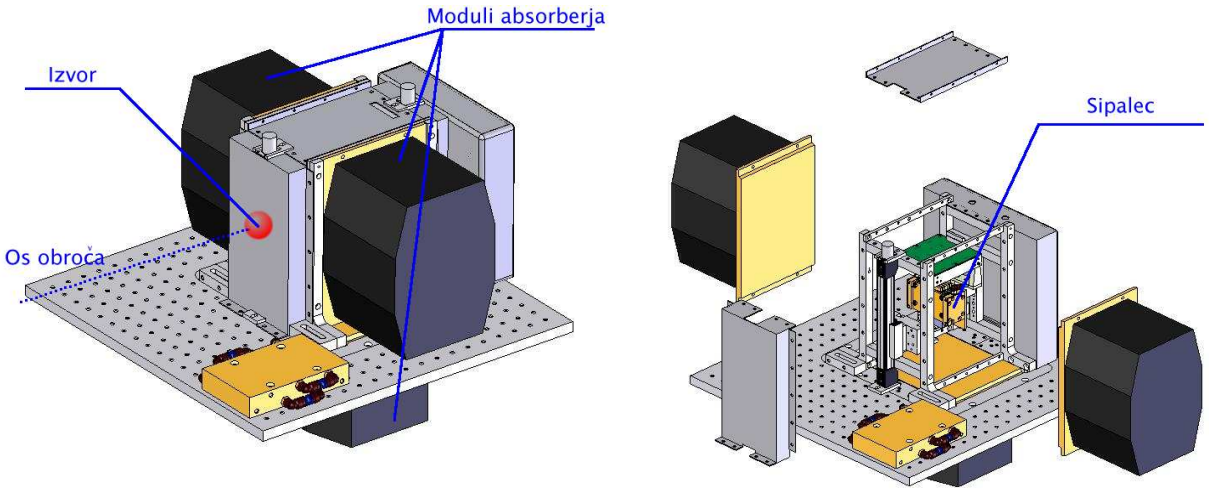

Slika 9.10. Shema prototipa comptonske kamere : a – Sestavljeni prototip: trije (črni) SPRINT moduli absorberja tvorijo nepopolni obroč okrog zakritih sipalcev. b – Razstavljeni prototip s sipalcem v središču obroča.

ločljivost ima širok minimum okrog sipalnega kota 1 radian, kjer sta prispevka geometrije in krajevne ločljivosti približno enaka Dopplerjevi razširitvi, ki znaša 60 mrad, skupna ločljivost pa je 120 mrad. Ločljivost comptonske kamere se izboljšuje z naraščajočo energijo fotonov, ki jih seva izvor: pri 250 keV je skupna ločljivost 70 mrad in pri 511 keV le še 60 mrad, predvsem na račun geometrijskega prispevka, ki ni odvisen od energije.

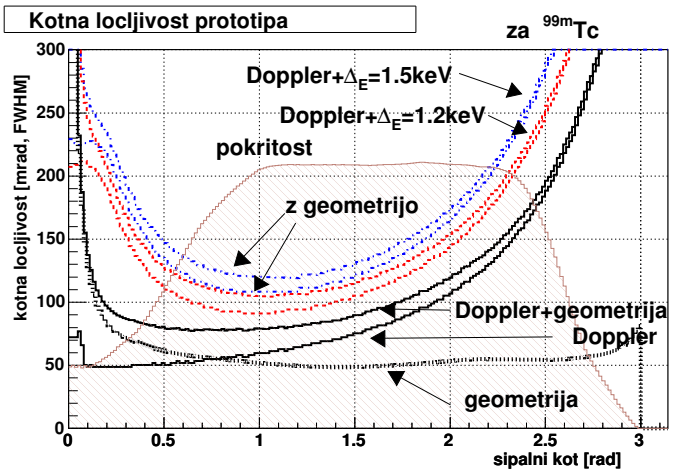

Slika 9.11. Kotna ločljivost prototipa v odvisnosti od sipalnega kota. Skupna ločljivost za 0,5 mm (1,2 keV) in 1 mm (1,5 keV) debele detektorje sipalca in prispevki Dopplerjeve razširitve, geometrije in kombinacije obeh prikazani posebej. Odvisnost za ^{99m}Tcizvor na osi obroča absorberjev, 5 cm od modulov sipalca.

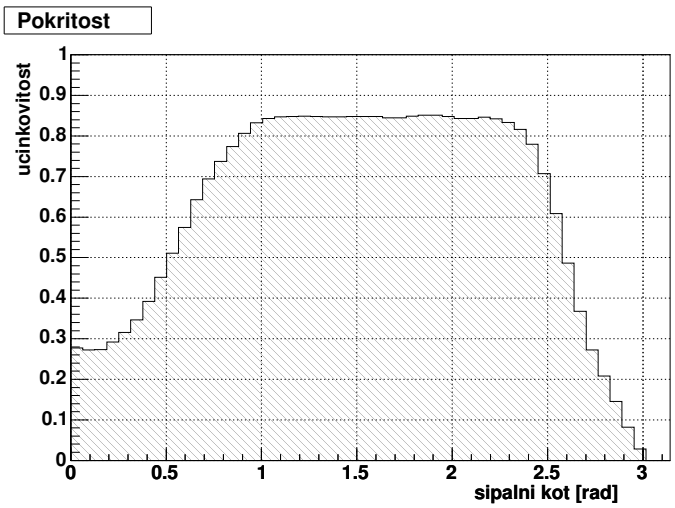

Slika 9.12. Geometrijski faktor ki kaže pokritost sipalnih kotov z absorberjem. Za izvor na osi, 5 cm od srednjega detektorja.

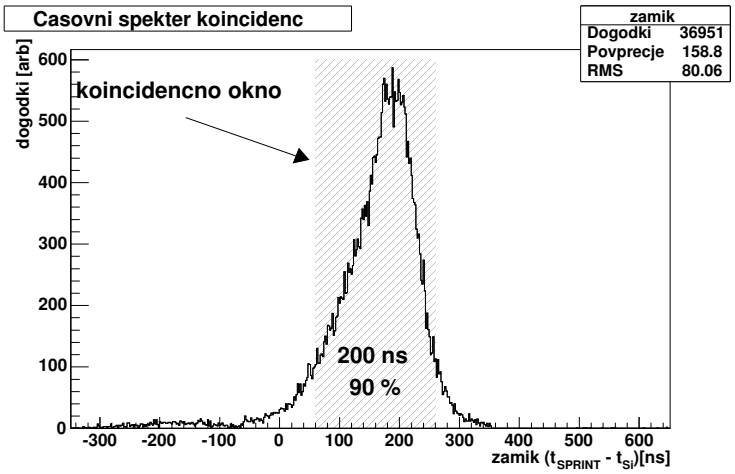

Slika 9.13. Porazdelitev zamika med prožilnim signalom v sipalcu in absorberju. Prikazano optimizirano koincidenčno okno ǒdolgo 200 ns zbere 90 % dogodkov iz vrha.

Izkoristek kamere je povezan z verjetnostma za interakcijo v sipalcu in absorberju ter z geometrijskim faktorjem, sorazmernim s pokritostjo sipalnih kotov absorberja. Odvisnost geometrijskega faktorja od sipalnega kota za izvor na osi obroča za naš prototip podaja slika 9.12. Z upoštevanjem prostorskega kota sipalca glede na povprečno 5 cm oddaljen izvor in verjetnosti za interakcijo v posameznih poddetektorjih je učinkovitost priprave $1{,}6\times10^{-3}$, oziroma en zaznani foton na 600 izsevanih. Pri preizkusu je bil uporabljen $^{99\mathrm{m}}$Tcizvor z aktivnostjo 5 MBq in v skladu z napovedano učinkovitostjo bi pričakovali 8000 zaznanih dogodkov na sekundo, vendar je bila frekvenca zajemanja dogodkov zasičena pri 50 Hz

zaradi bralne elektronike.

Časovna usklajenost obeh detektorjev je prikazana na Sliki 9.13, ki kaže porazdelitev zamika med prožilnima signaloma v sipalcu in absorberju z jasnim koincidenčnim vrhom. K širini vrha najbolj prispeva slaba energijska ločljivost sipalca. Koincidenčno okno široko 200 ns zajame 90 % dogodkov iz vrha. Med preostalimi 10 % so tudi dogodki z nizko energijo Comptonovih elektronov, ki imajo sicer dobro kotno ločljivost, a jih zaradi slabe časovne ločljivosti izločimo s koincidenčnim oknom.

9.5 Rekonstrukcija

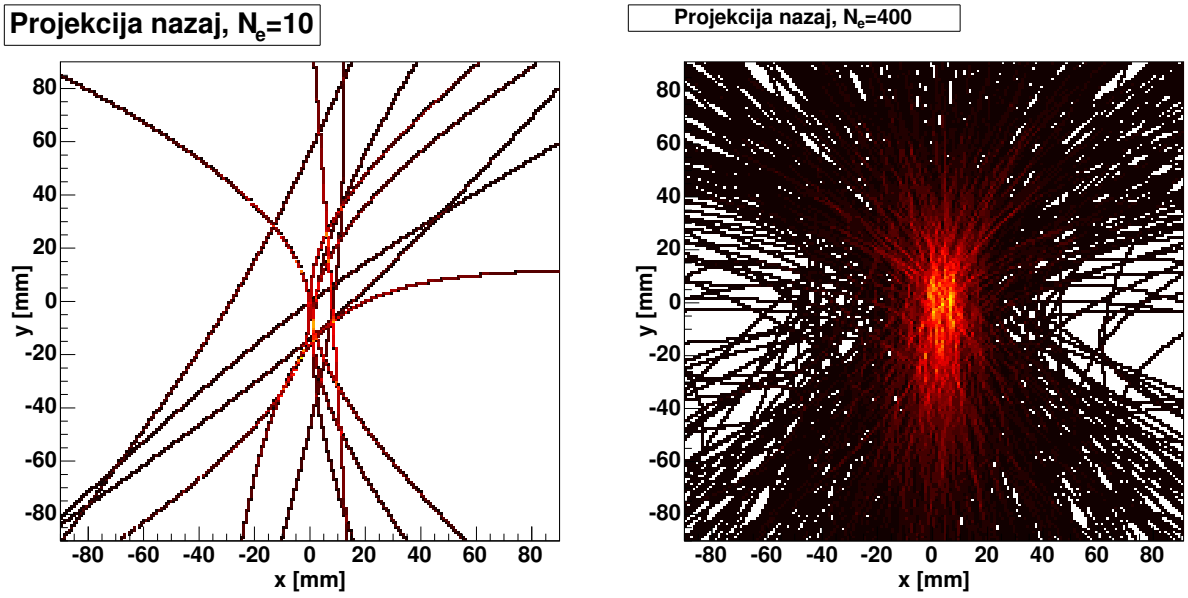

(a) (b)

Slika 9.14. Vmesni koraki pri projekciji nazaj v prostor izvora: a – Prvih N_e=10 dogodkov in b – N_e=400 dogodkov.

Preprosta rekonstrukcija lege izvora je projekcija izmerjenih vrednosti nazaj v prostor izvorov. Za to priredimo vsakemu dogodku stožec možnih smeri vpadnega fotona in točke v prostoru sevalcev utežimo glede na število stožcev na katerih ležijo. Da si olajšamo delo, prostor razdelimo na množico goriščnih ravnin in rekonstrukcijo opravimo na vsaki ravnini posebej. Presečišča ravnine in stožca so elipse[4]. Točke na ravnini, ki so del elipse, utežimo z:

$$w = \frac{1}{c^e}\frac{1}{r_s}\frac{\ell}{\ell^e}, \tag{9.5}$$

[4]Med elipse spadajo tudi krožnice, hiperbole, parabole in premice.

kjer je c^e obseg elipse, r_s razdalja med točko na ravnini in točko interakcije v siliciju in ℓ/ℓ^e delež elipse vsebovan v dani točki.

Vmesne korake pri $N_e = 10$ (a) in N_e= 400 (b) dogodkih kaže slika 9.14, slika 9.15 pa kaže končno rekonstrukcijo po $N_e = 250\ 000$ dogodkih.

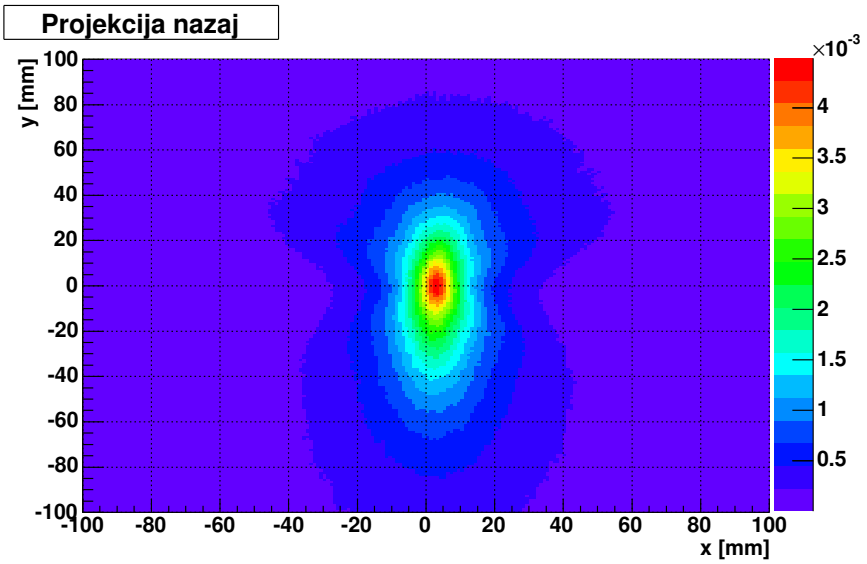

Slika 9.15. Projekcija za 250 000 dogodkov na goriščni ravnini, oddaljeni 4 cm od prednjega sipalca, na približni lokaciji izvora.

Podatke smo zajeli z dvema od treh modulov SPRINT in vsemi petimi moduli sipalca. Manjkajoči modul absorberja slabša ločljivost v navpični (y) smeri, v horizontalni (x) pa je lega izvora dobro določena. S preseki vzdolž osi x in prilagajanjem Gaussove porazdelitve smo določili krajevno, iz znane razlike med goriščno ravnino in sipalcem pa še kotno ločljivost prototipa.

V skladu s predvidevanji se kotna ločljivost izboljšuje, ko izbiramo dogodke s sipalnimi koti blizu minimuma kotne ločljivosti. Primerjavo izmerjene odvisnosti in napovedi kaže slika 9.16; obe se ujemata v okviru natančnosti rekonstrukcijske metode.

Za dogodke z energijo Comptonovega elektrona pod 25 keV dobimo presek s slike 9.17, ki kaže optimalno ločljivost prototipa 8,5 mm FWHM pri oddaljenosti 5 cm ali kotni ločljivosti 170 mrad FWHM.

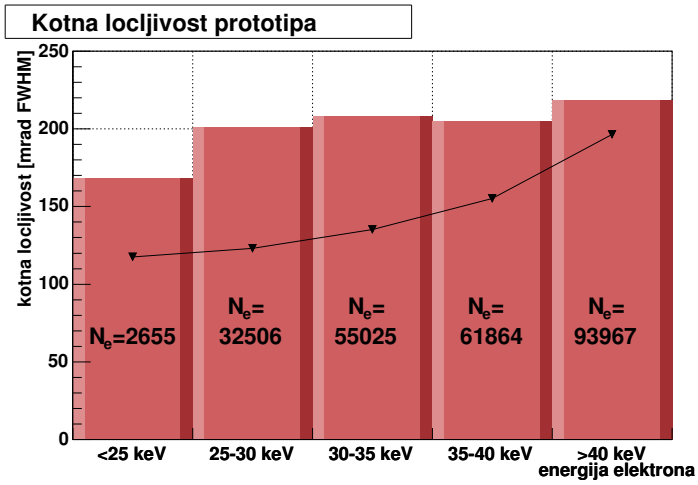

Slika 9.16. Izmerjena kotna ločljivost (stolpci) prototipa v primerjavi z napovedano ločljivostjo (obrnjeni trikotniki) v odvisnosti od energije Comptonskega elektrona (ali sipalnega kota), ki je enaka tisti na sliki 9.11. Vrednosti N_e povedo število dogodkov v vsakem energijskem intervalu.

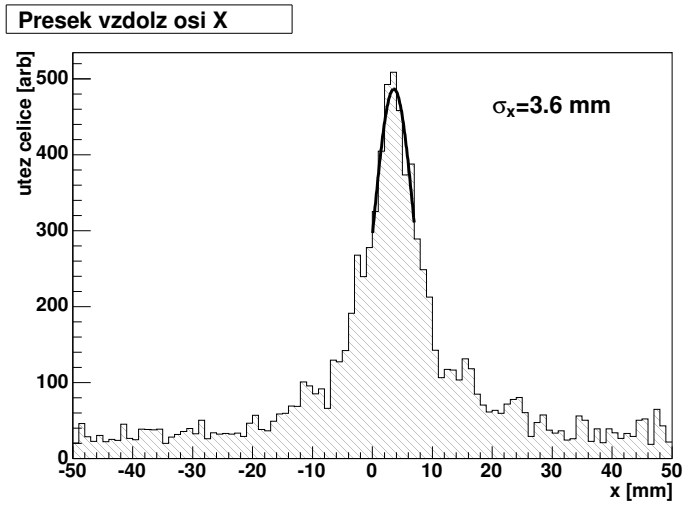

Slika 9.17. Presečišče vzdolž osi x za dogodke z energijo Comptonovega elektrona, manjšo od 25 keV. Ozkemu območju okrog vrha je prilagojena Gaussova porazdelitev, ki da krajevno ločljivost $2,35 \times \sigma_x$=8,5 mm FWHM ali kotno ločljivost 170 mrad pri razdalji sipalca od izvora enaki 5 cm.

9.6 Rezultati in zaključek

Neposredno primerjavo med opisanim prototipom in prejšnjim prototipom comptonske kamere, C-SPRINT-om, onemogoča bistvena razlika v njuni geometriji. Lahko pa izračunamo ločljivost C-SPRINT-u geometrijsko ustreznega prototipa, temelječega na našem prototipu, torej razdalji 25 cm med sipalcem in absorberjem in zajetimi sipalnimi koti med 80° in 110°. Tak hipotetični prototip bi imel ločljivost 100 mrad, kar je velik napredek v primerjavi s 150 mrad, ki jih daje C-SPRINT; izboljšava gre predvsem na račun izboljšane energijske ločljivosti sipalca.

Preprost prototip s preprosto rekonstruckijsko metodo je primerljiv z utečenimi Angerjevimi kamerami, tako kar se tiče ločljivosti (10 mm pri razdalji 5 cm v primerjavi z 5-15 mm) kot napovedanega izkoristka (1,6 ‰v primerjavi z 0,05-0,2 ‰). Red velikosti večji izkoristek bi tudi uravnotežil izgubo informacije, ki jo predstavlja rekonstrukcija iz stožcev pri comptonski namesto iz premic pri Angerjevi kameri. Tako izkoristek kot ločljivost opisanega prototipa sta še daleč od optimalnega za comptonsko kamero: izkoristek lahko povečamo za red velikosti z večanjem dimenzij sipalca, ločljivost pa z optimizacijo geometrije in bolj premišljenimi rekonstrukcijskimi algoritmi. Primerjava optimiziranega prototipa bi bila tako še bolj v korist comptonski kameri, kakor tudi primerjava pri višjih energijah žarkov γ.

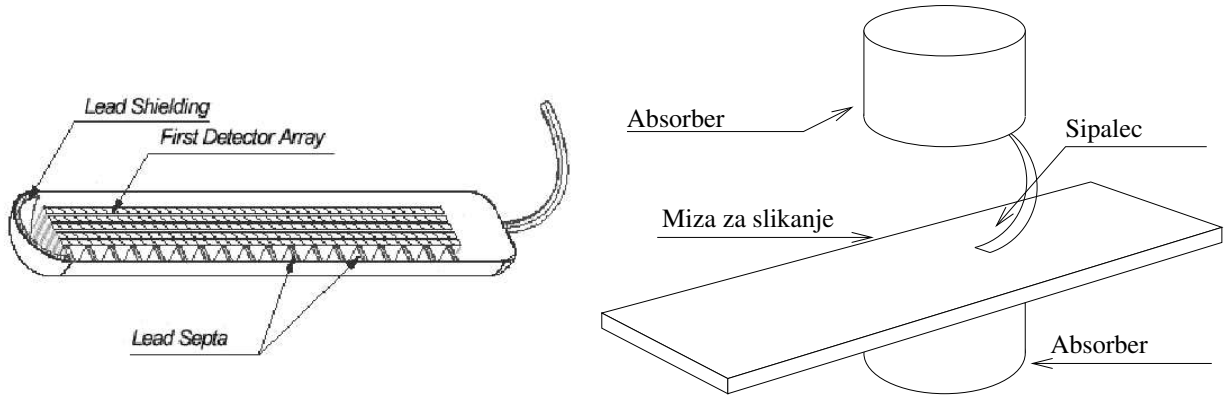

Slika 9.18. Slika predvidene probe za prostato. Levo: Za prst debel sipalec (First Detector Array) iz tesno zloženih silicijevih detektorjev v svinčenem ohišju (Lead Shielding). Desno: Absorber obkroža mizo za slikanje in sipalec.

Zanimiva aplikacija, predvidena na podlagi comptonske kamere, je proba za prostato (slika 9.18). Sestavljena bi bila iz velikega absorberja, obkrožajočega pacienta, in prst debelega sipalca, vstavljenega intra-rektalno, s širokim zornim kotom na prostato. Simulacije napovedujejo, da bi bila ločljivost in izkoristek naprave pri slikanju z izvori višjih energij (^{111m}In, 245 keV) primerna za slikanje primarnih tumorjev prostate. Trenutna tehnologija preiskave SPECT tega ne omogoča, izboljšana metoda pa bi služila natančni določitvi lokacije in obsega tumorja in s tem zgodnejši diagnozi in boljšemu spremljanju zdravljenja bolezni.

Appendix A

Sources of electronic noise and their propagation through front-end electronics

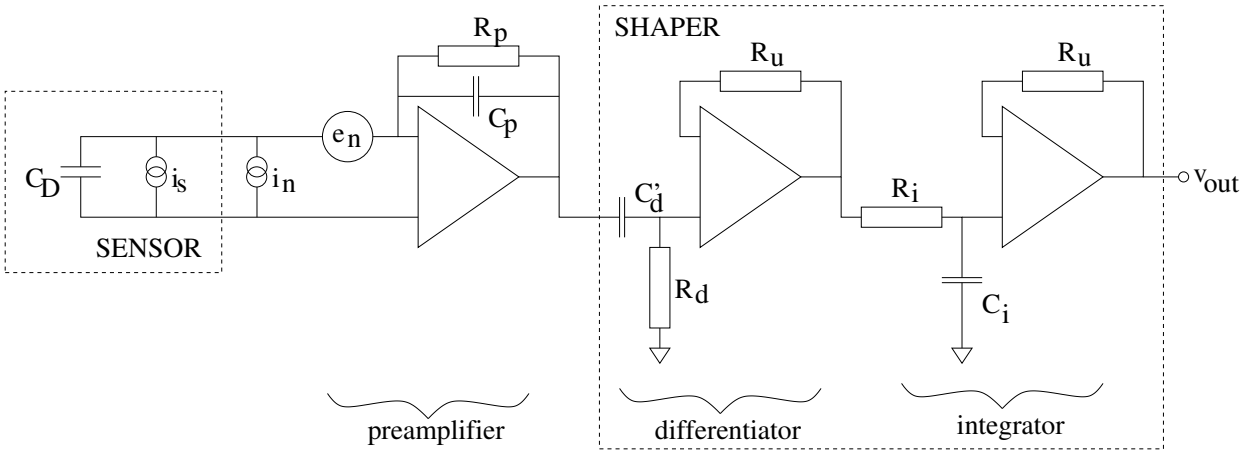

Figure A.1: A schematic representation of the first stage electronics circuit and the sensor, including the noise sources.

Figure A.1 shows the electronic schematic, including the noise sources. They come in two varieties, either as e_n, a voltage noise source or i_n, a current noise source. Both current and voltage noise are white, i.e. independent of the frequency, and are quantified with their spectral power densities, in terms of V^2/Hz or A^2/Hz for voltage or current noise sources, respectively.

The noise at the output (v_out) is the integral of N^2, the voltage spectral power density

integrated over $G(\omega)$ the frequency response of the system:

$$v_n = \frac{1}{2\pi}\int_0^\infty N^2|G^2(\omega)|d\omega. \tag{A.1}$$

The frequency response of the circuit in Figure A.1 is composed of the pre-amplifier response and the shaper response. The frequency response of the pre-amplifier is different for current and voltage sources, and will be derived separately.

The voltage of a voltage noise source is divided over the voltage divider composed by Z_p the complex feed-back impedance and C_D giving U_e^p, the voltage at the pre-amplifier output:

$$U_e^p(\omega) = \frac{i\omega(C_d + C_p) + \frac{1}{R_p}}{i\omega C_p + \frac{1}{R_p}} e_n. \tag{A.2}$$

In the frequency range of the shaper $1/R_p$ is negligible compared to ωC_p and U_e^p is essentially frequency independent:

$$U_e^p = \frac{C_d + C_p}{C_p} e_n. \tag{A.3}$$

The current of current noise source is integrated on C_p, yielding the frequency dependent voltage U_i^p at the output even if $1/R_p$ is considered negligible:

$$U_i^p = \frac{i_n}{i\omega C_p}. \tag{A.4}$$

This is an essential difference of the current and the voltage noise sources.

The shaper is composed of the differentiator or C-R circuit with a frequency response $T_d(\omega)$, and an integrator or R-C circuit with a response $T_i(\omega)$:

$$T_d(\omega) = \frac{i\omega\tau_d}{1 + i\omega\tau_d}, \tag{A.5}$$

$$T_i(\omega) = \frac{1}{1 + i\omega\tau_i}, \tag{A.6}$$

with the characteristic times of the differentiator $\tau_d = R_d C_d'$ and integrator $\tau_i = R_i C_i$. The differentiator is a high-pass filter with the cut-off frequency $1/2\pi\tau_d$ and the integrator is a low-pass filter with the cut-off frequency $1/2\pi\tau_i$. The full shaper response is the product of the two and the band-width is limited from both ends. Since the scatterer optimization for a high rate implies optimization of τ_d, the noise is minimized for $\tau_d = \tau_i = \tau_s$.

Inserting the frequency responses (A.5-A.6) back into (A.1), the corresponding voltage vari-

ations V_i and V_v of the current and voltage noise sources are obtained:

$$V_v^2 = \frac{e_n^2}{\tau}\,\frac{(C_d + C_p)^2}{C_p^2}\frac{1}{2\pi}\int_0^\infty \frac{\omega^2\tau^2}{\left(1+\omega^2\tau^2\right)^2}d(\omega\tau), \tag{A.7}$$

$$V_i^2 = \frac{i_n^2\,\tau}{C_p^2}\,\frac{1}{2\pi}\int_0^\infty \frac{1}{\left(1+\omega^2\tau^2\right)^2}d(\omega\tau). \tag{A.8}$$

The numerical value of both integrals is $\pi/4$, and the total noise appearing at the output is:

$$V_n^2 = \frac{1}{8}\left(e_n^2\,\frac{(C_d + C_p)^2}{C_p^2}\,\frac{1}{\tau} + i_n^2\,\frac{1}{C_p^2}\,\tau\right). \tag{A.9}$$

Appendix B

List-mode maximum likelihood expectation maximization

The list-mode maximum likelihood expectation maximization (LML/EM) method is an approximate reconstruction method. It consists of three combined approaches: image quality is estimated based on maximum likelihood, it is optimizied based on expectation maximization and data is organized as a list, hence list-mode. A breif explanation of each of the terms follows.

The maximum likelihood is translated into the imaging theory as a comparison in the measurement space. The interpretation is given for binned image in the measurement space. Poisson distribution of the bin content m'_j of bin j, bin index designated by values of all measured parameters for an event (impact positions in both sensor parts, energy measurement), is assumed, with the average value $m_j = \sum_{i=1}^{M} T_{ji} s_i$ given by the forward projection of the source distribution, equation (6.3). Then the part of the logarithm of the maximum likelihood (log-likelihood) which depends on the source distribution is given by:

$$\log L = \sum_{j=1}^{M} m'_j \log(\sum_{i=1}^{N} T_{ji} s_i) - \sum_{j=1}^{M} \sum_{i=1}^{N} T_{ji} s_i. \tag{B.1}$$

The expectation maximization is the variation of the source distribution s_i which maximizes log-likelihood under the condition that all s_i are non-negative.

The log-likelihood as defined by (B.1) above still requires the full matrix T_{ji} to be stored and manipulated. This requirement is circumvented if the list-mode approach is used. since the sum in (B.1) is evaluated only for measured points. This can be interpreted as decreasing the bin size of the measurement space until each measurement corresponds to a single bin. Then the measured contents m'_j are either 1 if there is an event with measurements corresponding to set indexed by j or 0 for the rest of the measurement space. The remaining indices, i.e.

those with content 1, are re-labeled to indices e which label the event, in which the set of parameters corresponding to the bin index j were measured. This requires a re-interpretation of the matrix elements T_{ji} calculated in the binned case - there they were used to indicate the portion of data a source at position labeled i will give in measurement bin j. Now the matrix elements are labeled t_i^e and signify the probability that the photon originating in i will be detected as event e. The log-likelihood is now:

$$L_{lm}(s_i) = -\sum_{e=1}^{N_e}\left(\sum_{i=1}^{N} t_i^e s_i\right) + \sum_{e=1}^{N_e}\log(\sum_{i=1}^{N^e} s_i), \tag{B.2}$$

with N_e number of detected events.

The expectation maximization yields the iteration step:

$$s_i'^{(+)} = \frac{s_i'}{R_i(1+\alpha\sum_{k=1}^{N} r_{ik}s_k')}\sum_{e=1}^{N_e}\frac{t_i^e}{\sum_{k=1}^{N} t_k^e s_k'}, \tag{B.3}$$

where $s'^{(+)}$ is the improved image estimate, and R_i is the (survival) probability that the photon emitted from bin i in the image is detected anywhere in the apparatus. The denominator of the first quotient of equation (B.3) provides a roughness penalty, with parameters α determining the amount of smoothing applied. The matrix elements r_{ik} are non-negative for eight nearest neighbours relative to the pixel labeled i, and their sum is set to 0 to perserve event count. The roughness penalty parameter is determined for a given reconstrcution problem as $\alpha = \alpha_0/\langle s'^{(0)}\rangle$, with $\langle s'^{(0)}\rangle$ the average intensity of the initial image approximation $s'^{(0)}$, i.e. the back-projection described above. The parameter α_0 nominally ranges between 0.005 and 0.01.

The complexity of the reconstruction now lies with the determination of the matrix elements t_i^e and the survival probabilities R_i as described in [WFC+01].

The relative survival probabilies are modeled assuming the absorber is homogeneous to the extent that the probabilities R_i depend only on the first detector geometry, and are proportional to the sum:

$$R_i \propto \sum_{V_s}\frac{\cos\phi(1-e^{-\mu z_{si}})}{d_{si}^2}, \tag{B.4}$$

over the cells V_s of the scatterer, with $\phi = \angle\vec{\mathbf{n_s}}, (\vec{\mathbf{r_s}} - \vec{\mathbf{r_i}})$ the orientation of the face of the cell (given by the cell normal vector $\vec{\mathbf{n_s}}$) with respect to the photon path, z_{si} the distance traversed by the photon within the scatterer before reaching the interaction point $\vec{\mathbf{r_s}}$, μ is the total attenuation coefficient in the absorber at energy of the initial photon and d_{si} the distance between the emission point $\vec{\mathbf{r_i}}$ and the interaction point. The assumption of the absorber homogenity was derived for an absorber forming a full ring around the scatterer module, and the validity of the assumption is somewhat questionable for an incomplete ring.

The relative probabilities t_i^e that the event e was caused by a photon emitted from point

$\vec{\mathbf{r_i}}$ are composed of two factors. The first factor is the probability $f(e)$ of detecting event e relative to other collected events, and the second probability $f^e(i)$ of event being a result of photon emission from point $\vec{\mathbf{r_i}}$ relative to other points in the source space. The factors $f(e)$ are:

$$f(e) \propto e^{-\mu z_{sa}} \frac{d\sigma}{dE_e}, \tag{B.5}$$

proportional to the probability $e^{-\mu z_{sa}}$ that the photon escapes the scatterer with z_{sa} the length of path of the scattered photon in the absorber and the probability of Compton scattering with energy transfer of E_e, which is given by the Klein-Nishina differential cross-section with respect to the energy transfer, $\frac{d\sigma}{dE_e}$, given by equation (2.13). The factors $f^e(\vec{\mathbf{r}})$ are:

$$f^e(\vec{\mathbf{r_i}}) \propto R_{is} g^e(\vec{\mathbf{r_i}}), \tag{B.6}$$

where R_{is} is the summand of equation (B.4) corresponding to the scatterer cell s hit in the interaction. In the case of perfect angular resolution, the probability $g^e(\vec{\mathbf{r_i}})$ would give the portion of the conic determined from equation (6.6), contained in the pixel centered at $\vec{\mathbf{r_i}}$ of the image. Since this is clearly not the case, there is a probability that pixels close to those lying on the cone were the source of the detected photon. This is accounted for by filling the adjacent pixels according to the cone spread distribution, which is determined from the parameters of the setup. The widths in terms of FWHM of the distribution for various scattering angles θ were computed in Chapter 5 and shown on Figure 5.5. Because of the non-Gaussian nature of Doppler-broadening, the cone spread distribution is not well approximated by a single Gaussian distribution, but a 10% addition of a Gaussian with 3 times the spread gives a good agreement with a modeled response [WFC+01]. Then the factor $g^e(\vec{\mathbf{r_i}})$ is computed as:

$$g^e(\vec{\mathbf{r_i}}) = \int_{V_i} d\vec{\mathbf{r}} \; (0.9e^{-r^2/2\sigma^2} + 0.1e^{-r^2/2(3\sigma)^2}), \tag{B.7}$$

where r is the distance between the position of the source determined from back-projection (6.6) and the position $\vec{\mathbf{r}}$ within the pixel i, perpendicular to the cone axis, and σ is the cone spread at the focal plane, determined as the angular resolution times the distance between the interaction point and the pixel being tallied.

To summarize the algorithm: The relative probabilites that photons emitted from pixel i in the image plane are calculated using (B.4) prior to event loop. Then, for each event, the relative weights $f(e)$ are computed and stored. In each iteration, starting from the image generated from back-projection, the pixels intersected by the cone of the event back-projection are determined. Then this pixels and nearest neighbours are tallied with relative probabilites $g^e(\vec{\mathbf{r_i}})$, and the scheme is repeated for all events. After each iteration, expectation maximization step is performed according to equation (B.3), and the improved image is obtained.

Appendix C

Parameters of data runs used in the thesis

Table C.2 gives a list of parameters which were set for data runs which appear throught the thesis. Words abbreviated in Table C.2 are described in Table C.1.

Abbreviation/Acronym	Description
LJ	Jožef Stefan Institute, Ljubljana, Slovenia
AA	University of Michigan, Ann Arbor, MI, USA
CERN	European Organization for Nuclear Research, Geneva, Switzerland
GND	Grounded front GND pads of VATAGP3
+n	n adjacent channels
M1,M2,L	SPRINT modules
lj3557a, lj3557b, lj3557c	
lj3557f, lj3557g	scatterer modules
`m`	`mbias` in μA
`v`	`vfp` in mV

Table C.1: List of abbreviations and acronyms which appear in Table C.2.

Table C.2: Parameters of data runs.

run #	date & location	scatterer modules	absorber modules	source	N_e	VATAGP3 settings	sensor bias [V]	readout mode	purpose	VATAGP3 threshold [keV]	Chapter in thesis
1001	10.2004 LJ	lj3557a	/	^{241}Am	1M	m:1200 v:800 GND	150	serial	calib	8	3
4001	6.2004 AA	lj3557a	/	^{99m}Tc	0.4M	m:1000 v:900	120	serial	calib	15	3 5
1002	10.2004 LJ	lj3557a	/	^{241}Am	0.2M	m:1200 v:800 GND	150	sparse +10	calib	8	3
1021	10.2004 LJ	lj3557a	/	^{241}Am	0.3M	m:1200 v:800 GND	150	sparse +3	calib	8	3
1011	10.2004 LJ	lj3557b	/	^{241}Am	0.2M	m:1200 v:800 GND	150	serial	calib	10	3
5101	8.2003 CERN	/	L	^{57}Co	30k × 1189	/	/	/	calib	/	4
14001	7.2004 AA	lj3557a-c lj3557f-g	M1 M2	^{99m}Tc	0.4M	m:1000 v:900	120	serial	data	20	5,6 7

Appendix D

Glossary of frequently used symbols, abbreviations and expressions

Symbol – Description
SPECT – single photon emission computed tomography
Compton electron – electron produced in Compton scattering
θ – scattering angle of the photon in Compton interaction
c – velocity of light in vacuum 2.99×10^8 m/s
m_e – electron rest mass m_ec^2=511 keV
E_γ – energy of the initial photon
E_e – kinetic energy of the Compton electron
$\vec{\mathbf{q}}$ – scattering momentum; difference of momenta of initial and scattered photon
p_z – component of momentum of bound electron along the scattering momentum
$\Delta_{\vec{\mathbf{p}}}$ – correction to Compton equation due to electron movement prior to scattering
$J(p_z)$ – distribution of p_z in atom
DDKNXS – double-differential Klein-Nishina cross-section
μ – attenuation coefficient
Z – atomic number
A – atomic mass
σ – cross-section of interaction
N_A – Avogadro number, 6.023×10^{26} atoms/Kmol
α – Compton parameter, $\alpha = E_\gamma/m_ec^2$
r_0 – classical electron radius r_0=2.82×10^{-15}m
ρ – material density
d – depletion depth
V – voltage drop across the diode

Symbol – Description
ϵ – dielectric constant (for silicon ϵ=11.9)
ϵ_0 – permittivity of space, ϵ_0=8.9×10^{-12}As/Vm
e_0 – electron charge magnitude, e_0=1.60×10^{-19}As
N_d – concentration of (donor) dopants in silicon bulk
V_{FD} – full-depletion voltage
w – thickness of the sensor
ϱ – resistivity of the silicon bulk
C – capacitance
S – diode area
C_{FD} – capacitance of depleted diode
N_{e-h} – number of created electron-hole pairs during ionization
Q – signal charge, corresponding to N_{e-h} electrons or holes
η – average energy of fast particle required to create an electron-hole pair
$i_e(t)$, $i_h(t)$ – current pulse created by moving electron/hole
q_e q_h – charge of charge carrier
$\vec{\mathbf{v_e}}(t)$ $\vec{\mathbf{v_h}}(t_)$ – velocity of charge carrier
$\vec{\mathbf{E_w}}$ – weighting field
$\vec{\mathbf{E}}$ – electron field
μ_e, μ_h – mobility of charge carriers
x – coordinate in diode; coordinate axis traversing the sensor, origin set at the junction
$E(x)$ – electric field magnitude; function of x
t_c^h, t_c^e – collection time; time necessary to collect carriers created by ionization on the readout electrode
C_p – capacitance of pre-amplifier feed-back
R_p – resistance of pre-amplifier feed-back
τ_p – pre-amplifier characteristic time
e – base of natural logarithm, e=2.72
v_{out} – pulse at the output of (the slow) shaper
τ_s^E – shaping time of the slow shaper providing spectroscopic output
V_n – noise of v_{out} in units of voltage
σ_n – equivalent noise charge of v_{out}
I_d – current through the diode under reverse bias conditions
e_a – voltage noise power density of the pre-amplifier
v_{thr} – threshold voltage level
τ_s^t – shaping time of the analog pulse generating trigger
σ_n^t – equivalent noise charge of analog pulse generating trigger
f_n – rate of triggers caused by base-line oscillations
f_r – maximal tolerable f_n

Symbol – Description
α_r – logarithmic noise rate suppression factor
Q_{min} – minimum detectable signal charge
$E_{e,min}$ – minimum energy of Compton electron required for detection
B – charge collection efficiency
SINTEF – The Foundation for Scientific and Industrial Research at the Norwegian Institute of Technology (NTH), Trondheim, Norway, `http://www.sintef.no`
ASIC – application specific integrated circuit
VATAGP, VATAGP3 – chips – ASICs performing the tasks of front-end electronics
IDEAS – Ideas ASA, Snarøya, Norway,`http://www.ideas.no`
DAC – digital-to-analog converter
`mbias` – master bias of VATAGP chip family which sets ASIC operating parameters
`vfp` – bias which sets R_p and consequentially τ_p
PCB – printed circuit board
DAQ – data acquisition
VME – physical interface and communication standard, `http://www.vita.com`
IB – intermediate board
FPGA – Field-Programmable Gate Array
PC – personal computer
ADC – analog-to-digital converter
p_i – pedestal of channel, pad indexed with i
s_i^e – content (in units of ADC) of readout channel i in event e
σ_i – noise of channel i
c^e – common-mode shift of s_i^e in event e
N_c – number of channels per chip
N_e – number of collected events, $1/N_e$ is also used as pedestal update weight
FWHM – full-width at half-maximum
C_0 – pre-amplifier capacitance
C_L – load capacitance
RMS – root mean square
PMT – photo-multiplier tube
SPRINT – single photon ring tomograph
BGO – bismuth germanate
E_s – energy of the scattered photon
L_i – amount of light collected on PMT i
N_{PM} – number of PMTs in a module, 20
g_i – relative gain correction of PMT i
$\vec{\mathbf{r_i}}$ – position of PMT i center
ε – detector efficiency

Symbol – Description
$a(\theta)$ – setup acceptance at a given scattering angle
Ω_1 – solid angle of the scatterer relative to the source
$P(\theta)$ – probability density for Compton scattering versus θ
D – distance between the source and interaction point in the scatterer
D_0 – distance between the source and the scatterer
$\vec{\mathbf{r_a}}$ – interaction point in the absorber
$\vec{\mathbf{r_s}}$ – interaction point in the scatterer
$\vec{\mathbf{r}}$ – position of the source
R – distance between interaction points in the scatterer and absorber
$S(\vec{\mathbf{r}})$ – distribution of relative source intensity
$\mathbf{y}$ – vector of measurements, $\mathbf{y}=(\vec{\mathbf{r_s}},E_s,\vec{\mathbf{r_a}})$
$M(\mathrm{y})$ – distribution of measurements, measurement image
s_i – intensity of sources in pixel/voxel centered at $\vec{\mathbf{r_i}}$, $s_i = \int_{V_i} d\vec{\mathbf{r}} S(\vec{\mathbf{r}})$
m_j – event count in bin j of measurement space
$\underline{T}_{ij}$ – transfer matrix; probability that source placed at $\vec{\mathbf{r_i}}$ will cause events in bin j of measurement space
c^e – circumference of conic (ellipse) on focal plane for event e
r_{is} – distance between point r_i on the focal plane and r_s
ℓ_i^e – length of conic contained in pixel i for event e
ℓ_{total}^e – total length of conic on focal plane in event e
w_i^e – weight assigned to pixel in event e
w_i – total weight assigned to pixel for N_e back-projected events

Bibliography

[Ang58] H. O. Anger, *Scintillation camera*, Rev. Sci. Instr. **29** (1958), no. 1.

[Bla99] J.W. Le Blanc, *Compton camera for low energy gamma-ray imaging in nuclear medicine applications*, Ph.D. thesis, University of Michigan, 1999.

[BOA+04] D. Bhattacharyaa, T. J. O'Neilla, A. Akyúzb, J. Samimic, and A. D. Zych, *Prototype tigre compton -ray balloon-borne telescope*, New Astronomy Review **48** (2004), 287–292.

[Com23] H. A. Compton, Phys.Rev. **22** (1923), 483.

[Fan47] U. Fano, Phys. Rev. **72** (1947), 26.

[GFD+96] F. D. Geeter, P. R. Franken, M. Defrise, H. Andries, E. Saelens, and A .Bossuyt, *Optimal collimator choice for sequential iodine-123 and technetium-99m imaging*, Eur J Nucl Med. **7** (1996), no. 23, 768–74.

[GFF+93] N. Gehrels, C. E. Fichtel, G. J. Fishman, J. D. Kurfess, and V. Schnfelder, *The compton gamma-ray observatory*, Scientific American **269** (1993), no. 6, 38–45.

[HBO+98] G. H. Hinkle, J. K. Burgers, J. O. Olsen, B. S. Williams, R. A. Lamatrice, R. F. Barth, B. Rogers, and R. T. Maguire, *Prostate cancer abdominal metastases detected with indium-111 capromab pendetide*, Journal of Nuclear Medicine **39** (1998), no. 4, 650–652.

[HLS90] T. Hebert, R. Leahy, and M. Singh, *Three-dimensional maximum-likelihood reconstruction for a electronically collimated single-photon-emission imaging system*, J. Opt. Soc. Am. A **7** (1990), 1305–1313.

[HVB+75] J. H. Hubbell, W. J. Veigele, E. A. Briggs, R. T. Brown, D. T. Cromer, and R. J. Howerton, *Atomic form factors, incoherent scattering functions, and photon scattering cross sections*, J. Phys. Chem. Ref. Data **4** (1975), 471–538.

[KAS+04] G. Kanbach, R. Andritschke, F. Schopper, V. Schönfelder, A. Zoglauer, P. F. Bloser, S. D. Hunter, J. A. Ryan, M. McConnell, V. Reglero, G. Dicocco, and J. Knödlseder, *The MEGA project*, New Astronomy Review **48** (2004), 275–280.

[KN28] O. Klein and Y. Nishina, Zeits. fur Physik **52** (1928), 853.

[Kno99] G. F. Knoll, *Radiation detection and measurement*, 3 ed., John Wiley & Sons, 1999.

[KWM+98] D. Kahn, R. D. Williams, M. J. Manyak, M. K. Haseman MK, D. W. Seldin, J. A. Libertino, and R. T. Maguire, *111indium-capromab pendetide in the evaluation of patients with residual or recurrent prostate cancer after radical prostatectomy. the prostascint study group.*, J Urol. **159** (1998), no. 6, 2041–2047.

[LCH+98] J.W. LeBlanc, N. H. Clinthorne, C. H. Hua, E. Nygård, W. L. Rogers, D. K. Wehe, P. Weilhammer, and S.J. Wilderman, *C-sprint: A prototype compton camera system for low energy gamma ray imaging*, IEEE, Trans. Nucl. Sci. **45** (1998), 943–949.

[LCH+99] J. W. LeBlanc, N. H. Clinthorne, C. H. Hua, E. Nygard, W. L. Rogers, D. K. Wehe, P. Weilhammer, and S. J. Wilderman, *Experimental results from the c-sprint prototype compton camera*, IEEE Trans. Nucl. Sci. **46** (1999), no. 3, 201–4.

[LKS+02] Z. Liu, G. A. Kastis, G. D. Stevenson, H. H. Barrett, L. R. Furenlid, M. A. Kupinski, D. D. Patton, and D. W. Wilson, *Quantitative analysis of acute myocardial infarct in rat hearts with ischemia-reperfusion using a high-resolution stationary spect system*, J Nucl Med **43** (2002), 933–939.

[MKW+93] J. B. Martin, G. F. Knoll, D. K. Wehe, N. Dogan, V. Jordanov, and N. Petrick, *A ring compton scatter camer for imaging medium energy gamma rays*, IEEE, Trans. Nucl. Sci. **40** (1993), no. 4, 972–977.

[Par00] L. Parra, *Reconstruction of cone-beam projections from compton scattered data*, IEEE, Trans. Nucl. Sci **47** (2000), no. 4, 1543–1550.

[Ram39] S. Ramo, *Currents induced by the electron motion*, Proceedings of the I.R.E (1939), 584–5.

[RCS+88] W. L. Rogers, N. H. Clinthorne, L. Shao, P. Chiao, Y. Ding, J. A. Stamos, and K. F. Koral, *Sprint ii, a second generation single photon ring tomograph*, IEEE, Trans. Med. Imaging **7** (1988), 291 –297.

[Ric45] S. O. Rice, *Mathematical analysis of the random noise*, Bell Syst. Tech. Journal **23,24** (1944,1945), 282,46.

[S. 01] S.J. Park S. J. Wilderman, L. Han *et all*, *"Experimental Setup for a Very High Resolution Animal PET Based on Solid-state Detector"*, Conference Record 2001 IEEE Nucl. Sci. Symp. and Med. Imag. Conf., San Diego, Nov 4-10 (2001).

[SCC+03] A. Studen, V. Cindro, N. H. Clinthorne, A. Czermak, W. Dulinski, J. Fuster, et al., *Development of silicon pad detectors and readout electronics for a compton camera*, Nucl. Inst. Meth. A **501** (2003), 273–279.

[Sco73] J. H. Scofield, *Theoretical photoionization cross sections from 1 to 1500 kev*, Lawrence Livermore National Laboratory Rep. **UCRL-51326** (1973).

[SHS73] V. Schönfelder, A. Hirner, and K. Schneider, *A telescope for soft gamma ray astronomy*, Nucl. Inst. and Meth. in Phys. Res. **107** (1973), 385–394.

[Sin83] M. Singh, *An electronically collimated gamma camera for single photon emission computed tomography. part i: Theoretical considerations and design criteria*, Med. Phys. **10** (1983), 421–427.

[TH03] T. Tomitami and M. Hirasawa, *An analytical image reconstruction algorithm to compensate for scattering angle broadening in compton cameras*, Phys. Med. Biol. **48** (2003), 1009–1026.

[TNE74] R. W. Todd, J. M. Nightingale, and D. B. Everett, *A proposed gamma-camera*, Nature **251** (1974), 132.

[UM84] International Commission On Radiation Units and Measurements, *Stopping powers for electrons and positrons*, ICRU Report **37** (1984).

[WFC+01] S.J. Wilderman, J. A. Fessler, N. H. Clinthorne, J. W. LeBlanc, and W. L. Rogers, *Improved modeling of system response in list-mode em reconstruction of compton scatter camera images*, IEEE, Trans. Nucl. Sci. **48** (2001), no. 3, 11.

[WND+96] P. Weilhammer, E. Nygrd, W. Dulinski, A. Czermak, F. Djama, S. Gadomski, S. Roe, A. Rudge, F. Schopper, and J. Strobel, *Si pad detectors"*, Nucl. Instr. Meth. A **383** (1996), no. 1, 89–97.

[WP72] W.A.Reed and P.Eisenberger, *Gamma-ray compton profiles of diamond, silicon, and germanium*, Physical Review B **6** (1972), no. 12, 4596–4604.

[WRKE98] S.J. Wilderman, W. L. Rogers, G. F. Knoll, and J. C. Engdahl, *Fast algorithm for list mode back-projection of compton scatter camera data*, IEEE, Trans. Nucl. Sci. **45** (1998), no. 3, 957–61.

[Zha04] Lisha Zhang, *Compton gamma-ray imaging probes for prostate and breast*, Ph.D. thesis, University of Michigan, Biomedical Engineering, 2004.

Izjavljam da sem avtor te doktorske disertacije.

Andrej Studen

Ljubljana, 27. junij 2005